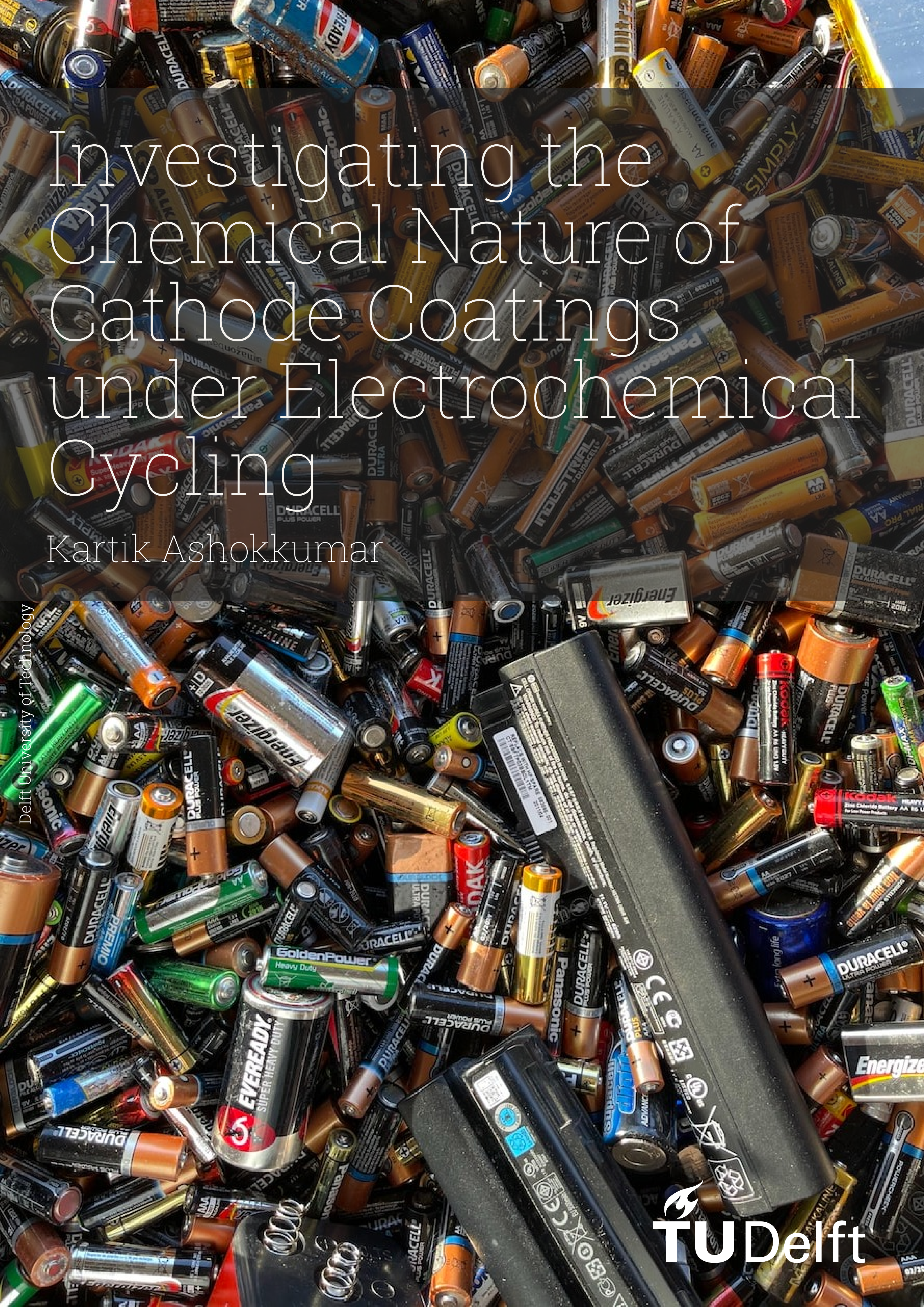

Investigating the Chemical Nature of Cathode Coatings under Electrochemical Cycling

Kartik Ashokkumar

Delft University of Technology

Investigating the Chemical Nature of Cathode Coatings under Electrochemical Cycling

by

Kartik Ashokkumar

to obtain the degree of Master of Science in Sustainable Energy Technology
at the Delft University of Technology,
to be defended publicly on Thursday August 31, 2023.

Student number:	5504015	
Project duration:	November, 2022 - August, 2023	
Thesis committee:	Prof. dr. ir. Marnix Wagemaker,	TU Delft, SEE, Supervisor
	Dr. Swapna Ganapathy,	TU Delft, SEE, Supervisor
	Prof. dr. ir. Ekkes Brück,	TU Delft, FAME
	Ir. Hanan Al-Kutubi,	TU Delft, SEE, Daily Supervisor

Cover Photo: Used batteries ready for recycling by John Cameron

Acknowledgements

This MSc thesis in front of you is the outcome of a memorable two-year journey at TU Delft. A period of extremely valuable professional and human experience in a highly international setting, during which periods of frustration and uncertainty were consistently overshadowed by moments of excitement and fulfilment. I owe a great deal of gratitude to the numerous people who inspired and helped me during my MSc study at TU Delft.

Hanan comes to mind first because without her, this thesis would not have been possible. She has invested a great deal of time and effort into my thesis from the inception to the culmination, and has been an exemplary supervisor. I will never forget her encouragement, guidance, and engaging conversations during our weekly meetings. I truly value the time I spent working with Hanan and will certainly miss that moving forward.

I want to express my sincere thanks to Marnix for supervising my thesis and serving as an inspiration. From you, I learnt a lot about batteries but also the rigorous scientific approach and the dedicating spirit for work. One of the things that sparked my interest in this field was how highly I enjoyed your lectures in Energy Storage in Batteries course. I am also incredibly thankful to Swapna for introducing me to Hanan and for her unwavering support throughout my highs and lows during the thesis period.

I owe a heartfelt debt of gratitude to Frans, who has always served as the point of contact for any questions regarding experimental work. Along with his enthusiasm, his words of encouragement always inspired me to raise the calibre of my work. It is because of his constant help that a great deal of the experimental work in this thesis was successful. My time in the lab and our amusing talks will be missed. I would especially like to thank Esther, Robert, Michel, Bart and Astrid for helping me with the experiments and for always clearing up any doubts I had.

I would also want to thank the SEE research group for all the informative weekly meetings, during which I gained a lot of knowledge about battery research. I would also like to express my gratitude to the PhD and post-doc members of the group for enlightening me with new perspectives during our lunch discussions. Additionally, I would like to convey my sincere gratitude to Powall B.V. and PTG Eindhoven B.V. for working with me and Hanan on this project. I want to thank Prof. Dr. ir. Ekkes Brück for evaluating my thesis and being a part of the graduating committee.

And almost-last, but definitely not the least, I want to express my gratitude to my family for their unconditional love and support, which has always motivated me to work harder. Finally, my sincere gratitude to all the friends I've made over the past two years for the innumerable wonderful experiences we've experienced together. A special thanks to Maitreyee, Shriram, Surya, Raghav, Dhruv, Imran, Srijit, Avi, and Anirvin for always being there for me and for helping me become a better person. I treasure our friendships and look forward to many more unforgettable experiences with you all.

Kartik Ashokkumar
Delft, The Netherlands
August, 2023

Abstract

The advancements in the field of e-mobility today far outpace all prior projections, and the rate of progress is quick. Due to their high power density and energy density, Lithium-Ion Batteries (LIBs) have grown to be an increasingly appealing alternative for use in electric vehicles. However, over extended use, these batteries frequently experience problems with capacity loss. Additionally, the battery's current collectors are challenging to scrape off from the cathode, which results in erroneous measurement results under spectroscopic observation. Furthermore, current collectors have a propensity to corrode with repeated use, which reduces the battery's power output.

In this study, the cathodes are manufactured without a current collector, i.e. a Free-Standing (FS) cathode, to prevent the issues brought on by the current collector. To assess how well these cathodes function in comparison to cathodes with an aluminium current collector, they are cycled both for long term and at different charging rates. In this investigation, the cathode materials examined include NMC 532, NMC 811, and LCO. The cycling behaviour of the FS cathodes was found to be quite comparable to that of the cathodes on current collectors. Using Electrochemical Impedance Spectroscopy (EIS), X-Ray Diffraction (XRD), and X-Ray Photon Spectroscopy (XPS), their cycling behaviour was further assessed in order to ascertain the chemical changes that occurred while cycling. The findings showed that an unstable cathode-electrolyte interface layer caused the cathodes to develop cracks on their surface during long-term cycling. Consequently, the electrolyte started to decompose, depositing impurities on the cathode surfaces. This behaviour produced a high impedance and prevented charge transfer over the cathode surface, leading to quick capacity fading and a subpar electrochemical performance.

To address the issue of capacity loss, the cathodes under investigation are coated with Al_2O_3 using Atomic Layer Deposition (ALD). Every commercial battery, in recent times, utilizes a cathode with a coating. However, there has been very little investigation into the chemical nature of the coating, especially during battery operation. This thesis investigates the chemistry of the coated cathodes during electrochemical cycling, highlighting their benefits and drawbacks. The ALD coated cathodes were found to demonstrate an improved cycling performance, with lower charge transfer resistances. Investigation of these cathodes after cycling revealed that the electrolyte decomposition had been greatly decreased, resulting in a virtually impurity-free surface. Additionally, it was discovered that the thicker the ALD coated layer is, the lower its cycle performance is likely to be, due to the increased charge transfer resistance caused by the thick layer. As a result, it is suggested to keep the coating as thin as possible to gain superior performances.

The chemical differences between the coated and uncoated cathodes in this work were examined through EIS, Scanning Electron Microscopy coupled with Energy Dispersive X-Ray Spectroscopy (SEM-EDS), XRD, XPS and Nuclear Magnetic Resonance Spectroscopy (NMR). In order to examine the chemistry of the coating layer more effectively, it is recommended to carry out NMR measurements at high magnetic fields. It is also recommended to carry out cathode investigations at high voltages to determine their behaviour. Overall, this thesis effectively illustrated the benefits of coating the cathodes with Al_2O_3. Additionally, it offered a fascinating route for FS electrode-specific research.

Keywords: Lithium-Ion Battery, Free-Standing cathode, Atomic Layer Deposition, Electrochemical cycling, NMC 532, NMC 811, LCO, Electrochemical Impedance Spectroscopy, X-Ray Diffraction, and X-Ray Photon Spectroscopy, Scanning Electron Microscope coupled with Energy Dispersive X-Ray Spectroscopy, Nuclear Magnetic Resonance Spectroscopy, Cathode-electrolyte interface.

Contents

List of Figures

List of Tables

Nomenclature

Abbreviation	Definition
LIB	Lithium-Ion Battery
EV	Electric Vehicle
EC	Ethylene Carbonate
EMC	Ethyl Dimethyl Carbonate
DMC	Dimethyl Carbonate
PC	Propylene Carbonate
DEC	Diethyl Carbonate
SEI	Solid-Electrolyte Interface
EEI	Electrode-Electrolyte Interface
CEI	Cathode-Electrolyte Interface
LCO	Lithium Cobalt Oxide
NMC	Lithium Nickel Manganese Cobalt Oxide
XPS	X-Ray Photon Spectroscopy
NMR	Nuclear Magnetic Resonance
ALD	Atomic Layer Deposition
ACEI	Artificial Cathode-Electrolyte Interface
FS	Free-Standing
EIS	Electrochemical Impedance Spectroscopy
SEM	Scanning Electron Microscopy
EDS	Energy Dispersive X-Ray Spectroscopy
XRD	X-Ray Diffraction
CC	Constant Current
CV	Constant Voltage
SOC	State of Charge
OCP	Open Circuit Potential
KKT	Kramers-Kronig Test
SED	Secondary Electron Detector
TMA	Trimethylaluminium
MAS	Magic Angle Spinning

1

Introduction

The development of next-generation technologies, specifically portable electronic devices and electric automobiles has created a high demand for energy storage devices with long lifetime, high energy density and high safety. Lithium-Ion Batteries (LIBs) are one of the most promising battery technologies which addresses all the factors mentioned above. In today's world, LIBs are the go-to choice for powering most electronic devices ranging from cameras, mobile phones, medical equipments to electric vehicles [1].

The global LIB market has seen a steady increase over the past decade from having a demand of 0.5 GWh in 2010 to over 520 GWh in 2020. This soar in the demand is expected to grow even further, with the projected demand being around 9,300 GWh in 2030, which is more than 17 times the demand in 2020 [2]. A pictorial representation of the increase in the LIB demand is shown in figure 1.1. This high demand is predominantly to cater to mobility applications, specifically Electric Vehicles (EVs) [3].

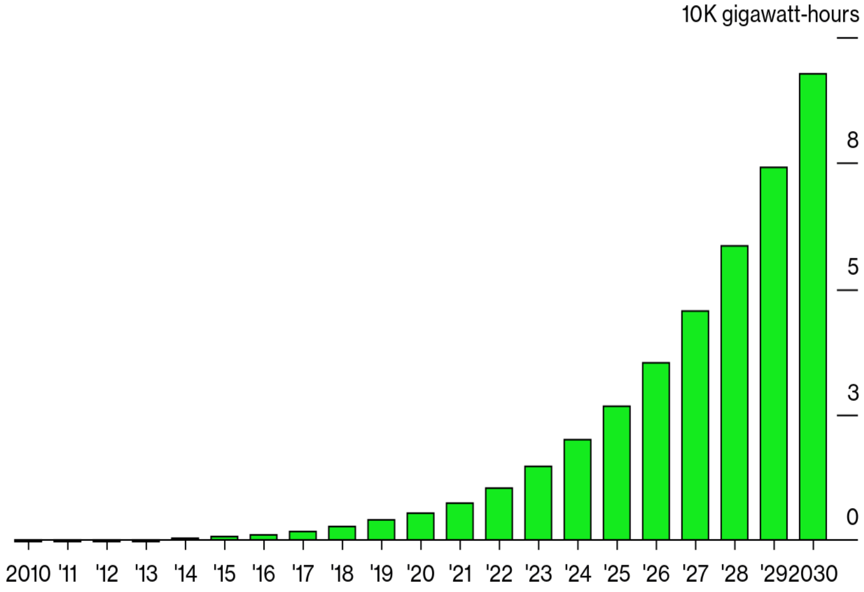

Figure 1.1: Estimated global LIB demand from 2020 to 2030, in GWh [2].

By 2030, the annual revenue of the battery value chain is expected to touch 400 billion euros [4]. To keep up with the enormous expansion of the EV industry, LIB makers must quickly ramp up cell production, a quest that calls into question the cost and sustainability of present LIB manufacturing practises. Cathodes (positive electrodes) are a critical component of a LIB cell which limit energy density and dominate battery cost among the several components used in the cell. To make EVs more accessible to society, it is critical to enhance the performance of its cathodes [5, 6]. This work will touch upon the performance enhancement of common LIB cathodes.

Chapter 2 of this thesis will explain the working of a LIB along with the current difficulties that a commercial LIB faces. Chapter 3 will outline the research questions of this thesis, which will help identify solutions to some of the current problems in a LIB. Chapters 4 and 5 will discuss the experimental data obtained, while chapter 6 will provide an overall conclusion for the thesis, along with recommendations for further research.

2

Lithium-Ion Battery: Theory and Fundamentals

This chapter provides an overview of the components used in a LIB along with their function during battery cycling. Furthermore, the chapter also describes the working of the LIB along with the active challenges it faces. Finally, this chapter concludes with the current trends in solving the existing challenges which outlines the main scope of this thesis.

2.1. Components of a LIB

A LIB primarily comprises of a cathode, anode, electrolyte, separator and current collectors. A cathode active material in a LIB is usually composed of a metal oxide. Some of the common cathode active materials include $LiNi_xMn_yCo_{1-x-y}O_2$ (NMC), $LiCoO_2$ (LCO), $LiFePO_4$ (LFP) and $LiMnO_4$ (LMO). The cathode active material is a powder, characterised by a primary and secondary particle size. Primary particles are typically micro- or nano-sized and consist of single or several layers of transition metals and lithium. Secondary particles are formed by the agglomeration of the small primary particles [7, 8]. Anodes are typically made of graphite which is used owing to its low cost and high reversible capacity [9]. There has been ongoing research into investigating different anode materials as a replacement for graphite, in order to improve the battery's performance and capacity [10].

An electrolyte in a LIB consists of lithium salts in organic solvents. These lithium salts consists of ions which allow the change transfer inside the battery. The lithium salts have high dielectric constants which help in achieving a higher salt dissociation. These lithium salts are dissolved by an organic solvent, which helps facilitate the movement of lithium ions. Lithium salts generally include $LiPF_6$ and $LiBF_4$, while the organic solvents include ethylene carbonate (EC), ethyl dimethyl carbonate (EMC), dimethyl carbonate (DMC), propylene carbonate (PC) and diethyl carbonate (DEC). The electrolyte is responsible for facilitating the reversible movement of lithium ions within the battery during charging and discharging cycles. Furthermore, commercial electrolytes also contain various additives to optimize specific properties such flammability or solid-electrolyte interface (SEI) generation [11, 12].

Separators are one of the most important components within a Li-ion battery, which directly influences the battery's cycle life, performance and safety [13, 14]. It consists of a micro-porous layer which is usually made of a polymeric membrane or a non-woven fabric mat. These are placed between the cathode and anode, and prevent both electrodes from having physical contact with each other. A separator for a LIB is usually chosen depending on a few factors. These include high porosity to absorb the liquid electrolyte, which provides high ionic conductivity for the cell during its operation, high electrochemical stability towards the electrode materials and electrolyte, and high mechanical strength [14].

Current collectors in LIBs are made of aluminium and copper foils for cathodes and anodes, respectively. During the battery making process, the cathodes and anodes are coated onto the current collectors, which are usually flat and about 12-15 μm thick. These current collectors bridge the components within the battery and connect them to the external circuit, thereby delivering electrons from external circuit to the active material and vice versa [15].

2.1.1. Assembling a coin cell

All the components mentioned above are arranged in a sequential order to make a LIB coin cell. An image of the arrangement is shown in fig 2.1. The image is a pictorial representation of a half cell, which consists of a cathode, and lithium metal as the anode instead of graphite. Since this work primarily focuses on investigation of cathode behaviour, we use a half cell for performing tests. The purpose for using half cells is that they are easy to make and enable to investigate the behaviour of the cathode. Moreover, they provide an infinite source of lithium. Additionally, during continuous cycling, undesirable side reactions between the electrolyte and lithium could lead to a loss of lithium ions. Due to the presence of metallic lithium, a half cell can make up for the lost lithium ions while a full cell cannot do so. However, these half cells encounter a problem of Li dendrite formation during electrochemical cycling, which does not occur in a full cell [16, 17, 18, 19].

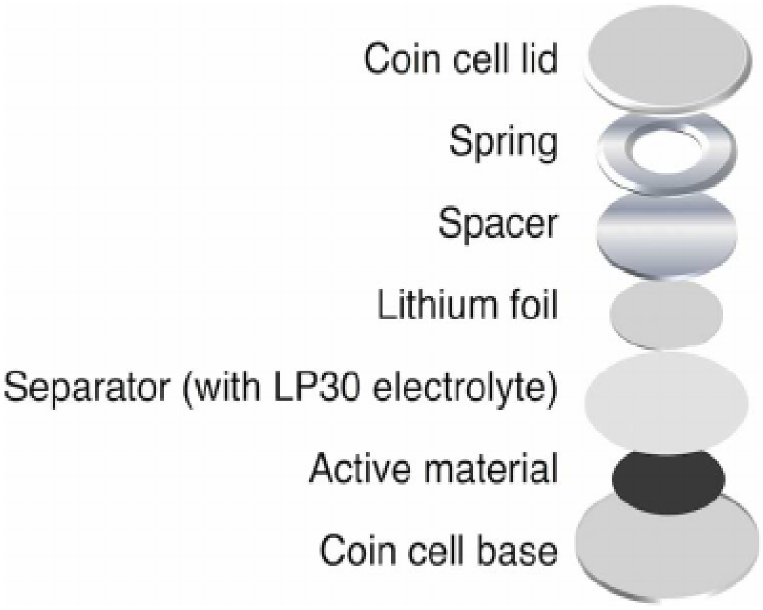

Figure 2.1: Assembly of different components within a coin cell (half cell) [20].

Fig 2.1 depicts a schematic of half cell assembly. The cathode side is the coin cell base (also known as can), while the anode side is the coin cell lid (also known as cap). Both the cathode and anode are active components within the cell. In this work, the separators employed are glass fiber (Whatman GF/A, 0.26 mm thickness, 1.6 μm pore size, 15 mm diameter) and Celgard® (2400-0804E-A, 25 μm thickness, 41 % porosity, 19 mm diameter). Because of its porous nature and great thermal stability, the glass fiber separator is used to increase the electrochemical performance of the cell. The Celgard is used owing to its excellent chemical stability, thickness, and mechanical strength [21, 22]. The Celgard is placed over the cathode, followed by the glass fiber separator. The electrolyte is pipetted onto the glass fiber separator. The electrolyte used in this work is LP30 (E-Lyte), which consists of 1M $LiPF_6$ in EC/DMC = 1:1 vol%. The lithium foil is placed over this, followed by the spacer and spring, which provide compression and alignment of the electrodes within the cell [23]. The cell is then pressed using an electric crimper machine (MSK-160D, MTI Corp., USA) and used for testing.

2.2. Working of a LIB

A LIB generates electrical energy by converting chemical energy stored in the electrodes via redox reactions. The electrochemical reactions taking place within a full LIB cell are shown in equations 2.1 to 2.3. For this, we assume graphite as anode and $LiCoO_2$ as the cathode. In the cathode, during discharge, reduction takes place where the cobalt ions combine with lithium ions to form lithium cobalt oxide ($LiCoO_2$). The half reaction is as follows:

$$\text{Li}^+ + \text{CoO}_2 + e^- \underset{\text{charge}}{\overset{\text{discharge}}{\rightleftharpoons}} \text{LiCoO}_2 \tag{2.1}$$

In the anode, oxidation takes place during discharge, where lithium is oxidised from Li to Li^+ through the following half-reaction:

$$\text{LiC}_6 \underset{\text{charge}}{\overset{\text{discharge}}{\rightleftharpoons}} C_6 + \text{Li}^+ + \text{e}^- \tag{2.2}$$

The two reactions add up to produce the overall reaction within a LIB as shown below.

$$\text{LiC}_6 + \text{CoO}_2 \underset{\text{charge}}{\overset{\text{discharge}}{\rightleftharpoons}} \text{C}_6 + \text{LiCoO}_2 \tag{2.3}$$

The charging and discharging mechanism of a modern commercial LIB is primarily based on intercalation and deintercalation of lithium ions, which occurs between the cathodes and anodes separated by an electrolyte. Intercalation refers to the infusion of Li ions into the host matrix without changing the crystal structure of the matrix [24].

During charging, oxidation occurs at the cathode which results in loss of negatively charged electrons. In order to maintain the charge balance, the positively charged Li ions move to the anode from cathode through the electrolyte and intercalate with graphite present in the anode. This process stores energy as a result. During discharging, oxidation occurs in the anode, where the Li ions are deintercalated from the anode and move back to the cathode, which releases the energy stored [25]. The amount of lithium stored in the electrodes determines the battery's energy density per weight unit. For a LIB, large amounts of Li can be stored which, as a result, provides the battery with high energy density.

In a standard LIB, an electrode-electrolyte interface (EEI) layer gets formed when the redox potential of the electrodes lies outside the electrochemical window of the electrolyte. The interface occurring on the anode side is stated as a SEI, while on the cathode side, it is referred as a cathode-electrolyte interface (CEI). The EEI is made up of CEI and SEI, both of which have thicknesses ranging from a few nanometers to micrometers [26]. Since this research focuses on investigating cathodes using a half cell, the study will emphasise more on the evolution and stability of the CEI.

The complicated chemical surface reactions between the cathode and electrolyte ultimately lead to the formation and evolution of surface CEI layers on cathodes. This initially occurs when cathode materials come into close contact with electrolyte [27]. Furthermore, the development of CEI is also thought to be linked to the dynamic evolution of SEI on the anode side. The anode SEI fragments move to the cathode via the electrolyte and contribute to the creation of the CEI [28, 29]. A stable CEI layer reduces electrolyte oxidation, cathode surface reconstruction, and transition metal dissolution, boosting the cathode's cycling stability [30]. A LIB would benefit from having a stable SEI and CEI layer, because it stabilizes the battery by stopping further interfacial reactions from occurring. On the other hand, an unstable CEI can lead to unwanted side reactions at the contact surfaces. These side reactions use up the electrolyte and deteriorate the electrodes, leading to battery failure [28].

2.3. LIB Cathode Materials

As discussed in the previous section, the performance enhancement of a LIB depends on the development of the cathode materials present within the cell. In this section, three common LIB cathode materials will be investigated. This thesis will focus specifically on the performance and the chemical nature of these cathode materials over cycling. A comparison of common LIB cathode materials along with their characteristics is shown in fig 2.2.

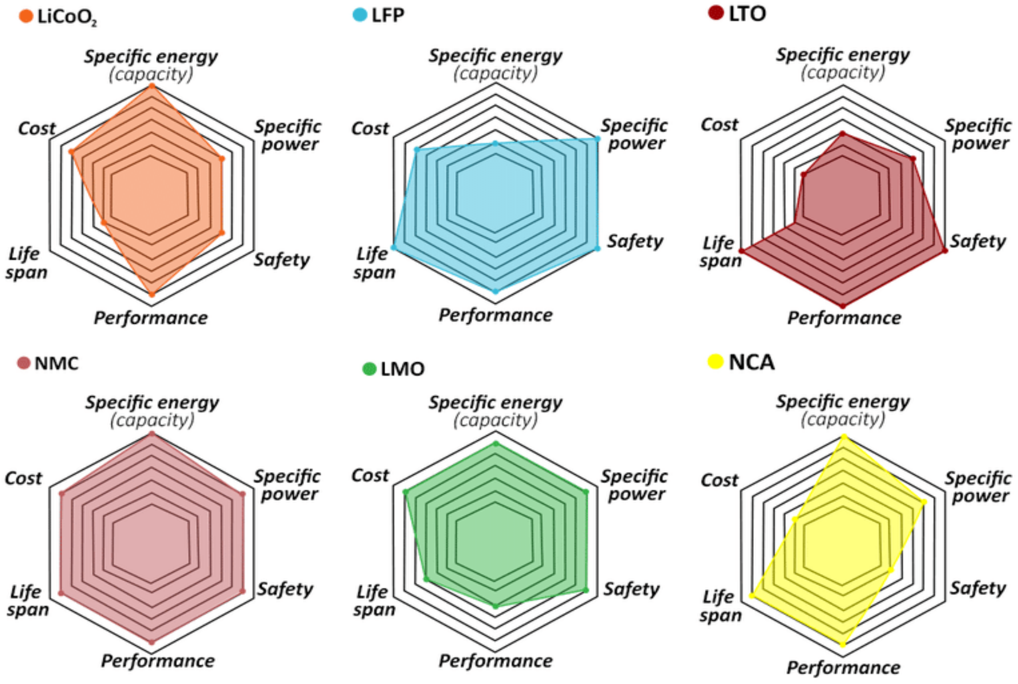

Figure 2.2: Comparison of popular LIB cathode materials [31].

2.3.1. Lithium Cobalt Oxide (LCO)

LiCoO$_2$ (LCO) is a form of layered transition metal oxide cathode which is most commonly used as a cathode material in rechargeable LIBs and consumer electronic products [32]. LCO is characterised by its distorted rock structure (α-NaFeO$_2$), in which Li and Co form a structure with hexagonal symmetry by occupying alternate layers in the octahedral sites of the cubic closed packed (ccp) of oxygen stacks. LCO is represented by its space group R(-)3m i.e. trigonal structure consisting of planes through which lithiation and delithiation occurs [33]. The crystal structure of layered LCO is shown in fig 2.3b.

The popularity of LCO as a cathode material for a majority of LIB applications is mainly associated with its long runtime, low self-discharge and high discharge voltage. However, despite its popularity, LCO has limitations which are being addressed to improve its stability and performance. LCO is a very expensive cathode with a low thermal stability. The high cost of the cathode is mainly due to the presence of Co, which is less available and hence more expensive to procure. Additionally, the mining of cobalt is very unethical [34]. The low thermal stability of LCO sometimes causes the cell to burst due to exothermic release of oxygen, if the cathode is heated beyond a certain point, causing runaway reactions. This usually occurs at temperatures over 200°C [35].

Furthermore, while charging the cell, it it has been found that the the cobalt dissolves in the electrolyte during delithiation, which as a result causes less lithium intercalation during discharging. It was also found that after complete delithiation, the CoO$_2$ layer formed, separates from the electrode surface. The above two mechanisms cause significant reduction in capacity of the cathode during cycling [33, 35].

2.3.2. Lithium Nickel Manganese Cobalt Oxide (NMC)

$LiNi_xMn_yCo_{1-x-y}O_2$ (NMC) is a high energy cathode material which has become popular in the last 30 years. These cathode materials are often spherical in shape [7] and have a high specific capacity. They have a layered, hexagonal α-$NaFeO_2$ structure belonging to the R-3m space group. A schematic representation of its structure is shown in fig 2.3a. The NMCs are also available at a lower cost because the Co content is reduced when compared to Co-rich cathodes like $LiCoO_2$. The NMC cathodes contain three transition metals: Ni, Mn and Co which provide high specific capacities, improved structural integrity and layered structures, respectively [36].

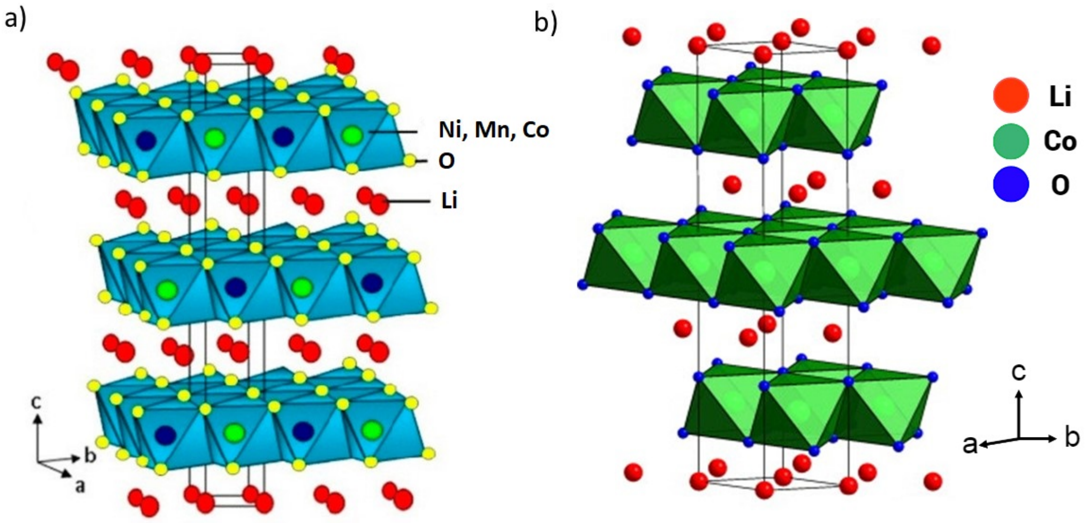

Figure 2.3: Structure of a) NMC and b) LCO, space group R-3m. Adapted from [37, 38].

Additionally, NMC cathodes show an enhanced thermal stability and also cycle at a higher operational voltage than many other commercial cathodes. Over the years, NMC cathodes with increased nickel content, also called Ni-rich NMCs have been investigated and pursued. This is due to the fact that Ni has the ability to cycle between Ni^{2+}/Ni^{3+} without any significant variation in its voltage during charging and discharging [39]. Hence, in this work, two specific Ni-rich NMCs will be investigated, NMC 532 ($LiNi_{0.5}Mn_{0.3}Co_{0.2}O_2$) and NMC 811 ($LiNi_{0.8}Mn_{0.1}Co_{0.1}O_2$).

These Ni-rich NMCs, however have downsides as well. They experience capacity fading and tend to have voltage drop during electrochemical cycling that affects their application commercially [40]. Presence of high Ni content leads to predominance of Ni^{4+}, which causes side reactions with the electrolyte, thereby hindering the thermal stability of the cathode. Moreover, high Ni content also results in Li/Ni cation mixing, which forms an inactive rock salt phase on the surface. The higher Ni content also causes stress on the material during cycling, causing micro cracks on the surface of the cathode [41].

There has been ongoing research to improve the performances of the NMC and LCO cathodes. Multiple surface modifications have been attempted, with some of them returning positive results. This work will be one in addition to the above which will focus on performance improvement through surface modification. This will be further discussed in the next section.

2.4. Active Challenges in LIB Cycling

In the previous chapter, the advantages of LIBs were discussed which attract extensive attention for their widespread use. However, despite their advantages, LIBs suffer from a number of challenges, some of which are currently being addressed through various research. Some of their limitations include slow Li transport and unfavourable interactions with electrolyte which reduces their performance efficiency. The LIBs have a tendency to overheat which raises concerns regarding their safety. Additionally, many of the cathode and anode materials typically used in a LIB suffer from low electrical conductivity [35]. Furthermore, the interfacial reactions occurring between the cathode and electrolyte jeopardises the performance of LIBs, causing negative phenomena like increased resistance along with the consumption of active lithium and electrolyte components [42].

As the demand for LIBs has increased over the past few years owing to increase in the production of electric vehicles, consumer electronics and grid scale power, there has been the need to produce batteries that produce high specific capacities and high voltage outputs. Here is where the commercial cathode materials used in the LIB face a challenge. Commercial cathode materials including LCO and NMCs have frequently demonstrated capacity deterioration [43], particularly after repeated long term cycling. This is a result of transition metal dissolution, decomposition of the electrolyte and structural changes within the cathode when cycled to high potentials [44]. A diagram illustrating the active challenges in a LIB is shown below.

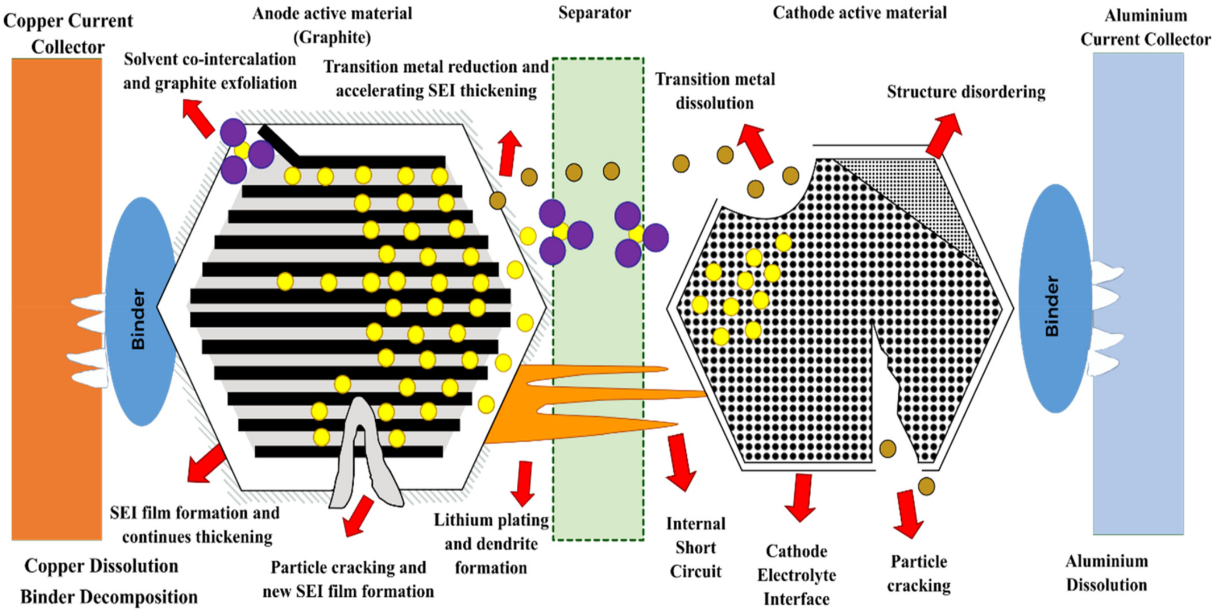

Figure 2.4: Challenges faced in a LIB during electrochemical cycling [45].

2.4.1. Challenges in a LIB due to the Presence of Current Collector

In general, most of the LIB research deals with modifications in electrode and electrolytes, but there has not been much research into the current collectors. Despite providing stability to LIB under cycling conditions, it has been observed that currently used current collectors corrode over long term cycling. As a result of corrosion, the active material in the cathode loses adhesion with the current collector, resulting in the loss of active material [46, 47]. This process reduces the overall power produced by the cell.

It has been proven that the aluminium current collector experiences corrosion during cycling. This is because the current collector has a native alumina layer, which, during cycling, participates in redox reactions with the electrolyte, potentially leading to corrosion [48]. This produces corrosion products, which precipitate on the cathode surface, limiting the transfer of Li ions and contributing to capacity losses in a battery. Moreover, this could also lead to short circuiting of the battery with rapid increase in the cell temperature, causing safety issues during the long term operation of the battery [47].

Reducing the weight of the electrodes might be a crucial and effective method for enhancing the energy density of LIBs. The electrode mass which is largely made up of the non-electrochemically active current collector and binder, greatly lowers the battery's overall energy density [49]. These current collectors also lack flexibility and are brittle when bent [50]. This makes its use in flexible electronic devices dubious.

Additionally, while testing the electrodes with different spectroscopic techniques such as X-Ray Photon Spectroscopy (XPS) and Nuclear Magnetic Resonance Spectroscopy (NMR), the presence of the current collector makes it challenging to properly scrape the cathode off. The scraping process was time consuming and often times it led to small pieces of the current collector being scraped off together with the cathode material, causing hindrance while observing the spectra in such techniques. An alternative was needed to ease this approach, but at the same time not losing the primary characteristic of a LIB cathode under cycling.

This research specifically focuses on two specific limitations described above, regarding the low cycling stability of LCO and NMC cathodes, and the hindrance of current collector for spectroscopic measurements. A solution is sought for the limitation, which will be described in the next section.

2.5. Current Trends in LIB Chemistry

2.5.1. Atomic Layer Deposition (ALD) of LIB Cathodes

In the past few years, numerous surface modification techniques have been actively investigated in order to improve the cycle stability of LIB cathodes. This involves altering the CEI by placing an ultrathin film as an artificial CEI (ACEI). Two such prevalent techniques used lately include surface coating and surface modification through doping [51, 52, 53].

There have been many investigations into the artificial CEI layer through coating various films such as metal oxides (Al_2O_3, ZnO, MgO, Li_2MnO_3, Li_2ZrO_3) metal fluorides (AlF_3), metal phosphates, metal carbonates and carbon [54, 55, 56, 57, 58, 59]. Each of the above coatings had different levels of success in terms of achieving cycling stability. Specifically, surface coating with Al_2O_3 through ALD has attracted significant attention as a protective surface coating for cathodes in LIBs, owing to its low-cost and abundance. Moreover, the Al_2O_3 coating has uniformly proven to increase the cycling lifetime and helped in eliminating interface instabilities [54, 60, 61, 62, 63].

ALD is a promising technique that produces a conformal ultrathin film with angstrom-level thickness on a substrate, by alternating the exposure of reactant and precursor within a reactor. Its self-limiting feature enables precise, uniform film growth and composition control at the atomic level [64]. Moreover, the presence of Al_2O_3 prevents electrolyte oxidation and shows a high stabilizing effect on the structure of the electrodes, even at high cutoff voltages [65, 66]. In this work, the LCO and NMC cathodes are coated with Al_2O_3 using ALD. Despite various research into ALD Al_2O_3-coated cathodes, its chemical nature upon cycling has not been researched extensively. The goal of this work is to investigate the coating before and during battery operation to get an insight into its chemistry during the process. A detailed description of the ALD coating process is mentioned in chapter 5, along with the results for the ALD coated cathodes after cycling.

2.5.2. Free-Standing (FS) Cathodes

In the previous section, it was discussed that the presence of metal current collector causes a restraint when attempting to investigate the cathode chemistry. As an alternative, in this work, the cathodes are made and tested without the presence of any current collector i.e. a free-standing (FS) cathode. The FS electrodes are thin electrodes which serve as a replacement to the commercially used electrodes on current collectors. Research into these electrodes has focused on modifying the surface and structural design of the electrode to provide good flexibility. These electrodes have also proven to show good electrochemical performance, similar to cathodes with current collectors [67, 50, 49, 68]. Since the FS cathodes do not have an aluminium current collector, they can be directly used for spectroscopic measurements without the need for scraping. This, therefore gives an accurate chemical composition of the cathode elements without any hindrance.

Moreover, nowadays, energy storage mechanisms like capacitors and batteries are needed for thin-film based electronics, portable electronics, and flexible displays. Despite the introduction of many flexible devices in the market, this technology still has many challenges which remain unaddressed. A very flexible energy storage source that can tolerate repeated mechanical stress without affecting device performance is required, in order to create these flexible devices. Due to their high energy density, high operating voltage, long-term cyclability, and lack of memory effects, LIBs are unquestionably a consideration for powering these flexible devices. However, the electrodes present in the existing LIBs are rigid and fragile, which make them unlikely for flexible applications [67].

The presence of current collectors like aluminium and copper foils, which act as a support layer for the electrodes, are the primary cause of the stiffness. Aluminium and copper are additionally more brittle when bent which might result in the loss of connections inside the electrode materials and the failure of the device [50]. Therefore, using current collectors is not considered a good option for applications involving flexible devices. This provides scope for the usage of FS electrodes in these applications. The process of making a FS cathode along with its cycling results will be shown in chapter 4.

3

Research Questions and Thesis Outline

As discussed in the previous chapter, it has been proven through various research that ALD coated electrodes have shown significantly better cycling stability and less decomposition of the electrolyte under cycling. Additionally, the alumina layer present in the aluminium current collector has been known to react with the electrolyte during cycling, causing corrosion, which negatively impacts the battery's cycling performance. Scraping off the cathode from the aluminium current collector resulted in alumina being scraped off as well, which caused a hindrance in the spectroscopic measurements. Hence, when investigating the Al_2O_3 layer deposited with ALD, we cannot exclude the interference of the current collector.

As a possible solution, the FS cathodes, which do not have a current collector, are made and tested in this work. This work focuses on addressing the limitations presented in the previous chapter with the usage of both FS and ALD coated cathodes. The thesis is performed by finding solutions to a set of research questions which are mentioned in the following section.

3.1. Research Questions

The main research question that is investigated in the current work is:

”How does the chemical nature of the ALD-Al_2O_3 *coating change when subjected to cycling and does its presence lead to improved performance in LIBs?”*

A number of sub research questions have been devised to help answer the main research question, while concentrating on one aspect at a time. Four sub research questions have been formulated in total. They are as follows:

- How are FS cathodes made and how does the cycling performance of a FS cathode compare against a cathode with aluminium current collector?
- What are the changes in cycling behaviour of an ALD coated cathode compared to an uncoated cathode?
- What are the elemental changes observed for the coated and uncoated cathodes when subjected to electrochemical cycling?
- How does the aluminium environment change for an ALD coated cathode over cycling?

3.2. Thesis Outline

While the first two chapters of this report gave a broad outline on the working and existing limitations of a LIB, the next chapter i.e. chapter 4 will provide an insight on the electrochemical cycling behaviour of FS cathodes. The results are compared with cathodes coated onto aluminium current collectors. Additionally, chapter 4 will discuss the different characterization techniques used to understand the cathode behaviour during cycling and their results will be presented.

Chapter 5 of this thesis focuses specifically on the ALD coated cathodes. The chapter will discuss in detail the surface microstructure, cycling performance and characterization results of the ALD coated cathodes. The characterization performed in this chapter and the previous include Electrochemical Impedance Spectroscopy (EIS), Scanning Electron Microscopy coupled with Energy Dispersive X-Ray Spectroscopy (SEM-EDS), X-Ray Diffraction (XRD), XPS and NMR.

Chapter 6 of this thesis summarizes all the results and provides an overall conclusion for the work. The conclusion answers the research question stated above. Additionally, inputs for further research are provided.

4

Free-Standing Cathodes: Structure and Performance

4.1. Introduction

In the age of flexible electronics, consumer demand has fueled research into compact, thin, lightweight and bendable LIBs to fulfill the diverse design and power requirements of modern flexible electronic products. The cathode, which is a crucial component of LIBs, is made up of a current collector coated with a mixture of an active material, an electrical conductor and a binder. Because of the weak connection between the current collector and the other materials during frequent bending, this type of cathode is not appropriate for flexible or bendable LIBs [69].

The current collectors are also subject to corrosion if cycled for an extended period of time [48]. Moreover, the existence of current collectors, as explained in chapter 2, impacts the spectroscopic measurements of the cathode, which produces inaccurate results of its chemical nature. As a result, to minimise these shortcomings, alternative approaches for producing flexible LIB electrodes must be explored. In this work, a FS cathode is employed as a replacement for cathodes on current collectors in a LIB half cell. These FS electrodes are thinner than conventional LIB cathodes, due to the absence of a current collector, and have shown favourable flexibility and cycling performances [67, 70].

In this work, a facile method is applied to make FS cathodes, which will be described in the next section. Furthermore, the microstructure and cycling performances of NMC and LCO FS cathodes are compared to cathodes on an aluminium current collector. These FS cathodes will then be utilised for spectroscopic tests to investigate the elemental changes after cycling.

4.2. Materials and Methods

This section describes the materials and methods used for making and testing a FS cathode. Additionally, it also describes theory behind the characterization techniques used to analyse the cathodes during cycling.

4.2.1. Materials

In this work, three different cathodes are used: NMC 532, NMC 811 and LCO. The cathode powders are obtained from Gelon LIB Group Co., Ltd. These powders are made into cathodes, without the presence of a current collector i.e. FS cathodes. A detailed description of their preparation is given below. Additionally, the same cathodes are also made on aluminium current collectors to compare their performance with FS cathodes.

Preparation of a FS cathode

The preparation of a FS cathode requires the presence of a slurry containing the cathode material and a coating surface, from which the cathode is extracted. The making of the cathode slurry resembles the slurry used for the preparation of a conventional cathode on a current collector. The slurry-making procedure is outlined below.

The cathode slurry is made up of a powder mixture dispersed in an organic solvent. The powder mixture consists of 90 wt% of active material i.e. the cathode powder, 4.5 wt% of Super C45 i.e. carbon black (TIMCAL), 0.5 wt% of carbon nano-fiber (Aldrich, >98%) and 5 wt% of PVDF binder (Solef 5130). These powders are thoroughly mixed together for 30 minutes with an agate mortal and pestle. This mixture is dried overnight using a vacuum drier at 80°C. To make the slurry, N-Methyl-2-pyrrolidone (NMP) (Thermo Scientific, 99.5 %) is added in a volume ratio of 1:1 with the active material. The slurry is is then homogenized by stirring it for 90 minutes, using an overhead stirrer with a stirring speed of 1200 rpm. This process improves the consistency of the slurry, which is then coated and vacuum dried to produce the cathode [71, 72, 73].

Research done on FS electrodes so far, have interpreted different methods to make the FS electrode. Some include solution based etching process [68], coating onto an anodisc membrane filter [74] and coating on a glass substrate [75]. The difference in making a FS cathode to a conventional cathode on a current collector, lies in the coating process. For a conventional cathode on aluminium current collector, in this work, the cathode slurry is coated over a 15 μm aluminium foil using a 150 μm Zehntner ZUA 2000 doctor blade. However, for making a FS cathode, the slurry can be coated onto any flexible non-conductive polymer, paper, or plastic substrate with a conductive layer, which permits easy extraction of the cathode from the substrate [76]. In this research, release liners are used as coating substrates to coat the cathodes. A release liner is a thin sheet with a silicone layer that stops a sticky surface from adhering prematurely [77].

The coated foil is then allowed to dry at high temperatures in a drying oven for 15 minutes, before placing it in a vacuum oven overnight at 80°C, to remove moisture and residual solvent. After drying, the cathode is carefully extracted from the foil substrate to produce a FS cathode. This is then pressed with 400 MPa pressure, using a hydraulic press (Carver, 973214A). The cathodes are subsequently punched from the slurry as circular disks with diameter of 11.1 mm. An image of a pressed FS cathode punched into a circular disk is shown in fig 4.1 .

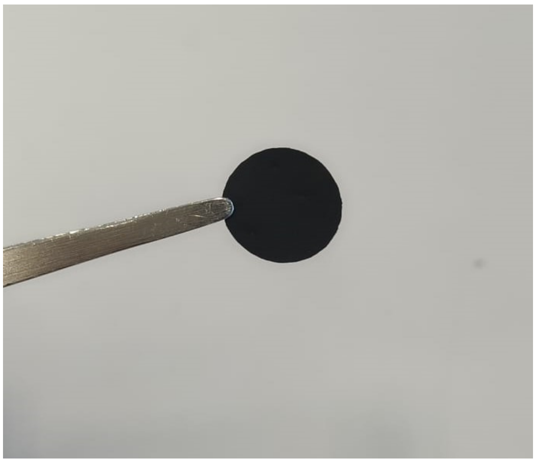

Figure 4.1: A FS cathode used in LIB half cells.

These cathodes are then sealed within pouch bags and stored within the glove box under argon conditions. These FS cathodes weigh between 9 mg to 12 mg and has a thickness ranging from 45 μm to 50 μm. In comparison, a cathode on an aluminium current collector weighs between 14 mg to 17 mg and has a thickness between 60 μm to 65 μm.

4.2.2. Methods

Procedure for cycling a LIB

To test the different cathodes, a coin cell, specifically a half cell consisting of lithium as anode material is used, in this study. The characterization of LIB electrodes in lithium half-cells is highly beneficial for studying the materials' intrinsic electrochemical behaviours [78]. We choose a half cell for testing because this work is especially geared at investigating cathode behaviour.

The half cells made with the NMC and LCO cathodes are then tested for electrochemical cycling at room temperature. Specifically, these cells are subjected to two tests: rate test and a long term cycling test. The purpose of performing a rate test is to test if the materials can hold different cycling rates during its function, while the long term cycling evaluates the materials' electrochemical stability over continuous charge and discharge [79]. The rate test is done with the Maccor battery tester while the long term tests were done in both Maccor and LANHE battery testing systems.

For the rate test, the cells go through five different cycling rates of 0.1 C, 0.5 C, 1 C, 2 C and 5 C, for five cycles each, and then are cycled back to 0.1 C for three cycles to test their capacity retention. For the long term test, the cells are cycled at 0.1 C for the initial two formation cycles, followed by 150 cycles at 1 C rate, and then cycled back to 0.1 C rate for the final two cycles. In order to prepare the cells for long-term cycling, a two-stage charging procedure is used: first, constant current (CC) is applied until the maximum charging voltage is attained, and then constant voltage (CV) is applied until the charge current reaches a low, defined value or until the predetermined, maximum charging time is reached [80].

Before testing, the cells go through a five-hour rest period. Moreover, the cells undergo a 10-minute rest period, following each cycle of charge and discharge. Allowing the cells to rest after discharging and charging would be necessary for the relaxation of concentration gradients caused by current flow [81]. All the FS cathodes and cathodes with aluminium current collector go through both rate test and long term cycling tests to evaluate their cycling behaviours. For the FS cathodes, the long term cycling was limited to a total of 75 cycles at 1 C rate apart from the formation cycles, due to channel constraints. For each cathode, three cells were made and cycled, in order to get an error estimate of their capacities during cycling.

For these tests, it is important to know the theoretical capacity of the cathodes and the cut-off voltage during testing. The voltage cut-off for the NMC 532 and LCO cathodes was 2.0-4.2 V while for NMC 811 it was selected as 2.0-4.3 V. The Upper Cutoff Potential (UCP) is particularly important for transition metal oxide cathodes, since the capacity fade is exacerbated at high UCPs. Considering this, we choose an UCP of 4.2 V for NMC 532 and LCO, while 4.3 V is chosen for NMC 811 [82]. For their potential range, the theoretical capacities of NMC 532, NMC 811 and LCO used are 166 mAh/g, 190 mAh/g and 140 mAh/g, respectively [83, 84].

Together with cycling, the differential capacitance analysis i.e. dQ/dV, is performed on all the cycled coin cells to study the degradation in the cathode capacity over long term cycling. The dQ/dV curve is obtained from the charge-discharge curve in LANHE, which calculates the capacity for every incremental change of voltage [85]. This method evaluates the rate of change of charge with voltage across each cycle, where its peaks represent the phase transitions in the cathode material as a result of intercalation and deintercalation. Studying the change in peak height and positions can help identify the different degradation mechanisms occurring in the cathode [86, 87].

Testing the Impedance of the LIB using EIS

EIS is a potent method for analysing electrochemical system behaviours. It is a non-destructive approach that can be used as a diagnostic or prognostic tool for quality control, estimating State of Charge (SOC), and monitoring internal temperature during a battery's lifespan. The components contained within commercial LIBs, including cathode, anode, current collector, electrolyte, generate various sources of impedance, such as resistive, capacitive, and inductive contributions, both electrical and electrochemical in nature. EIS probes these resistances, capacitances and inductances, producing a spectrum which has a distinct feature for each elementary process that make up the overall electrochemical mechanism in the cell [88, 89].

In this study, the EIS measurements are performed on the coin cells using a Metrohm Autolab device (PGSTAT302N with an FRA32M module) at room temperature. The potentiostatic measurements are performed at an Open Circuit Potential (OCP) at frequencies ranging from 0.1 Hz to 100 kHz. The measurements are done with 15 frequency points per decade and with a V_{rms} value of 0.005 V. The results from the measurements are shown in Nyquist plots, which chart the real vs imaginary part of impedance. The analysis is done using RelaxIS software [90].

Additionally, to determine the validity and quality of the spectra obtained after EIS, a Kramers-Kronig Test (KKT) is performed. The impedance of an electrochemical system is given by:

$$Z(\omega) = Z'(\omega) + iZ''(\omega) \tag{4.1}$$

Where Z' and Z'' represent the real and imaginary parts of the impedance, respectively. Z' and Z'' can also be called as resistance and reactance, respectively. This is taken as a basis to derive Kramers Kronig relation which results in the following [91]:

$$\begin{aligned}
Z'(\omega) - Z'(\infty) &= \frac{2}{\pi} \int_0^\infty \frac{\left(\omega_1 Z''\left(\omega_1\right) - \omega Z''(\omega)\right)}{\left(\omega_1^2 - \omega^2\right)} d\omega_1 \\
Z'(\omega) - Z'(0) &= \frac{2\omega}{\pi} \int_0^\infty \left[\frac{\omega}{\omega_1} Z''\left(\omega_1\right) - Z''(\omega)\right] \frac{1}{\left(\omega_1^2 - \omega^2\right)} d\omega_1 \\
Z''(\omega) &= -\frac{2\omega}{\pi} p \int_0^\infty \frac{Z'\left(\omega_1\right) - Z'(\infty)}{\omega_1^2 - \omega^2} d\omega_1 \\
\phi(\omega) &= \frac{2\omega}{\pi} \int_0^\infty \frac{\log\left|Z\left(\omega_1\right)\right|}{\omega_1^2 - \omega^2} d\omega_1 \\
R_p &= \frac{2}{\pi} \int_0^\infty \frac{Z''\left(\omega_1\right)}{\omega_1} d\omega_1 = Z'(0) - Z'(\infty)
\end{aligned} \tag{4.2}$$

where $\phi(\omega)$ and R_p are the phase angle and the polarization resistance, respectively. The polarization resistance represents the limitation of charge transport at the electrode/electrolyte interface [92]. By applying the above equations to the measured impedance spectrum, the validity of the spectrum can be calculated. The calculation of KKT is done using RelaxIS software.

Imaging the Cathode Microstructure using SEM-EDS

A Scanning Electron Microscope captures the surface phenomena of the cathode materials using a high-electron beam and analyses the outgoing electrons. The image that SEM produces can be helpful to understand the surface morphology of crystals, before and after cycling [93].

Certain important parameters to obtain a high resolution image are probe current, acceleration voltage and working distance. In this work, a Secondary Electron Detector (SED) is used, which helps produce a topographic SEM image with high surface detail [94]. The SEM (JEOL JSM-IT100) is operated with an acceleration voltage of 5 kV and a working distance between 11 mm to 13 mm to obtain a clear image.

The elemental compositions within the sample are detected using EDS. The SEM instrument is equipped with EDS to allow for the quantitative elemental analysis for the cathodes. EDS can identify elements with atomic numbers higher than boron, and these elements can be identified at concentrations of at least 0.1%. Material evaluation and identification, contaminant identification, spot detection analysis of regions up to 10 cm in diameter, quality control screening, and other applications are all possible with EDS [95]. The EDS data is obtained by mapping over a specific area within the sample.

In this work, we first analyse the morphology of the different cathode powders using SEM. This is followed by examining the change in fragmentation and surface crack evolution of cathodes during long term cycling.

Studying the Crystallographic Structure of Cathodes using XRD

A tried-and-true method for examining structural changes in oxide cathode materials is XRD. The distinctiveness of XRD when applied to LIBs lies in the ability to monitor (in real-time, in operando condition) the structural transformations, changes in lattice parameters, and phase composition during electrochemical charge/discharge experiments [96, 97, 98].

The XRD apparatus works on the principle of constructive interference of monochromatic X-rays and the crystalline sample measured. The diffraction of an X-ray by a crystal is given by Bragg's law, which is given by the formula:

$$n\lambda = 2d\,sin\theta \tag{4.3}$$

where n is the order of diffraction, λ is the wavelength, d is the interplanar spacing and θ is the Bragg angle. A schematic of the working of XRD setup is shown in fig 4.2. When the conditions are in accordance with Bragg's law, the interaction of the incident rays with the sample results in constructive interference [99].

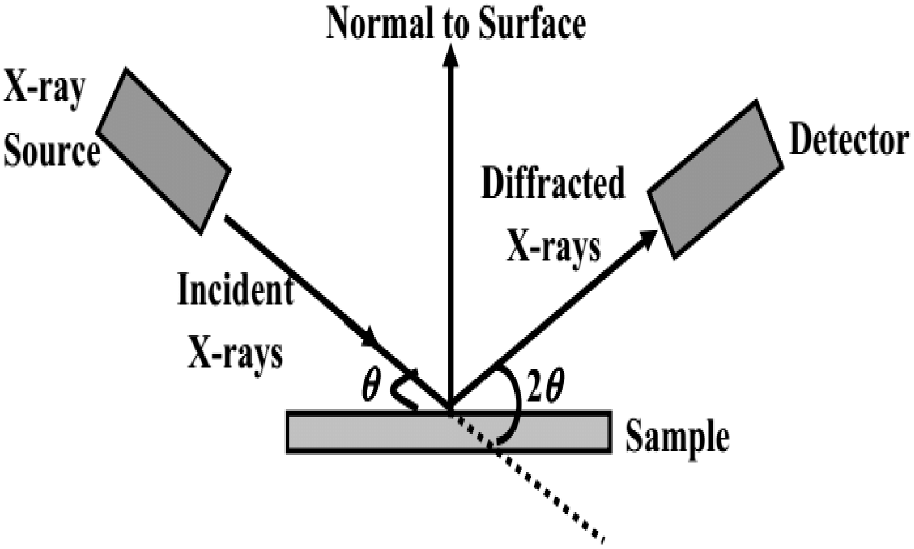

Figure 4.2: Mechanism of X-Ray Diffraction [100].

In this work, the XRD measurements are performed using either an open sample holder or an air-tight sample holder. For some measurements, a monochromator is used instead of an anti-scatter slit. The monochromator helps to remove unnecessary emission lines, like the Kα_2 line in the copper emission spectrum, which is relatively close to Kα_1 and produces double peaks, thereby substantially simplifying the appearance of a powder diffraction pattern [101]. Additionally, the monochromator reduces fluorescence caused due to the presence of cobalt in Cu Kα radiation [102]. The XRD patterns are obtained with a PANalytical X'Pert Pro system with Cu Kα radiation (at 45 kV and 40 mA). The diffraction data were collected with a Bragg-Bentano diffractometer in the 2θ range between 10° to 90°. The peaks are analysed using Match software [103], while the refinement was done using Rietveld refinement using GSAS-II software [104]. The lattice parameters are obtained through least square refinements in GSAS-II.

Cathode Surface Analysis using XPS

XPS is non-destructive, surface sensitive technique which studies the composition of surface contaminants and provides an overview of the evolution of cathode surfaces, before and after cycling [105]. This technique uses an X-ray beam on the surface of the sample which releases photoelectrons. The ability to identify the elements present in a material is made possible by the binding energies of the ejected photoelectrons, which can be computed from the observed kinetic energy of the electron [106].

The X-ray beam has a penetration depth of 10 μm [107], which allows for the detection of photoelectrons only upto 10 μm within a cathode surface. Electrons deeper than 10 μm do not contribute to the signal. A schematic of XPS penetration along with its respective peaks is shown in fig 4.3.

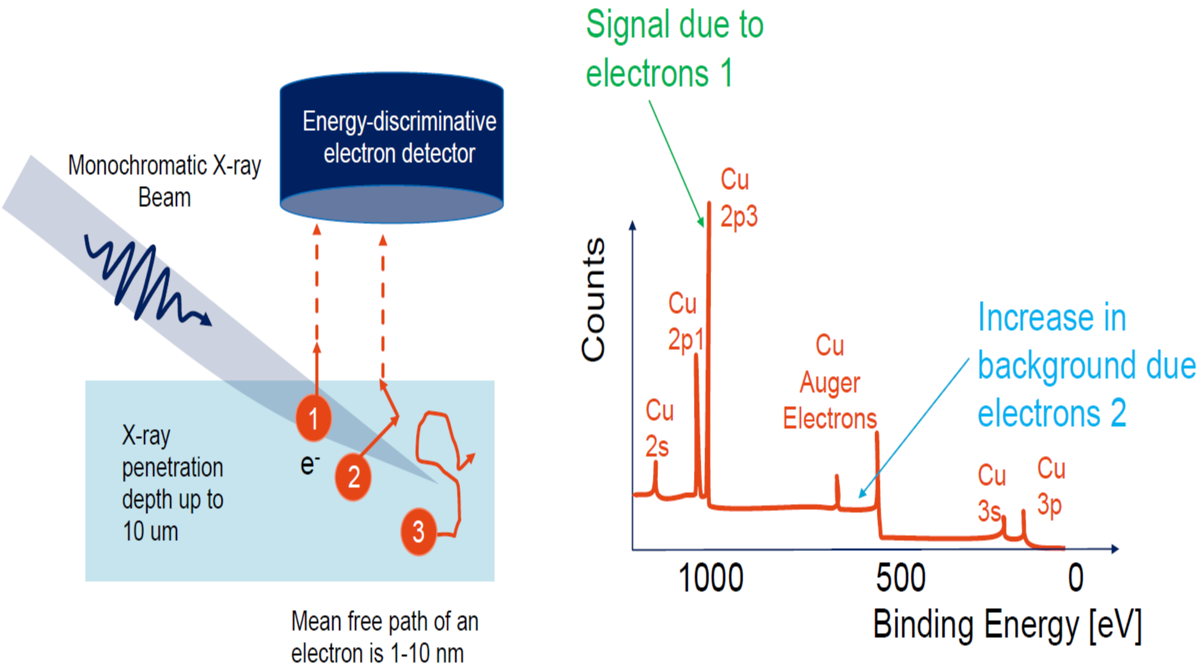

Figure 4.3: XPS penetration depth and its resulting peaks [106].

According to the above illustration, electron 1 generates a strong signal with a distinct peak, whereas electron 2 generates a strong background signal due to its energy loss. Electron 3 is not detected since it falls outside the apparatus's range of penetration.

In this work, XPS experiments are carried out at room temperature and at high vacuum using a K-Alpha Thermo Scientific X-ray photon spectrometer. Before testing the cycled cathode samples using XPS, they are washed with DMC (Sigma-Aldrich, >99 %) to remove any excess electrolyte present on the surface of the cathode which could interfere with the measurements [108]. For the measurements, Al Kα radiation (1486 eV) from a monochromatised X-ray source is used. The data processing was done using Casa XPS software [109]. For the data processing, the binding energies of the samples are corrected by setting the C 1s adventitious carbon peak at 284.8 eV [110]. The peaks were positioned using a non-linear Shirley background and fitted using a weighted least squares method containing both Gaussian and Lorentzian line shapes. The obtained data was initially smoothed using a Savitsky-Golay quadratic method, which uses linear least squares to smooth the data. The peak fitting was done according to the binding energy of the different peaks with a nominal standard deviation, by comparing it with references [111, 112, 113].

It is to be noted that due to the measurement time constraints, the amount of scans per sample had to be limited. This affected the scans of transition metal elements, which resulted in less observable peaks than the other elements. Hence, these could not be fitted and are added in A.5. Additionally, the lesser number of scans also affected the Li 1s scan for selected samples. Nonetheless, the high background was smoothed and then fitted. It is important to note that the fits only represent an approximate of the composition of each element or compound. XPS is a surface analysis technique and does not accurately identify changes in the bulk of the sample [114]. The XPS measurements on NMC 532 and NMC 811 powder samples, all the NMC and LCO cathode samples uncycled and after 1 cycle, were performed by PTG Eindhoven B.V.

4.3. Results and Discussion

4.3.1. SEM Analysis of Cathode Powders

The NMC and LCO powder samples are scanned and analysed using SEM to establish a baseline for their crystal structure and morphology. The images from SEM are shown in fig 4.4.

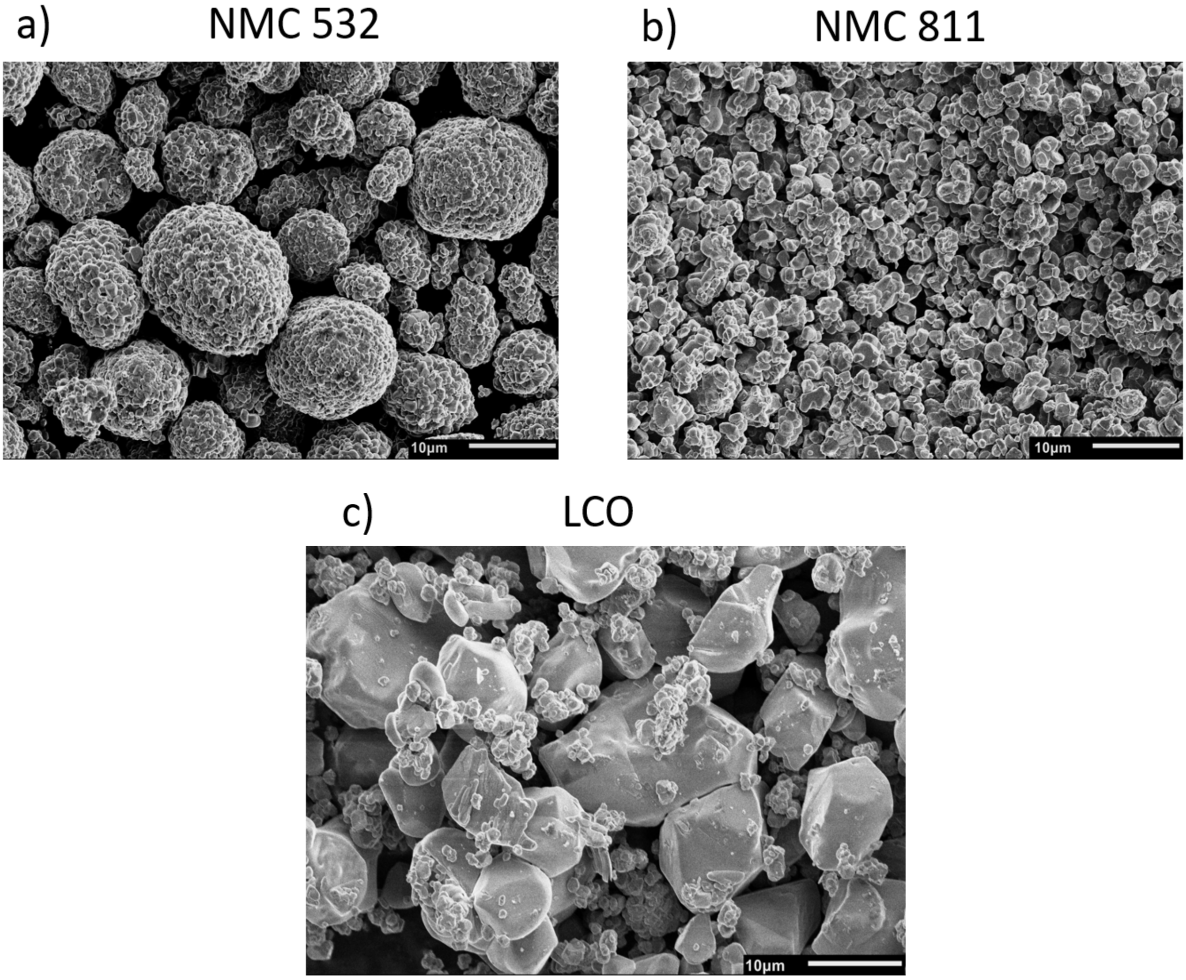

Figure 4.4: SEM image of a) NMC 532, b) NMC 811 and c) LCO powders taken at 2000x magnification with 5 kV acceleration voltage.

From the images, it can be observed that the NMC 532 is characterized by a spherical morphology with hard agglomerates, which are well defined and visible [115]. These spherical structures have diameters ranging from 8 to 13 μm. On the other hand, the NMC 811 has a polycrystalline structure [116], with spherical or spherical like crystals, 1 to 2 μm in size. These crystals are very small in size, in comparison to the other two cathode materials shown above. As a result of their small size, its structure was not clearly visible under high magnifications in the SEM micrograph.

The LCO powder consists of hard agglomerate crystals with a very well defined grain boundary. These crystals have diameters ranging from 10 to 18 μm. They are characterized by their large crystal sizes in comparison to the NMCs used in this work.

4.3.2. Cycling Performance

The NMC 532, NMC 811 and LCO cathodes are cycled for both rate test and long term cycling. The FS cathodes are tested along with cathodes on aluminium current collector. Post cycling, these cathodes are tested through various spectroscopic techniques, which are described in the following sections. The results for the cathodes after cycling are shown in fig 4.5. In this work, the FS cathodes are named as 'FS' while the cathodes on aluminium current collector are named as 'Al'.

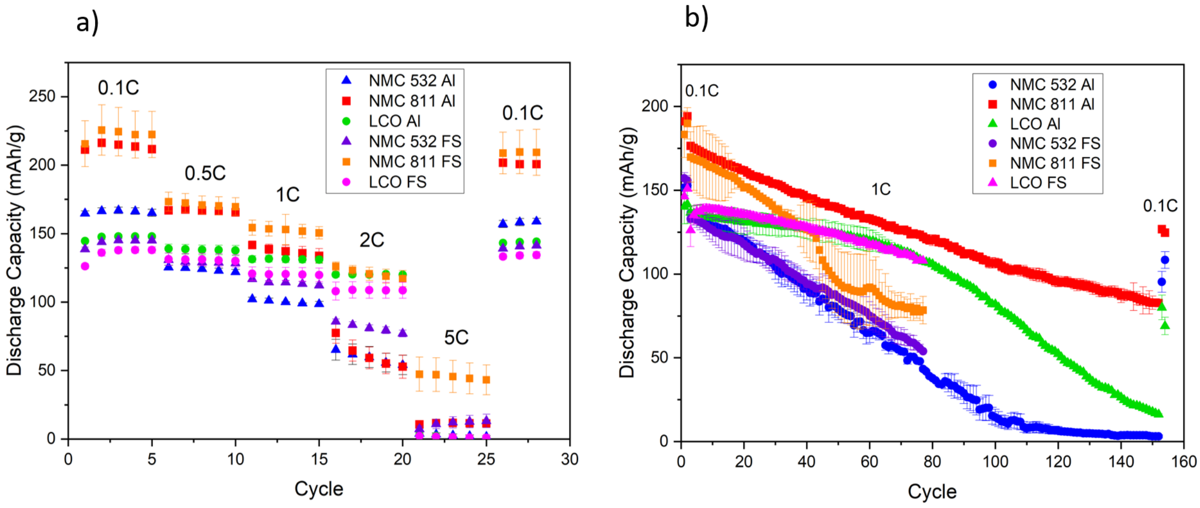

Figure 4.5: a) Rate test and b) long term cycling performed on NMC 532, NMC 811 and LCO cathodes.

From the figure above, it can be observed that all the FS cathodes display reasonably similar capacities to that of cathodes on aluminium current collectors, in both rate test and long term cycling. All the cathodes experience a reversible loss in capacity during their first cycle, which is a result of poor ion transfer kinetics [117]. NMC 811 cycles at a higher discharge capacity than the other cathodes due to its higher Ni content [118]. At a higher cycling rate i.e. 2C, it can be observed that there is a significant drop in capacity for NMCs. The capacity drops from 112.3 mAh/g to 85.8 mAh/g and 150.5 mAh/g to 126 mAh/g for NMC 532 FS and NMC 811 FS, respectively. This degradation in the electrochemical performance is primarily due to slow lithium diffusion, which results in excess of Li^+ ions at the surface of the cathode particles, thereby causing overpotential, impacting their performance [119, 120].

Furthermore, at 5C rate, the NMCs tend to have a slightly higher capacity than LCO. The capacity for NMC 811 FS and LCO FS at 5C rates are 45.6 mAh/g and 1.5 mAh/g, respectively. The higher capacity of NMCs with respect to LCO could be due to the smaller particle size of the NMCs, which paves way for faster Li diffusion than LCOs with bigger particle sizes. This theory is in accordance to the formula given below.

$$t = \frac{L^2}{D} \tag{4.4}$$

where D is the diffusion constant, L is the diffusion length and t is the time constant for ionic diffusion. For smaller particles, the diffusion length, L is smaller, thereby producing a reduced time constant which enables faster lithium diffusion [121].

In the long term cycling, it can be observed that the capacity initially remains stable but starts to degrade rapidly after prolonged cycling. According to literature, cathode degradation problems like particle cracking and surface degradation are less obvious during early cycling but become more obvious overall in later cycle life [83]. It is believed that repeated lattice expansion and contraction during long term cycling causes inter- and intra-granular cracking, which is a form of particle deterioration, leading to capacity decay [122, 123].

Additionally, we could observe that the capacity constantly decreases over cycling, specifically for NMC 532, where it reaches almost zero after 120 cycles. Multiple causes, especially the degradation of active material and an unstable CEI layer that restricts lithium transport across the interface, are blamed for the capacity reduction [124, 36]. In LCO, the drop in capacity after initially remaining stable, could be due to the formation of a resistive surface layer after delithiation, owing to LCO surface degradation, which in turn reduces the diffusivity of lithium ions [125]. Moreover, it can be seen that the discharge capacity of the NMC 811 FS sample in long-term cycling abruptly decreases after 42 cycles. This might be a result of NMC 811's lower particle size, which might disintegrate with prolonged cycling, since it lacks a protective current collector surface to hold it together. Furthermore, smaller particle size offers a larger specific surface area for unfavourable reactions to occur, leading to capacity fading [126].

Pressing a FS cathode improves its stability and homogeneity when cycling, while unpressed cathodes often lose their structural integrity through continuous cycling. To test this, long term cycling test at 1C was performed on unpressed and pressed NMC 532 FS cathodes. From the results (see fig A.1), it can be observed that the pressed cathode showed improved cycling stability while the unpressed cathode began to lose its capacity rapidly after 35 cycles, owing to the the loss of structural integrity.

4.3.3. Differential Capacitance of Cycled Cathodes

To further examine the capacity degradation observed during long term cycling, dQ/dV analysis was performed on the cycled cathodes. The results from the analysis are shown in fig 4.6. Differential capacitance analysis was performed across five different cycles for cathodes on aluminum current collector and four different cycles for FS cathodes. The differential capacitance for the cathodes were analysed after the 2nd cycle instead of the first, owing to the capacity loss that occurs in the first cycle as observed in the cycling results. The subsequent 4th, 15th, 75th and 150th cycle gave a good representation of the cathodes' cycling stability during the long term cycling.

The dQ/dV curve is characterized by two peaks: on the positive y-axis which corresponds to oxidation peaks during charging (delithiation), while the peak on the negative y-axis corresponds to reduction peaks during discharging (lithiation). This provides information about the stability of the CEI layer during cycling. The increase in charge transfer resistance in the cathode, which causes capacity fading, is the cause for peak separations during continuous charge and discharge; alternative explanations include the formation of cracks on the cathode surface [127].

The graphs show that for all the NMC and LCO cathodes, the peak shift increases as the number of cycles increase. This demonstrates the rise in charge transfer resistance, which can be linked to the capacity fading, as observed in the cycling behaviour. For NMC 811, specifically, we observe the presence of an additional peak at the higher voltage region. Presence of a peak at higher voltages indicates phase transformation. In our case, it represents phase transformation from H2 to H3, which denotes the structural instability of $LiNiO_2$ formed, that results in rapid capacity fading [128].

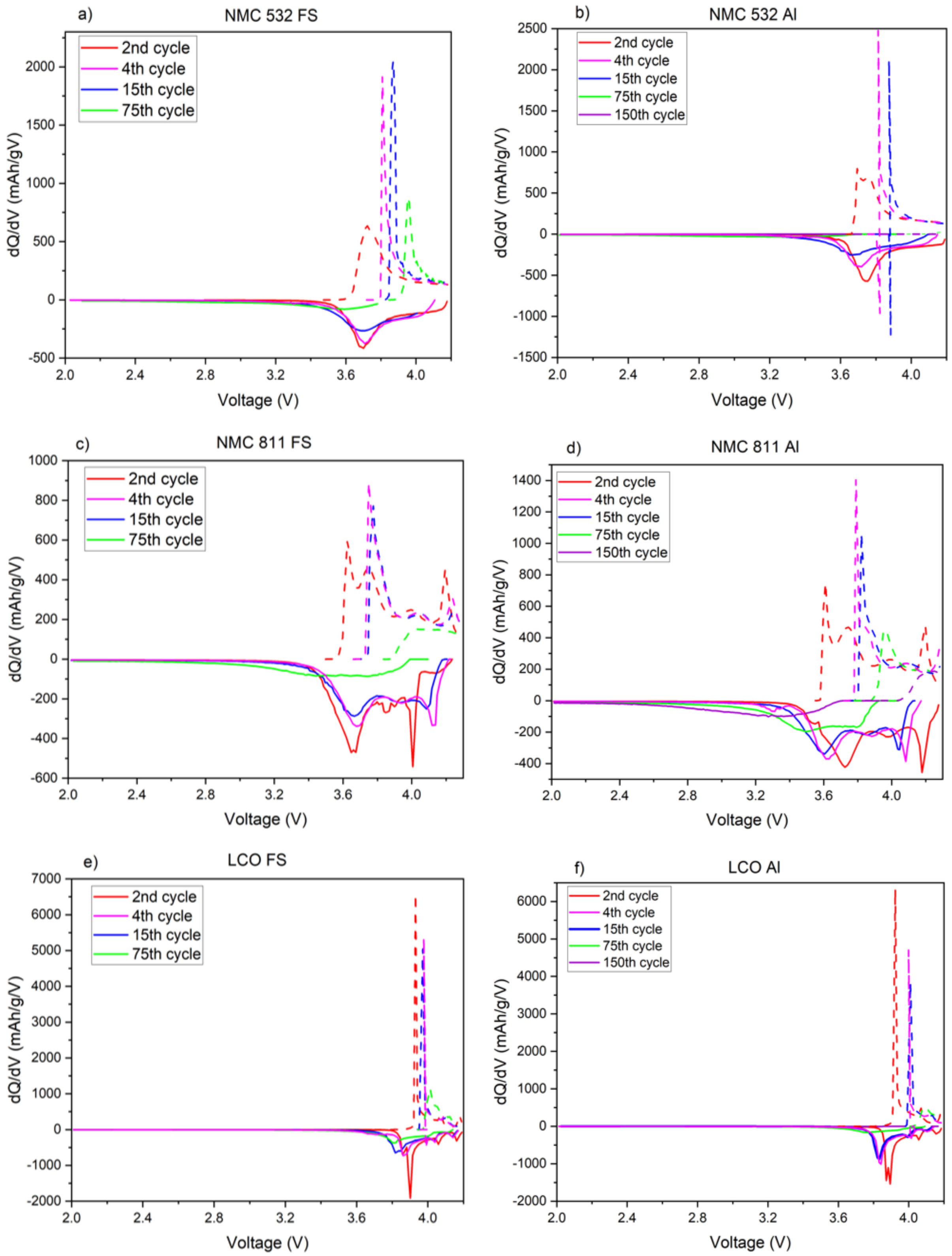

Figure 4.6: dQ/dV curves of NMC 532 *a) FS, b) AI, NMC 811 c) FS, d) AI, LCO e) FS and f) AI cathodes after 2nd, 15th, 75th and 150th cycles**.
* 2nd cycle is at 0.1C rate, while 4th, 15th, 75th and 150th cycles are at 1C rates.
** FS cathodes are tested until 75 cycles, while AI cathodes are tested until 150 cycles.

4.3.4. EIS Results for LCO and NMC Cathodes

In the previous subsection, there was a shift in the oxidation and reduction peaks observed as a result of cycling, which was attributed to an increase in charge transfer resistance. To verify this, EIS is performed on the LCO and NMC cathodes after the 1st and 75th cycle.

Fig 4.7 shows the Nyquist plot for the half cells during cycling. The plot after 1 cycle consists of three regions. At higher frequency region, the intercept of the semicircle with the x-axis is attributed to the electrolyte resistance, along with the resistance of the cell and wires (R_s). This is followed by a semicircle in mid frequency region which corresponds to the charge transfer resistance (R_{ct}). The sloping line at low frequency region represents the lithium ion diffusion (W_o). After 75 cycles, the Nyquist plot shows the presence of an additional semicircle, which is due to the formation of CEI layer. The resistance of this CEI layer is represented as R_a in the circuit. The Nyquist plots after 1 cycle and 75 cycles are fitted using equivalent circuit models shown in fig 4.8.

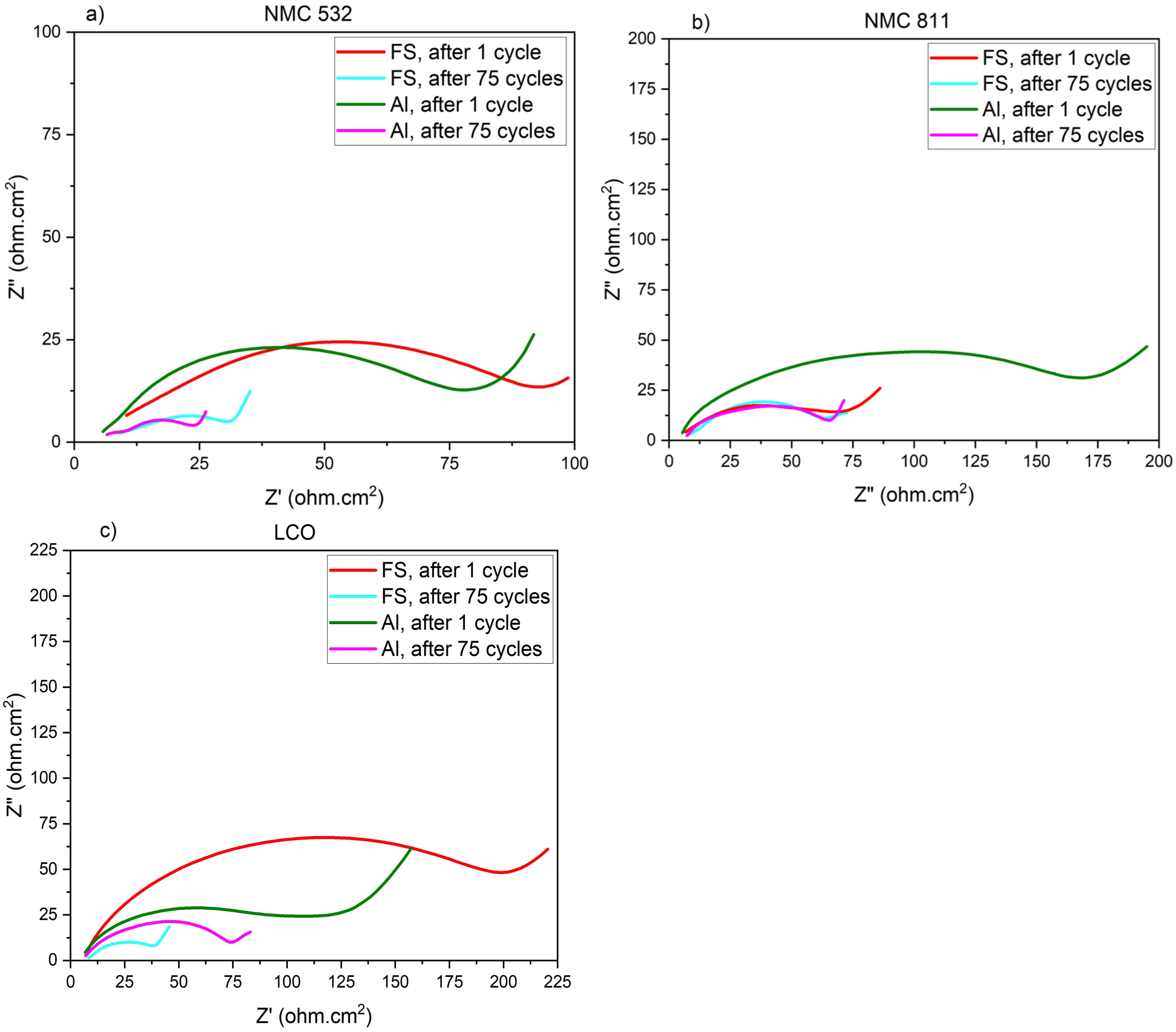

Figure 4.7: EIS spectra of FS and Al *a) NMC 532, b) NMC 811 and c) LCO cathodes after 1st and 75th cycle.
* 1st cycle is at 0.1C rate, while the 75th cycle is at 1C rate.

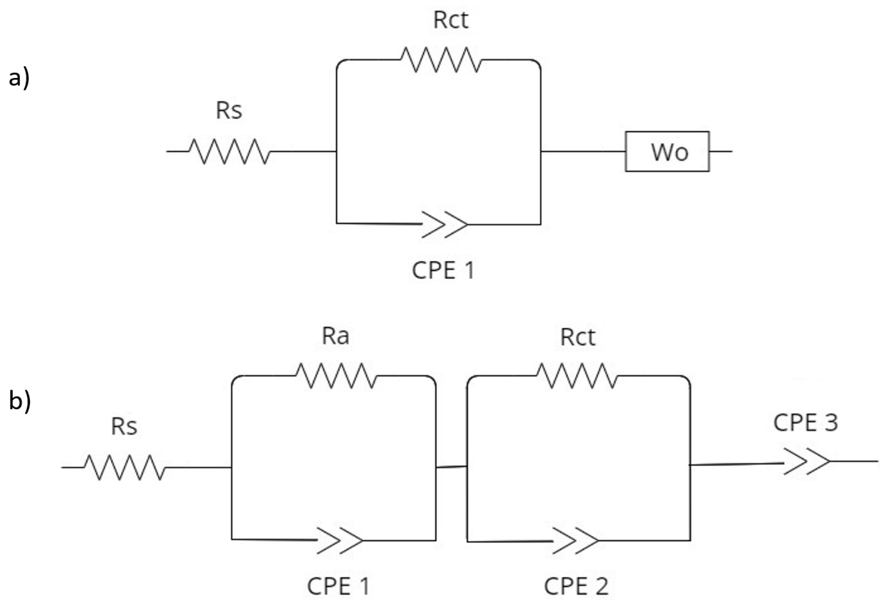

Figure 4.8: Equivalent circuit model for the impedance spectra after a) 1st cycle, b) 75th cycle.

From the spectra, it can be observed that after the first cycle, there is a large semicircle, which indicates a high charge transfer resistance and less Li$^+$ diffusion at the surface [129]. This large semicircle could also be due to the thin SEI layer that forms during this cycle which does not completely cover the surface of the lithium anode. This thin SEI functions as an interfacial resistance layer [130]. The lithium diffusion is represented in the circuit as a Warburg element. This Warburg element is a constant phase element with an angle of 45°.

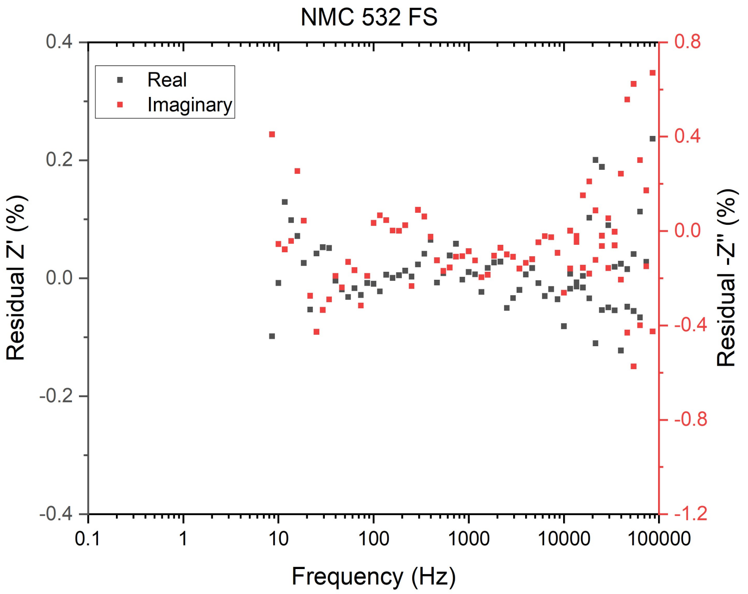

Figure 4.9: KKT results of NMC 532 FS sample after 75th cycle.

Upon further cycling, there is a CEI layer which gets formed on the cathode, which is represented in the circuit as an additional R-P element. The significant decrease in the semi circle associated with charge transfer resistance over cycling, could be a result of increased lithium dendrite formation on the anode [131, 132]. Additionally, it is evident that the Warburg element transforms into a constant phase element with cycling. A high impedance after cycling could indicate intergranular cracking as a result of continuous electrolyte decomposition, which causes reduced electrical contact and accumulation of CEI layers [133].

All the obtained spectra are evaluated with KKT to determine their validity. The KKT results for NMC 532 FS sample is shown in fig 4.10. From the KKT plot, we can observe that the residuals fall well within the 1% limit, except for high frequency regions. This could be due to the parasitic capacitance, which forms if different electric components are in close proximity within an electric circuit [134]. The other cathode samples follow a similar trend (fig A.2).

The impedance spectra for both Al and FS cathodes show the formation of the CEI layer with cycling. The spectra for both cathodes follow the same circuit model. Overall, it can be said that the FS cathodes and the cathodes on the aluminium current collector show a comparable impedance behaviour.

4.3.5. SEM Results for NMC and LCO Cathodes

The surface of the NMC and LCO cathodes after long term cycling is studied by SEM, in order to attribute for the capacity fading that was seen during cycling. The images would help in studying fragmentation and crack evolution of the cathodes. The results from SEM are shown below.

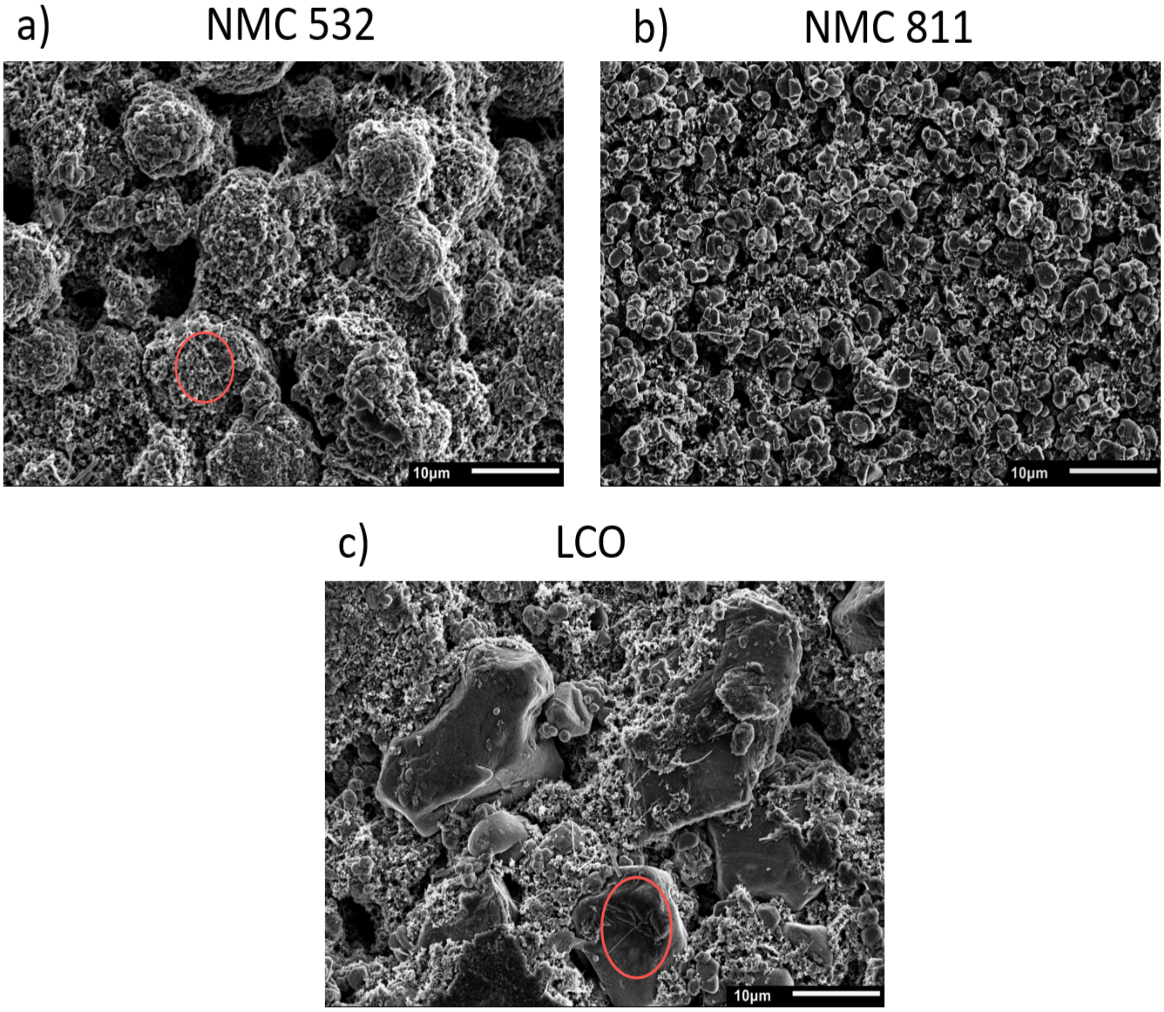

Figure 4.10: SEM micrographs of FS a) NMC 532, b) NMC 811 and c) LCO cathode surfaces obtained after long term cycling. The images are taken at 2000x magnification and 5 kV acceleration voltage.

From the above images, it is evident that the NMC 532 and LCO cathodes show the occurrence of microcracks and particle disintegration (highlighted in red), after long term cycling. Due to the NMC 811's small particle sizes, which were harder to observe under SEM, surface analysis of these particles produced no clear results.

The increase in surface area of cathode material exposed to the electrolyte over long term cycling, caused the majority of secondary particles to break entirely into primary crystallites. This produced additional surfaces for further electrolyte decomposition and CEI production in the NMC and LCO cathodes. As a result, the impedance increased, performance degraded, and capacity faded. This phenomenon also causes loss in the interparticle connections, which contributed to the increasing peak shift as observed in the the dQ/dV plots [135]. These cracks were also observed on cathodes on aluminium current collector (see fig A.4), which proves that both FS and Al cathodes encounter a similar loss in structural integrity over long term cycling.

The presence of microcracks on the cathode surface could lead to an increase in the strain, as a result of lattice expansion and contraction, which might have an impact on the cathode's crystal and electronic structure [136, 137]. Additionally, SEM measurements were also done on the cathode samples after 1 cycle, in which there were no presence of cracks observed. This asserts that, in accordance with literature, cracks grow particularly after long term cycling [83].

4.3.6. XRD Results

As discussed in the previous section, the presence of microcracks on the surface of the cathodes could lead to strain on the sample. This increased strain changes the lattice parameters upon cycling and causes shifts in the diffraction peaks [136]. To investigate this phenomenon, the cathode powders and the cycled cathodes are analysed through XRD. The results for the powder samples are shown in fig 4.11. The pattern on the top right of every image is the zoomed image of the highlighted region in the main pattern.

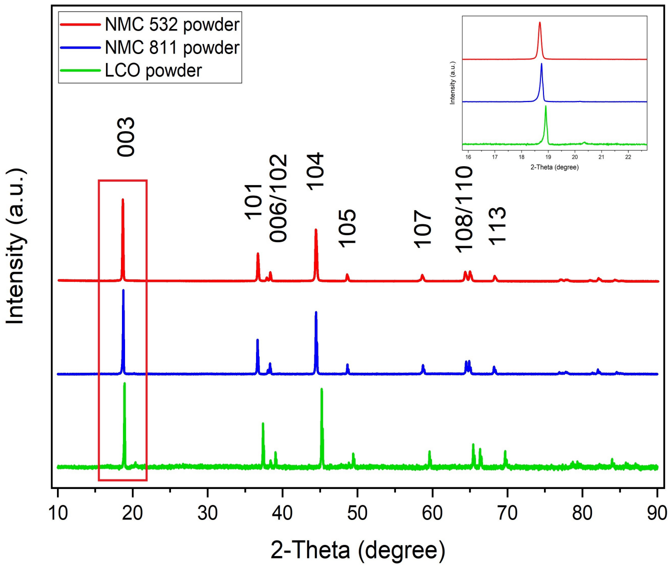

Figure 4.11: XRD patterns of *NMC 532, NMC 811 and LCO powders.
*The measurement for NMC 532 was performed using a monochromator for 15 hrs, while measurements for NMC 811 and LCO were performed using a anti-scatter slit for 2 hrs. An open sample holder was used for all the measurements.

The XRD patterns for the powder samples are shown above. The pattern consists of a series of peaks at different 2-Theta angles. All the powder samples were well indexed to a α-$NaFeO_2$ hexagonal layered structure with a R-3m space group. The main characteristic peaks in all the samples agree to the 003, 101, 006, 102, 104, 105, 107, 108, 110 and 113 planes at 18.7° 36.6°, 38° , 38.1°, 44.5°, 48.7°, 58.8°, 64.6°, 64.8°, 68.2°, respectively [136].

There was no additional peak observed in the measurements, indicating no crystalline impurity or second phase present in the powder samples. The splitting of the 006/102 and 108/110 peaks in all the powder samples indicate an ordered hexagonal layered structure [127]. The 003, 101 and 110 peaks are very indicative of the changes in the lattice structure upon cycling. While the 003 peak studies the evolution of c parameter, the remaining two peaks study the evolution of a and b lattice parameters [138]. The powders, made into FS cathodes, were tested for XRD after electrochemical cycling. The results are shown in fig 4.12.

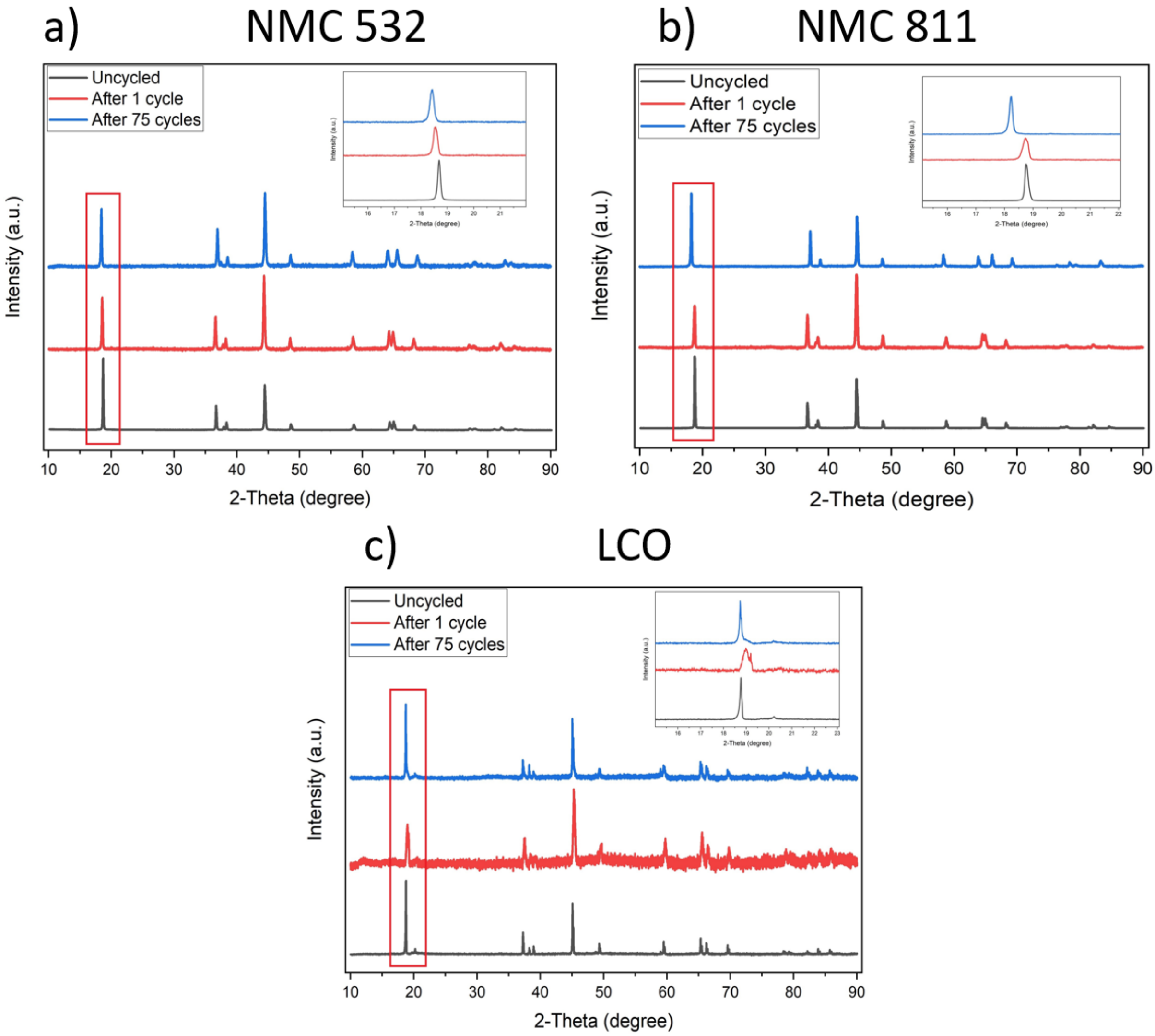

Figure 4.12: XRD patterns of FS *a) NMC 532, b) NMC 811 and c) LCO cathodes before cycling, **after 1st and 75th cycle.
*The uncycled NMC 532 and NMC 811 cathodes were measured with a monochromator for 15 hrs in an open sample holder. The LCO cathode after 1 cycle was measured with an anti-scatter slit using an air-tight sample holder. The remaining samples were measured for 2 hrs with an anti-scatter slit in an open sample holder.
** 1st cycle is at 0.1C while the 75th cycle is at 1C

During long-term cycling, notably comparing the 1st and 75th cycles, we can see a considerable peak shift (003) for the NMC and LCO cathodes in the figure. After cycling, the peak for a cathode sample initially shifts to lower 2-Theta values. This shift denotes the expansion of the unit cell in the c-direction. Long-term cycling causes this peak to gradually shift to higher 2-Theta values [136]. The shift could be due to displacement error caused due to the changes in the height of sample used during the XRD measurement. Over cycling, it can be seen that the peaks broaden, which could indicate the presence of microstrain on the samples [139, 140]. The degree of peak shift and peak broadening is important to assess the structural behaviour of the sample. To verify this, Rietveld refinement is done on the samples to attribute for displacement or strain.

Furthermore, the Ni^{2+} or Co^{3+} occupancy on Li^{+} sites, in the layered oxide can be effectively identified through the peak intensity ratio of (003)/(104) i.e (I_{003}/I_{004}). This ratio provides an estimate of the degree of cation disorder in the bulk of the cathode samples. If I_{003}/I_{004} is less than 1.2, the degree of cation mixing is high [141, 142, 143]. However, it has also been stated that this ratio lacks the ability to distinguish between Li/Ni, Li/Co, and Li/Mn cation mixing and cannot precisely reflect the degree of cation mixing. The peak intensity obtained is dependent on equipment and test conditions, and does not accurately represent the changes in the bulk of the sample. In order to provide an estimate of the degree of cation mixing, the obtained diffraction patterns are refined [144]. The result for the refinement of NMC 532 FS after 75 cycles is shown below. For the other refinement results, please refer to fig A.5.

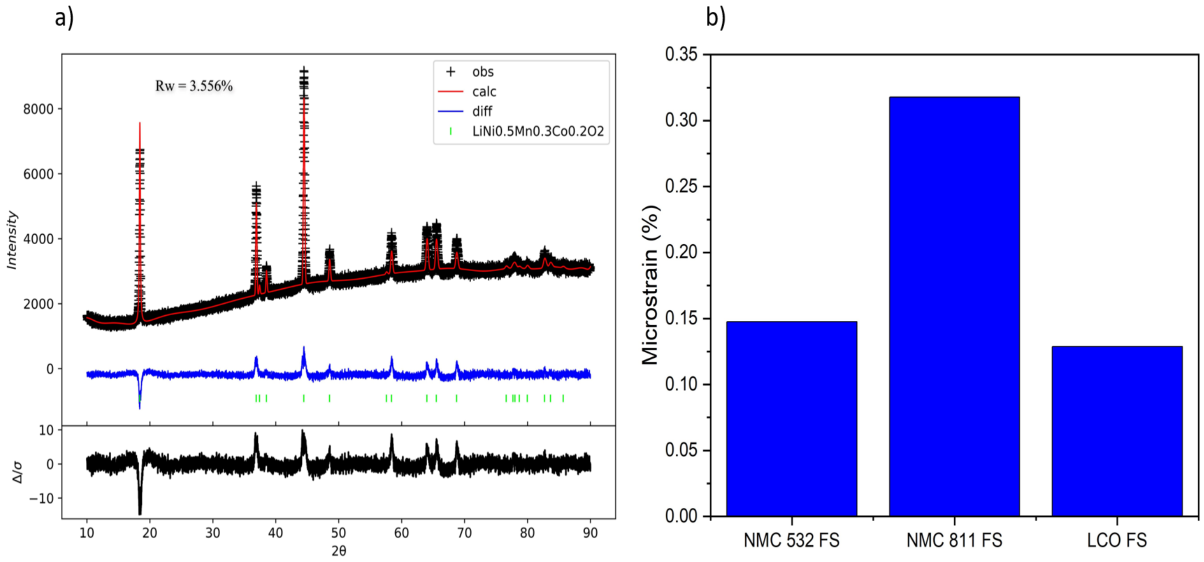

Figure 4.13: a) Rietveld refinement result for NMC 532 FS cathode after 75 cycles. b) The obtained microstrain values for NMC and LCO cathodes after 75 cycles, from refinement.

From the refinement, it was observed that there were minor values of microstrain observed in all the cathodes after 75 cycles, as shown in fig 4.13b. This could be correlated to the formation of cracks on the surface as observed in SEM, which results in microstrain. This microstrain was not observed on the cathode samples after 1 cycle. The refinement also did not indicate any change in the spinel structure for all the cathodes after cycling. Thus, the original structure was retained after cycling without any significant phase transformations. However, continued prolonged cycling or cycling at higher potentials could have resulted in the phase transformation and formation of rock salt structure [145].

The table containing lattice parameters obtained after refinement is shown in table A.1. Following refinement, the lattice parameters obtained have a certain standard deviation, depending on the refinement. During delithiation, the lattice parameters a and b contract while c expands. While the former relates to the decreasing cation radius of transition metals in their high oxidation states, the latter results from the repulsive force caused by the metal oxide layers as a result of extraction of lithium ions from the lithium layers. During lithiation, the changes in the lattice parameters reverse. This expansion and contraction occurs repeatedly over lithiation and delithiation during cycling to cause capacity fading, structural deterioration or phase transformations [138]. On the other hand, the peak shift and the change in the lattice parameters could also be a result of electrolyte decomposition, which results in the loss of lattice oxygen causing capacity to fade [146, 147], due to an unstable CEI. To further investigate this, XPS is performed on the surface of the uncycled and cycled cathodes, which is presented in the next section.

4.3.7. XPS Results

It was discovered by XRD analysis that the NMC and LCO cathodes exhibit microstrain, which could have been induced by the cathodes developing cracks on their surfaces during long term cycling. This could be due to the structural instability of the CEI layer, which might lead to contaminants forming on cathode surfaces as a consequence of electrolyte decomposition. To study the evolution of the cathode surface over cycling, XPS is performed. Initially, the powder samples are subjected to XPS to check the presence of any surface impurities. The results are shown in fig 4.14.

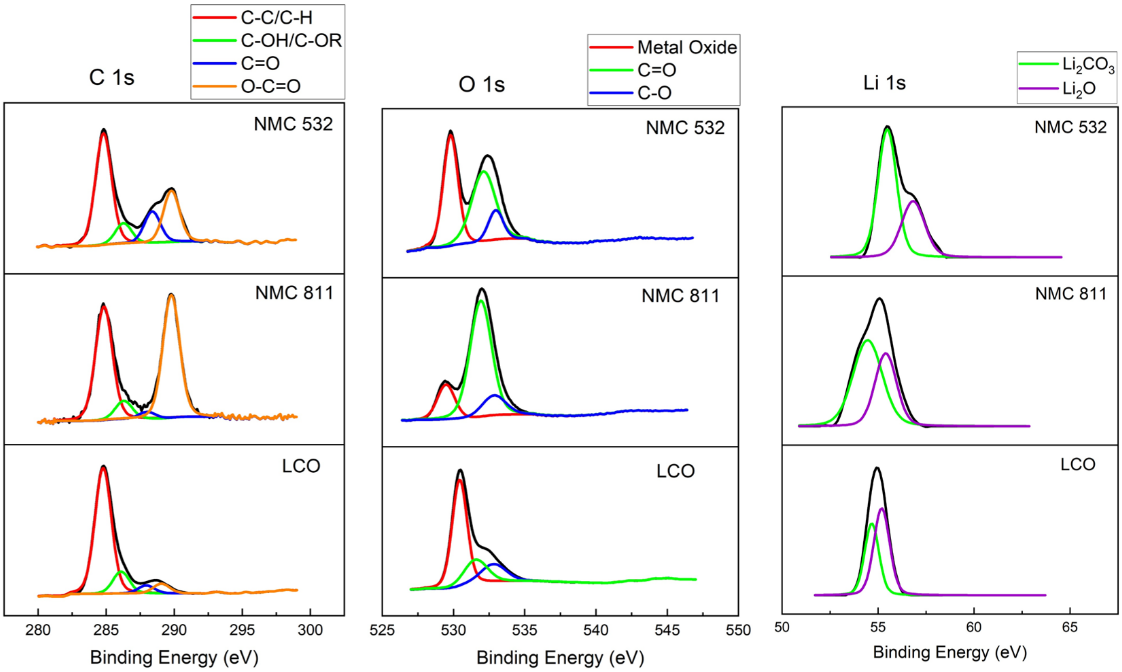

Figure 4.14: Fitted photoelectron spectra of (from left to right) C 1s, O 1s and Li 1s for NMC 532, NMC 811 and LCO powder samples.

Firstly, the C 1s scan contains four different peaks, the C-C/C-H peak at 284.8 eV is due to the presence of adventitious carbon, found on the cathode powders. The peak at 286.3 eV corresponds to C-O, which could be a result of C-O bonds in the carbon layer or due to the presence of carbonate species. The peaks at 288.3 eV and 289.6 eV correspond to C=O and O-C=O, respectively, which results from reaction of surface Li_2O with H_2O and CO_2 from moisture air during storage, to form Li_2CO_3 [148, 149].

Secondly, the O 1s scan shows three distinctive peaks, one at 529.2 eV which is assigned to the lattice oxygen bond (Ni-O, Co-O or Mn-O) in the NMCs and LCO. The peak at 532 eV is attributed to C=O which is from Li_2CO_3 residual on the surface of the sample. This C=O peak from the carbonate layer could not be detected by XRD because it could be amorphous and thin [150]. The third peak at 533.2 eV is attributed to C-O, which has contributions from the C-O bonds in the adventitious carbon layer and in the carbonate residuals.

The Li 1s scan depicts two peaks, one each at 54.8 eV and 56.2 eV, which indicate the presence of Li_2CO_3 and Li_2O, respectively on the powder surfaces. The presence of Li_2CO_3 peak is in agreement with the peaks obtained in C 1s and O 1s scans as seen above.

The peaks of Ni 2p for NMCs and Co 2p for LCO were fitted in both their 3/2 and 1/2 orbital states (fig A.7). For the NMCs, the Ni 2p 3/2 scan consists of two peaks corresponding to Ni^{2+} and Ni^{3+} at 854.2 eV and 855.1 eV, respectively. In LCO, the Co 2p 3/2 scan consists of two peaks of Co^{3+} and Co^{4+} at 779 eV and 780.1 eV, respectively. A higher amount of Ni^{2+} and Co^{3+} were present in the NMC and LCO samples, respectively which oxidises to a higher valence state upon cycling. This is concurrent with literature [105], where in NMCs, the Ni exists in +2 and +3 valence states, while Co and Mn exist in +3 and +4 valence states, respectively. In LCO, Co exists in multivalent valence states, but more predominantly in +3 and +4 valence states. The scans for Co and Mn in NMCs had a high background, which could be due to lower abundance of these elements on the surface of the powders [105]. Due to their high background, the scans of transition metal elements provided no conclusive results.

From the analysis of the powders, there exists a significant proportion of Li_2CO_3 residuals on the surface of the samples. These powders are then made into cathodes and cycled for long term as shown in section 4.3.2. The XPS scans for the cathodes before and after cycling are shown below.

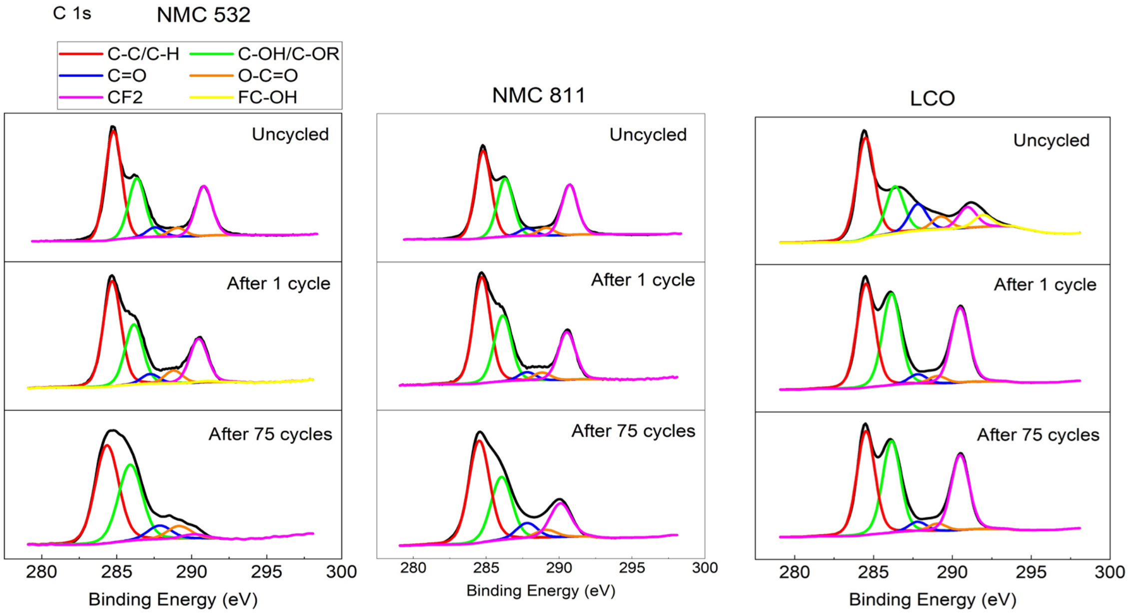

Figure 4.15: Fitted C 1s spectra of NMC 532, NMC 811 and LCO cathodes before cycling, after 1 cycle and after 75 cycles.

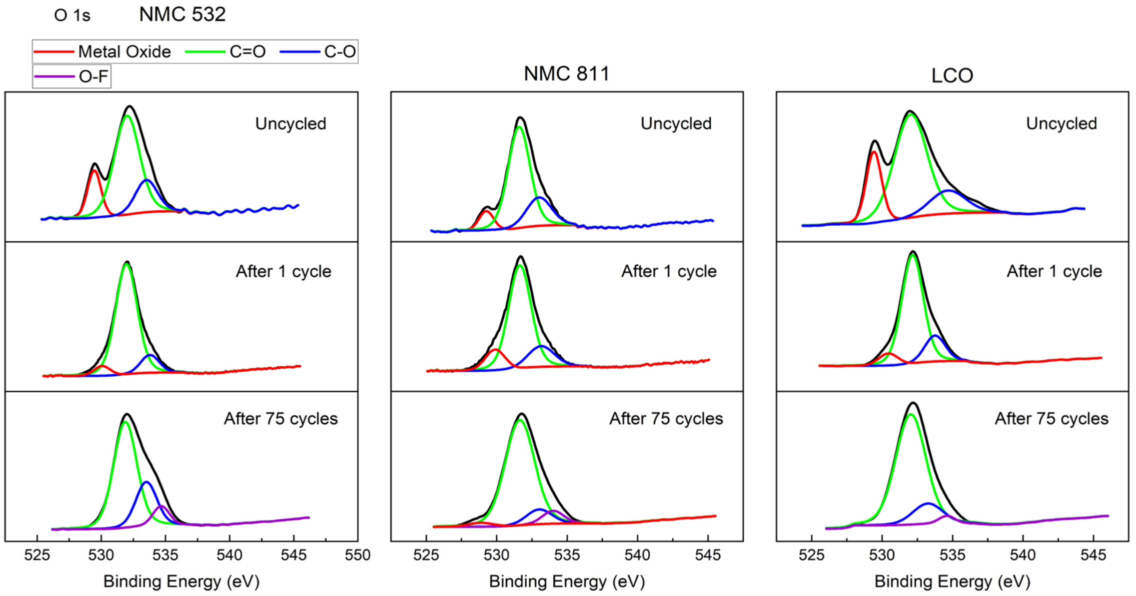

Figure 4.16: Fitted O 1s spectra of NMC 532, NMC 811 and LCO cathodes before cycling, after 1 cycle and after 75 cycles.

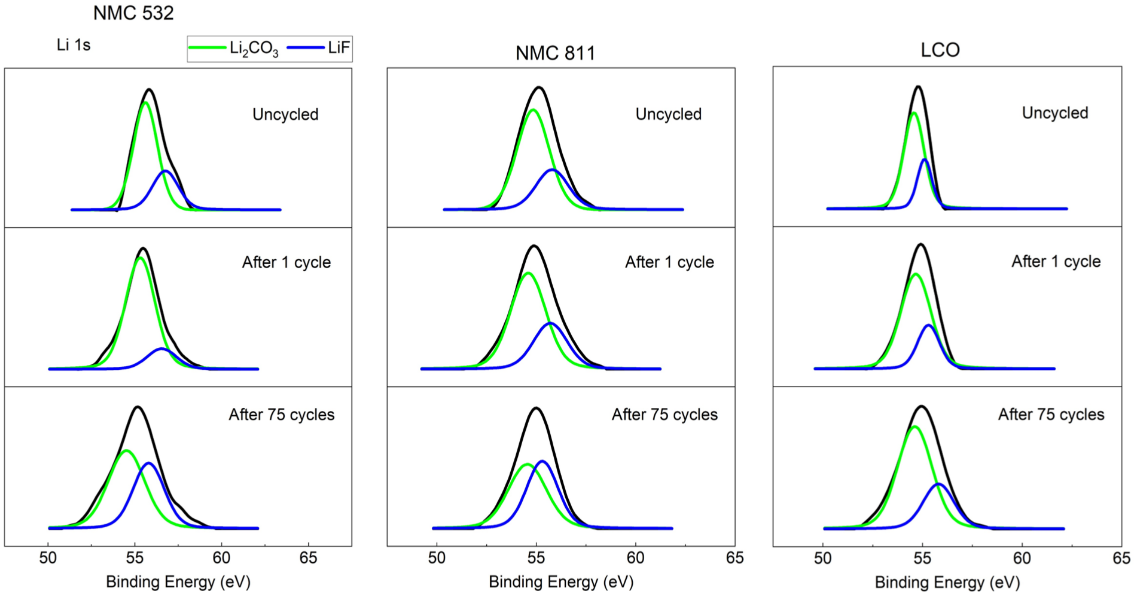

Figure 4.17: Fitted Li 1s spectra of NMC 532, NMC 811 and LCO cathodes before cycling, after 1 cycle and after 75 cycles.

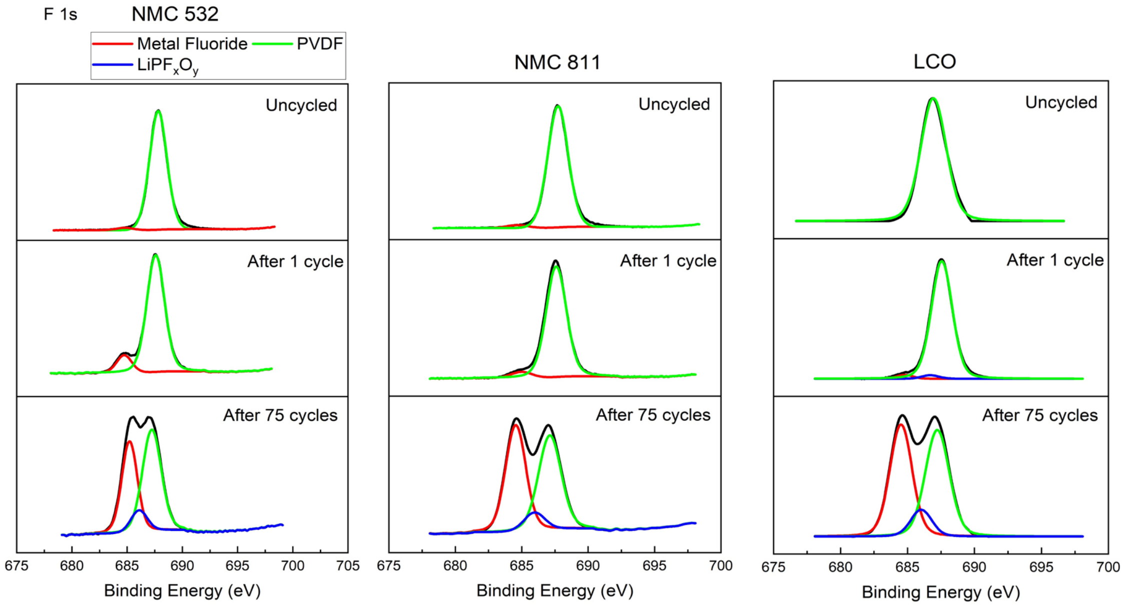

Figure 4.18: Fitted F 1s spectra of NMC 532, NMC 811 and LCO cathodes before cycling, after 1 cycle and after 75 cycles.

The XPS scans of cathodes before cycling, after 1 cycle and after 75 cycles are shown above. For a cycled cathode, the decomposition of electrolyte results in the presence of C=O, O=C-O, O-F and Li-F components on the CEI layer. The decomposition of electrolyte gives rise to $ROCO_2Li$, $LiPF_xO_y$ and Li_2CO_3 products [133]. Understanding the elemental compositions of these components will provide an idea about the extent of electrolyte decomposition in the cell.

In the C 1s spectra, there is a CF_2 peak at 290.5 eV and a FC-OH peak at 291.4 eV, which are due to the presence of PVDF in the cathode. The C-O peak is related to the presence of carbon black in the cathode [148]. After cycling, it is observed that the peaks attributed to C=O and O-C=O are significantly present in the NMC and LCO cathodes, indicating formation of $ROCO_2Li$ or Li_2CO_3, which are dominant in the CEI film. For the uncycled electrode, the peaks of C=O and O-C=O arise from the reaction with moisture.

The O 1s scan shows a sharp peak for C=O in the cathodes after 75 cycles, which indicates an increased decomposition of the electrolyte, forming inorganic lithium salts on the surface of the cathode. The peak for metal oxide indicates the presence of oxygen atoms in the NMC and LCO crystal lattice. Over cycling, this peak decreased, indicating the formation of a thicker CEI layer [151], with limited lithium diffusion. The peak at 534.8 eV attributed to O-F, indicates the presence of an inorganic layer comprising of transition metal fluorophosphates ($LiPF_xO_y$), which is a product of electrolyte decomposition. This peak can be observed in all the cathode samples after cycling, implying that long term cycling produces decomposition products on the cathode surface.

It is stated that for a stable CEI, having an appropriate content of Li_2CO_3 improves the stability of the interface upon cycling [133]. We therefore examine other contaminants in order to properly account for electrolyte decomposition in all the samples. In the Li 1s scan, there is a peak attributed to LiF, which occurs at 56.8 eV. For the uncycled cathodes, this could be from the electrode fabrication, which facilitates a reaction between LiOH/Li_2CO_3 present on the cathode surface and PVDF [148]. However, the increased presence of this peak after 75 cycles denotes salt decomposition in the cathodes. After 1 cycle, we observe a sharp peak for LiF in the Li 1s scan. This was the only surface contaminant which is observed after the formation cycle, in the XPS scans. The other contaminants are majorly observed to form after long term cycling.

The F 1s scan shows three peaks. The peak at 684.8 eV corresponds to the presence of metal fluoride. The second peak at 685.6 eV denotes the presence of $LiPF_xO_y$, which is formed due to electrolyte decomposition. The third peak at 687.5 eV represents PVDF.

Moreover, after cycling, it can be seen that the Ni^{2+}/Ni^{3+} ratios and Co^{3+}/Co^{4+} ratio become smaller in NMCs and LCO, respectively (from fig A.8 and fig A.10). This could be due to the loss of lithium ions from the NMC and LCO lattice, causing an increase in Ni/Co oxidation states [105].

From the above results, the electrolyte decomposition over long term cycling produced decomposition products on the cathodes' surface. The presence of these products were indicated by their respective peaks in the elemental scans. These contaminants formed as a result of a poor CEI layer, causing capacity fading, as seen in the earlier subsections.

4.4. Conclusion

In this chapter, the FS cathodes were cycled for rate test and long term cycling test. Their results were contrasted with cathodes on aluminium current collector. The changes in resistance over cycling were then assessed using EIS on these cathodes. Post that, the cathodes were investigated using SEM, XRD, and XPS to account for changes in their surface as a result of long term cycling.

The FS cathodes' cycling performance was comparable to that of cathodes on an aluminium current collector, which provided the motivation to use them for the spectroscopic studies, in this work. This aids in achieving an accurate result for elemental compositions, devoid of any current collector interference. Furthermore, the cathodes noticed capacity degradation during the course of long term cycling, which increased the charge transfer resistance and limited the diffusion of lithium ions. This was a result of an unstable CEI layer, which caused the electrolyte to decompose, resulting in the formation of contaminants on the cathode surface. This phenomenon led to the formation of microcracks on the cathode particles, which resulted in microstrain on these samples. The performance of the LIB half cells was impacted by these occurrences, causing their capacity to fade during cycling.

This capacity fading and structural instability can be overcome through surface modification of the cathode. Coating the cathode surface with Al_2O_3 using ALD has proven to be a successful technique to enhance the cycling performance of the LIB cathodes [152]. The performance of the cells after ALD coating is examined in the following chapter, which focuses exclusively on the ALD coated cathodes.

5

Impact of Atomic Layer Deposition on LIB Cathodes

5.1. Introduction

In the previous chapter, it was seen that the NMC and LCO cathodes experience a loss in their structural integrity, when subjected to long term cycling. The battery's performance deteriorated as a result, which places restrictions on the cathodes' use in commercial applications. In order to prevent this, the cathode surfaces are modified using several coating techniques. In this work, the cathode active materials i.e. NMC 532, NMC 811 and LCO are coated with Al_2O_3 using ALD.

Specifically, we investigate two different ALD coatings, 10 ALD and 30 ALD cycles, which roughly have thickness of 1 nm and 3 nm, respectively. The cathode active materials were coated in a fluidised bed reactor to achieve a conformal coating. It has been proven that the coating thickness plays an important role in the performance of a cathode. To strike a balance between preserving structural integrity and reducing electrochemical impedance, an optimised coating thickness is required [153]. This chapter focuses on the process of coating Al_2O_3 using ALD, and further investigates the cycling performance of the coated cathodes. The structural stability of these coated cathodes is further evaluated using SEM, XRD, and XPS. Finally, the 30 ALD cathodes are tested with NMR to validate the changes in the aluminium environment, as a function of cycling.

5.2. Materials and Methods

5.2.1. Materials

This section details the process of making an ALD coated FS cathode, which differs moderately from the uncoated FS cathode, described in the previous chapter. Moreover, it also describes the ALD coating process, along with the theory behind the characterization techniques used.

Characterization of the ALD Coating Process

ALD is a thermally activated gas phase technique that uses two or more gaseous reactants to coat a cathode powder. These gaseous reactants are concentrated on the sample, leading to self-limiting chemisorption surface reactions. Typically, the procedure calls for the separate dosing of a metal organic precursor and an oxidising co-reactant in a fluidised bed reactor. In order to help remove excess precursors and byproducts, high quality nitrogen is employed as a purging gas inside the reactor. The following steps represent the deposition process [154]:

1. The sample is placed in the fluidised bed reactor and is heated to an optimal temperature.
2. Following this, the precursor and co-reactant are added to the reactor under a specific dosing pressure, which is followed by purging the nitrogen gas within the chamber.
3. The co-reactant used is deionised water, while the precursor is Trimethylaluminium (TMA). TMA reacts with the hydroxyl group present in water, resulting in a CH_3 terminated surface, which then reacts again with the second co-reactant in a self limiting manner, to produce a layer of Al_2O_3. The reaction is shown below [154].

$$\text{AlOH} + \text{Al}\left(\text{CH}_3\right)_3 \rightarrow \text{AlO} - \text{Al}\left(\text{CH}_3\right)_2 + \text{CH}_4 \tag{5.1}$$

$$\text{Al}\left(\text{CH}_3\right)_2 + \text{H}_2\text{O} \rightarrow \text{AlOH} + \text{CH}_4 \tag{5.2}$$

4. The excess precursors and by products are removed by purging the inert nitrogen gas. This process produces one cycle of Al_2O_3 on the powder surface. More such cycles produce a thicker layer. A schematic of the ALD coating process is shown in fig 5.1.

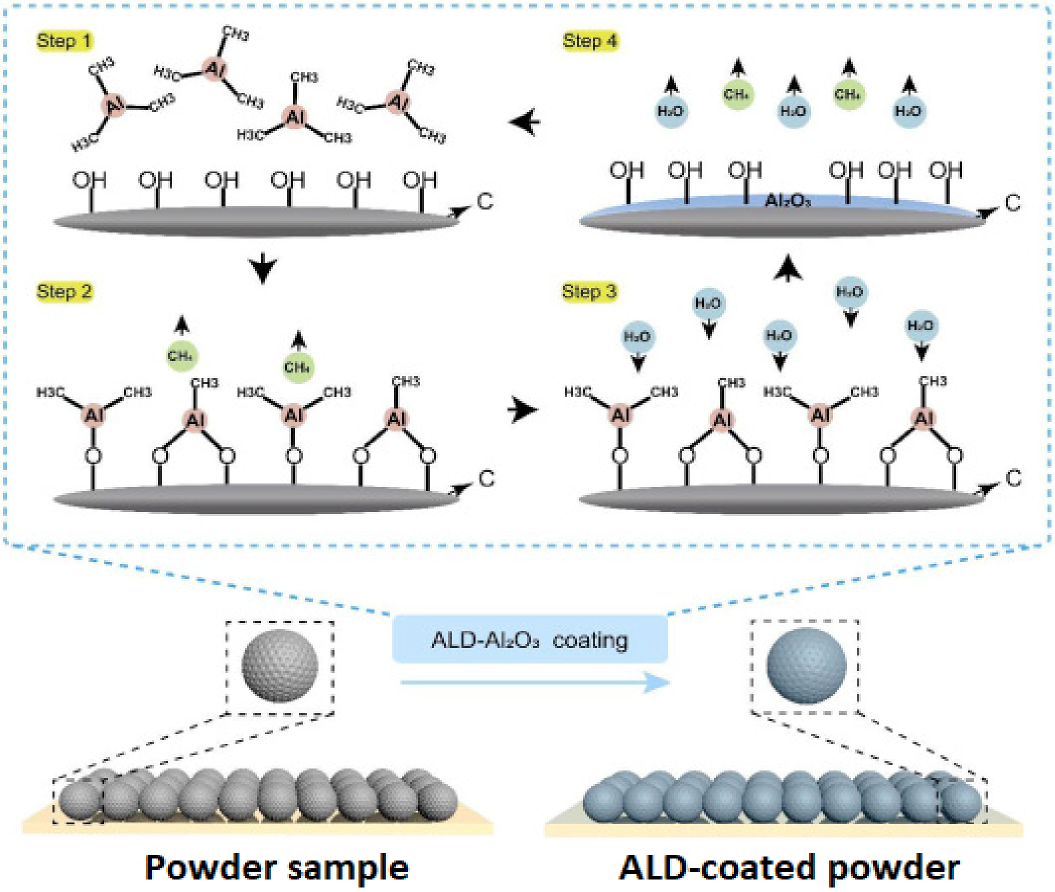

Figure 5.1: ALD process for depositing Al_2O_3 on the cathode powders. Adapted from [155].

For this study, the ALD coating for the cathode powders were performed by Powall B.V.

Making an ALD-Coated Cathode

The process of making an ALD coated cathode follows a similar sequence of steps as making an uncoated cathode described in the previous chapter. The major change, however, lies in the composition of the powder materials used to prepare the slurry. Since the goal of this work is to create FS cathodes, the cathodes' extractability after drying is essential in order to employ them for subsequent testing. The presence of Al_2O_3 layer causes a high adhesion to the coating surface [156]. This limits the cathode slurry's ability to be extracted from the release liner, when the slurry for the ALD coated cathodes were made with the same composition as the uncoated cathodes, in this work. As a result, more binder is needed to assist deliver a homogeneous slurry and keep the active material particles intact within the cathode [157].

Hence, for the above reason we use 1 wt% of PVDF binder (Solef 5130), and 8.5 wt% of active material. The composition of Super C45 (TIMCAL) and carbon nanofiber (Aldrich, >98%) used are 0.45 wt% and 0.05 wt%, respectively. The NMP (Thermo Scientific, 99.5 %) is added in a volume ratio of 1:1 with the active material to make a homogenous slurry. This slurry is then vacuum dried and coated over a 15 μm Al foil for cathodes with aluminium current collector, while it coated onto a release liner to generate a FS cathode. The cathodes are then pressed using a hydraulic press (Carver, 973214A), with 400 MPa pressure and cut into circular disks of 11.1 mm in diameter.

The FS cathode disks weigh between 9 mg to 12 mg, having a thickness between 42 μm to 50 μm. On the other hand, the cathodes on aluminium current collector weigh between 13 mg to 17 mg, with a thickness ranging from 60 μm to 65 μm, after pressing.

5.2.2. Methods

Cycling an ALD Coated Cathode

In this work, the ALD coated cathodes are used in a half cell, consisting of lithium metal as anode. The half cells undergo one of two tests: rate test and long term cycling. As described in the previous chapter, the rate test is performed at five different C rates (0.1 C, 0.5 C, 1 C, 2 C and 5 C) for five cycles each, and finally at 0.1 C for three cycles to test the cells' capacity retention. In addition to 150 cycles at 1 C rate, two formation cycles at 0.1 C, and two final cycles at 0.1 C are all performed as part of the long term cycling test. The long term cycling is carried out with CC-CV. For the FS cathodes, due to channel constraints, this long term cycling is capped at 75 cycles at 1 C rate. In this work, three cells were tested for each cathode, in order to get an error estimate of their capacities during cycling.

The cut-off voltage for the NMC 532 and LCO cathodes is 2.0-4.2 V, while for the NMC 811 cathodes, it is 2.0-4.3 V. For transition metal oxide cathodes, the UCP is crucial because capacity fade is accelerated at high UCPs. As a result, we choose a UCP of 4.2 V for NMC 532 and LCO and 4.3 V for NMC 811 [82]. The theoretical capacities for the three cathodes - NMC 532, NMC 811, and LCO are, respectively, 166 mAh/g, 190 mAh/g, and 140 mAh/g [83, 84].

Post cycling, a dQ/dV analysis is performed on the cells to validate the stability of the oxidation and reduction peaks over cycling. The dQ/dV curve is derived from the charge-discharge curve from the long term cycling in LANHE battery tester, which calculates the capacity for every incremental change of voltage. This evaluation gives a sense of the extent of degradation that is occurring within the cell [86].

EIS on ALD Coated Cathodes

In this work, the cathode active materials are coated by ALD-Al_2O_3, to improve their performance during long term cycling. However, the presence of a coating layer could also negatively impact the cathode's electrochemical impedance [153]. To have a better understanding of the impacts of utilising Al_2O_3 as a coating, EIS is performed.

The EIS measurements for ALD coated cathodes are performed at room temperature and at OCP. The measurements cover a frequency range of 0.1 Hz to 100 kHz. The measurements are carried out with 15 frequency points per decade and with a V_{rms} value of 0.005 V. The EIS measurements are performed on a Metrohm Autolab device (PGSTAT302N with an FRA32M module) and the resulting spectra are analysed using RelaxIS software [90]. Furthermore, the spectra obtained following EIS measurements are validated using KKT, just like the the uncoated cathodes described in the preceding chapter.

Probing the Microstructure of ALD Coated Cathodes using SEM-EDS

To further examine the conformality of ALD coating, the morphological features of ALD coated cathodes are characterised using a SEM (JEOL JSM-IT100) coupled with EDS operated at 5 kV acceleration voltage. To get a high resolution image, the working distance for the measurement is set between 11 mm and 13 mm. Since the ALD coated samples contain an alumina layer on the cathode surface, a high surface detail is required in the SEM image. To facilitate this, a SED is used for the SEM measurement [94]. The sample preparation for SEM observation is done by directly mounting sufficient amounts of a dry powder or a cathode onto a conductive carbon tape in ambient air. All the cathodes tested after cycling are washed with DMC (Sigma-Aldrich, >99 %) to remove any excess electrolyte present on the surface of the cathodes, which could otherwise cause hindrance during measurements [108].

After SEM imaging, the samples undergo an EDS analysis to determine how much the composition of the elements, including aluminium has changed as a result of cycling. The EDS is mapped over a specific area in the sample to obtain its elemental compositions.

XRD Characterization on ALD Coated Samples

XRD is used to investigate the crystallographic structure of the ALD coated powders and cathodes, which provide information on the phase transformation and structural changes in the sample microstructure. Moreover, this is done to understand if the ALD process affected the crystallinity of the cathode powders, which is useful to assess the nature of the coating layer [158, 97].

The XRD measurements are performed at room temperature and its patterns are obtained using a PANalytical X'Pert Pro system, using Cu Kα radiation (at 45 kV and 40 mA). The diffraction data were collected in the 2θ range between 10° to 90°. The analysis and refinement of the XRD peaks are performed using Match and GSAS-II software, respectively [103, 104]. In GSAS-II, least square refinement is applied to the measured sample in order to acquire the lattice parameters. To conduct the measurement, either an open sample holder or an air-tight sample holder is used. For specific measurements, a monochromator is used, which minimises the fluorescence caused due to the presence of cobalt in the Cu Kα radiation, and help obtain a clear spectrum [102, 101].

XPS Investigation on ALD Coated Samples

To verify the deposition of Al_2O_3 coating on the surface of the LCO and NMC cathodes, XPS is performed. With this method, the surface elements are characterised, and their changes during electrochemical cycling are examined. XPS provides an insight into the factors that affect the chemical composition of the CEI, which has an impact on the coulombic efficiency and cycling performance of the cathodes [159].

The XPS measurements for ALD coated samples are performed at room temperature and at high vacuum using a K-Alpha Thermo Scientific XPS apparatus. Al Kα radiation (1486 eV) from a monochromatised X-ray source is used for the measurements. The cycled cathode samples are washed with DMC to remove the impurities on their surface, before testing them for XPS. The obtained scans are processed using Casa XPS software [109]. To process the data, the binding energies of the samples are corrected according to the C 1s adventitious carbon peak at 248.8 eV [110]. The data obtained is initially smoothed using a Savitsky-Golay quadratic method to remove excess background. This is then fitted using weighted least squares method, containing both Gaussian and Lorentzian line shapes.

Some of the XPS measurements in this work were performed by PTG Eindhoven B.V. These include:

- NMC 532 (10 ALD and 30 ALD) powders
- NMC 811 (10 ALD and 30 ALD) powders
- NMC 532, NMC 811 and LCO cathodes before cycling (10 ALD and 30 ALD)
- NMC 532, NMC 811 and LCO cathodes after 1 cycle (10 ALD and 30 ALD).

NMR Studies of ALD Coated Cathodes

Solid-state NMR spectra can reveal a plethora of local structural information, resulting from magnetic interactions between the intended nuclei and their surrounding chemical environment. Some of the important interactions include [160, 161]:

- Chemical shift: In this shift, the chemically distinct nuclei show up as separate resonances in the NMR spectrum. In the ^{27}Al NMR, the signals from the compounds with high coordination number appear at the higher fields, while low coordination number compounds produce signals which resonate at lower fields, owing to chemical shift.
- Dipolar interaction: This is a short range, through-space magnetic interaction between nuclei. This interaction gives information about the short range proximities in materials.
- Quadrupolar interaction: The electric field gradient at the nuclear position interacts with the quadrupole moment of the nucleus, resulting in the quadrupolar interaction. This can be used to learn more about the distortions and the local bonding geometry.
- Paramagnetic interaction: This results from through-space and through-bond interactions between the magnetic moment of the nucleus and unpaired electrons, which has the ability to shift resonances from hundreds or thousands of ppm.

In this work, the NMR investigation on the cathodes is predominantly catered to studying the ^{27}Al nuclei, while ^{7}Li is explored as an addition, specifically for LCO cathodes. The NMR measurement in this work is performed using Magic Angle Spinning (MAS), which helps acquire a high resolution spectra by removing the anisotropic interactions from the spectra [162]. Furthermore, this provides useful information on the local structure of aluminium in the ^{27}Al NMR, through the dependability of the chemical shift on the local coordination environment. In general, four-, five- and six-coordinate Al-O species have chemical shift ranges of 50 to 80 ppm, 30 to 40 ppm, and 10 to 15 ppm, respectively [160].

Some of the important parameters which influence the quality of the NMR spectrum include quadrupole parameters, nuclear spin relaxation, spinning speed, pulse sequence and magnetic field during measurement. To avoid any overlap of the central line and spinning side bands during the measurement, it is crucial to select the right combination of spinning speed and external field strength [162].

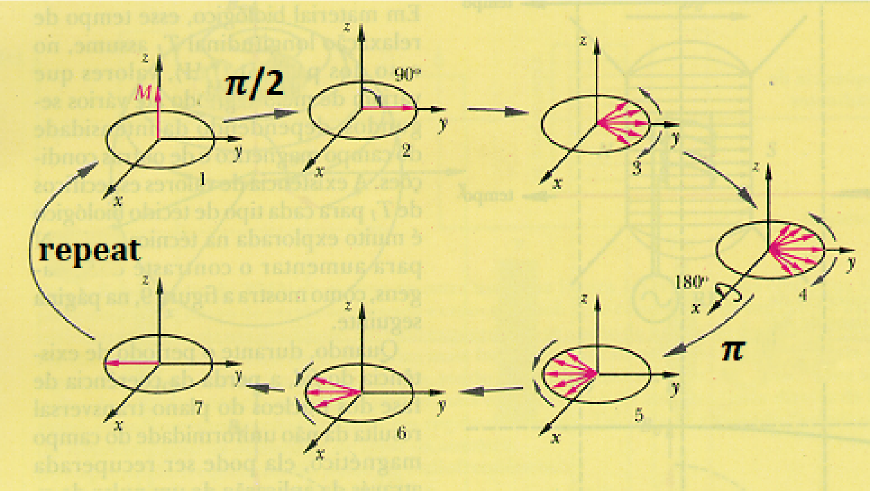

Figure 5.2: Demonstration of a Hahn-echo pulse sequence. Adapted from [163].

Under MAS, a typical NMR spectrum will have a central peak and spinning sidebands. The sidebands' existence is partially attributed to the presence of dipolar and quadrupolar interactions. These sidebands can be used to detect any interaction between a bulk active material with paramagnetic metal centers and the surface species, in our case aluminium [164].

The ^{27}Al and ^{7}Li NMR measurements are conducted on a Bruker Avance 300 spectrometer at 300 MHz (7.05 T), with a 1.9 mm probe. A MAS-rate of 30 kHz is used. The rotor and tools are cleaned and dried in vacuum overnight. The sample filling is done in an argon-filled glovebox to prevent any contamination. The 90-degree pulse as well as the chemical shift are set using saturated $Al(NO_3)_3$ in water and LiCl in water, as external reference for ^{27}Al and ^{7}Li NMR, respectively. All the spectra are acquired using a Hahn-echo pulse sequence ($t_{\pi/2} - \tau_1 - t_{\pi} - \tau 2$). This pulse sequence is used due to the large spectral widths in the MAS spectra of paramagnetic materials. Hahn-echo experiments help with phasing by refocusing magnetization in the transverse direction. The frequency gap in the spectra can typically be very wide, and without refocusing, the spectra would be extremely out of phase [165]. A pictorial representation of this sequence is shown in fig 5.2.

For the ^{27}Al NMR experiments, a $\pi/2$ pulse width of around 1.17 μs is used with recycle delays of 2 s. On the other hand, for the ^{7}Li NMR experiments, the spectra is obtained using a $\pi/2$ pulse width of around 2.5 μs with recycle delays of 12 s. The processing of the obtained spectra is done using ssSnake [166]. The obtained spectra is smoothed using a Gaussian line broadening of 1000 Hz.

All the ^{27}Al NMR experiments in this work are performed using 30 ALD NMC and LCO samples. The ^{7}Li experiments are performed with 30 ALD LCO samples. The 30 ALD cathodes were chosen in particular because of their high aluminium content, which can be seen in NMR as distinct peaks. This can be used to detect the changes in their aluminium environment.

5.3. Results and Discussion

5.3.1. SEM Microstructure of the ALD Coated Cathode Powders

In this study, the NMC and LCO powders are coated with Al_2O_3 using ALD. After coating the cathode powders using ALD, they are then scanned using SEM to examine their surface microstructure. The objective of testing the ALD coated powders with SEM is to find out if the coating is homogeneous throughout the bulk of the cathode, upon the deposition of Al_2O_3. Fig 5.3 displays the results for 10 ALD and 30 ALD powders.

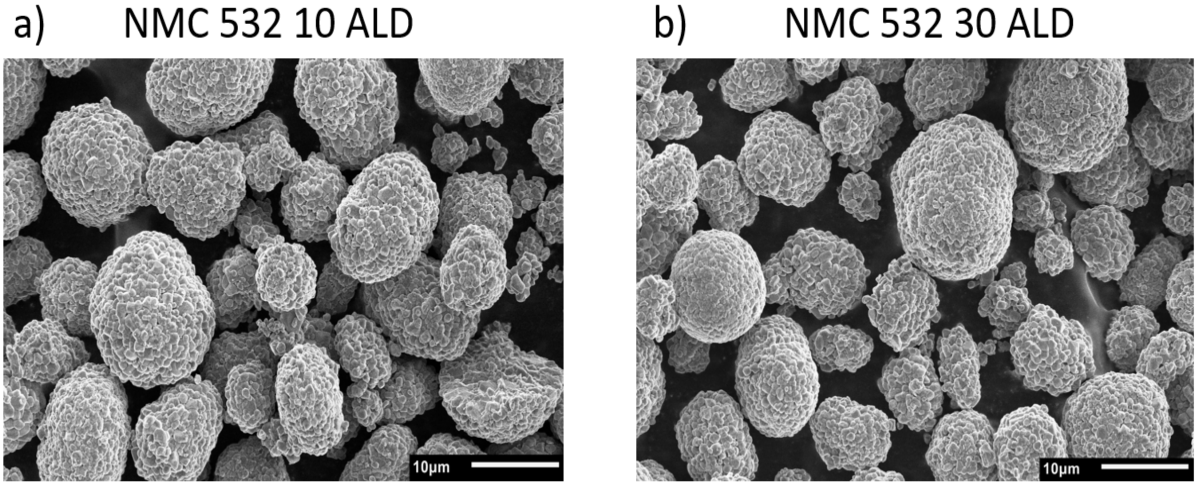

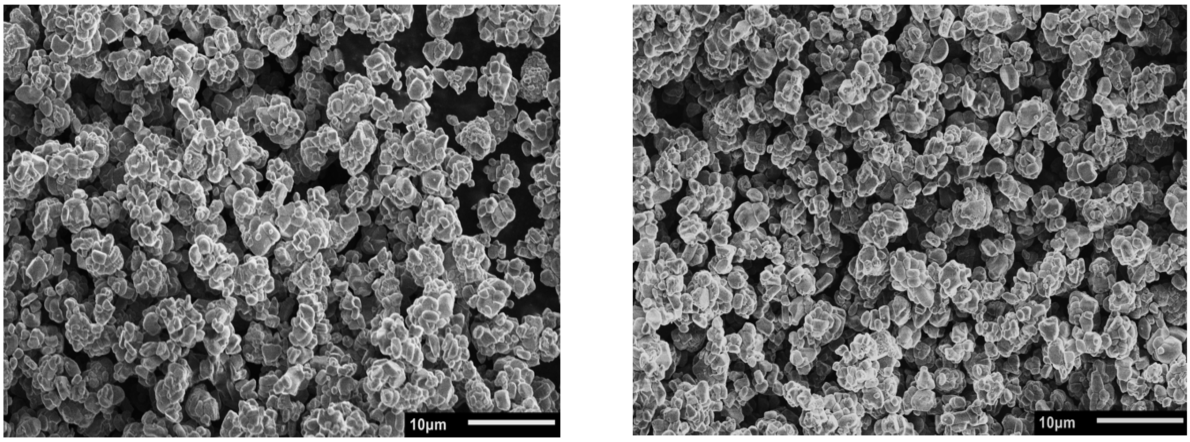

c) NMC 811 10 ALD

d) NMC 811 30 ALD

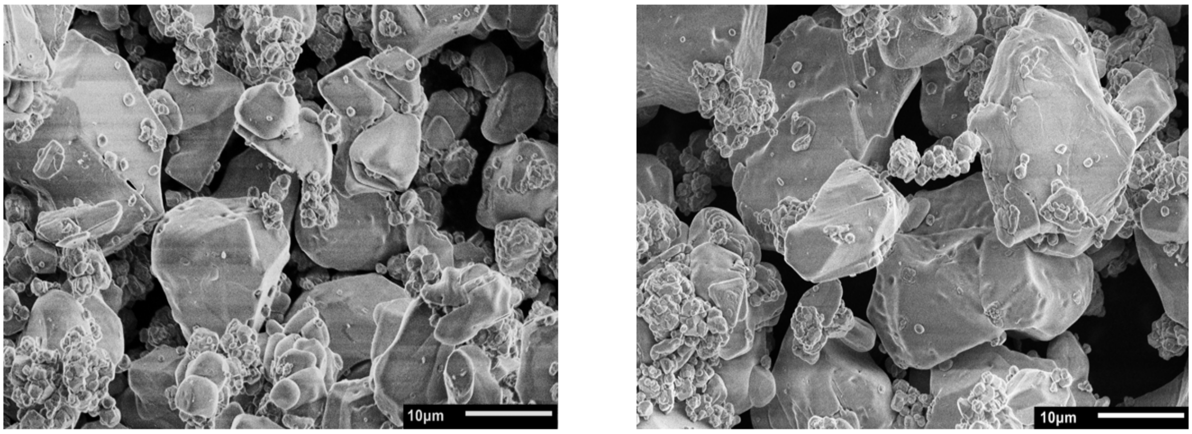

e) LCO 10 ALD

f) LCO 30 ALD

Figure 5.3: SEM micrographs of NMC 532, NMC 811 and LCO powders, 10 ALD and 30 ALD coated. The images are taken at 2000x magnification and 5 kV acceleration voltage.

From the above images, it is observed that the crystals of the cathode particles exhibit a certain amount of roughness at their edges, in comparison with uncoated cathode particles (shown in fig 4.4). This roughness indicates the presence of the Al_2O_3 layer. When the number of ALD cycles rises, a thicker Al_2O_3 layer gets formed, which increases the degree of roughness [158]. It can also be observed that the LCO particles showed distortions across their surfaces. These distortions could be the result of charging of the samples during measurement. When several electrons impinging on the sample become trapped inside the material, charging occurs, which results in a negative electrical potential [167, 168].

Overall, it can be seen that the crystal structures in the ALD coated cathode powders were homogeneous and maintained the same shape as the uncoated powders. This, indeed verifies that the thin nature of the Al_2O_3 layer helped in preserving the morphology of the particle structures after ALD [169].

5.3.2. Cycling Performance

The cycling performance of both the NMC and LCO cathodes is examined to better understand how the Al_2O_3 coating impacts the cathodes. The results are displayed in fig 5.4. The cycling results of the uncoated NMC and LCO cathodes from the previous chapter are also included in the figures for comparison with the coated cathodes. The FS cathodes and cathodes on aluminium current collector are labelled as ’FS’ and ’Al’, respectively.

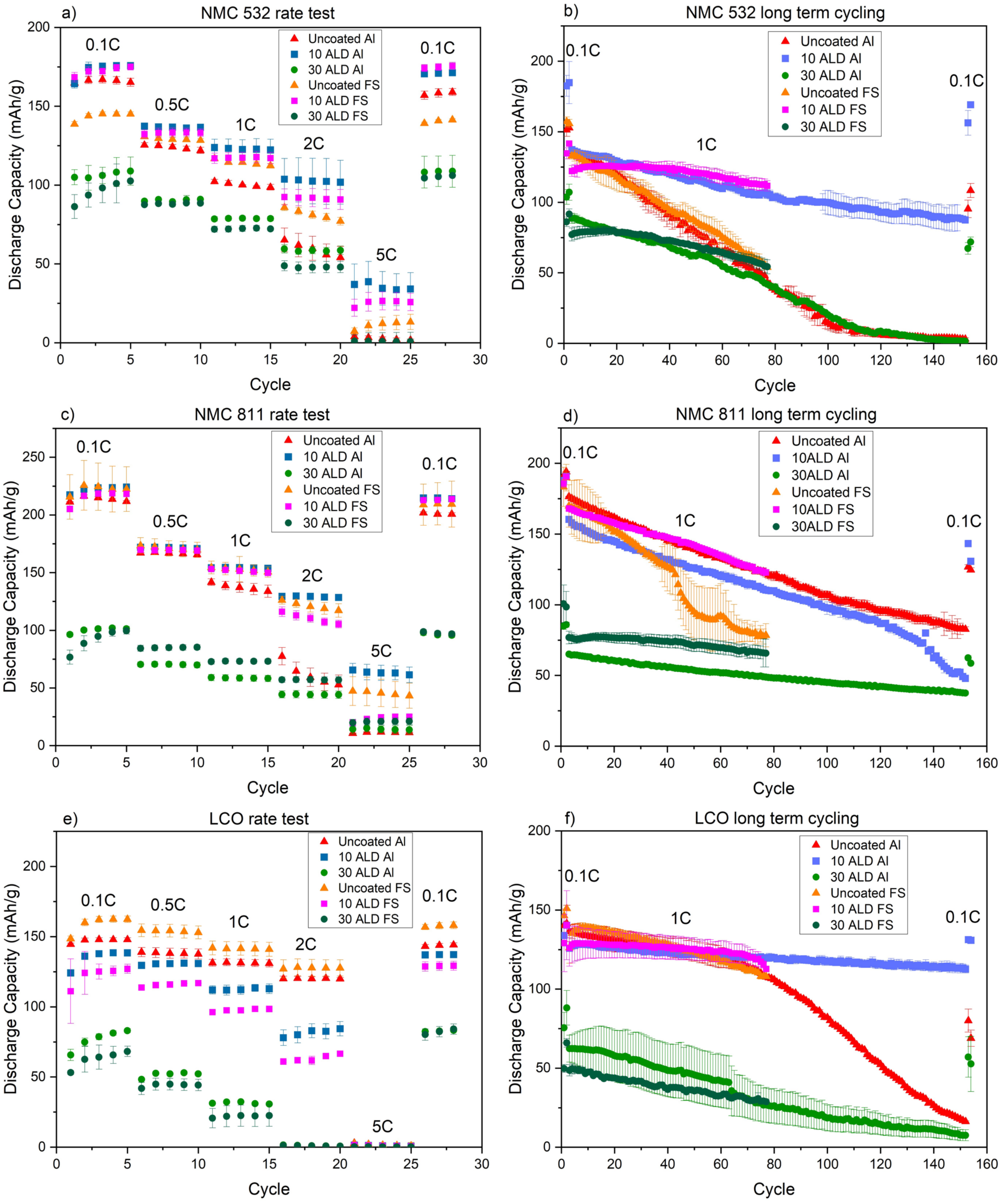

Figure 5.4: Rate test and long term cycling results for NMC 532, NMC 811 and LCO cathodes (both FS and Al)

The graphs show that both ALD coatings have an improved effect on the capacity retention and the cycling performance of the NMC and LCO cathodes. It is also obvious that the 10 ALD cathodes cycle at higher capacities than the 30 ALD cathodes. The thick ALD coating, which prevents charge transfer and limits the diffusion of lithium ions, could be to blame for the low capacities of 30 ALD cathodes

[170]. The 10 ALD cathodes cycle nearly as well as or even more efficiently than the uncoated cathodes. Therefore, it is advised to keep the coating as thin as possible to avoid any hindrance of charge transfer while cycling, in order to attain high discharge capacities.

The results of long-term cycling are an accurate representation of the performance enhancement brought on by the thin ALD coating. Specifically, in NMC 532 Al, after the 150th cycle, the discharge capacity of uncoated cathode is 3.1 mAh/g, while after coating it with 10 ALD Al_2O_3, the capacity increases to 88 mAh/g. This improved cycling performance can be correlated to a stable CEI layer and reduced electrolyte decomposition, especially at higher voltages [158]. Moreover, in the ALD coated samples, the presence of Al_2O_3 prevents trace water and oxygen from reacting with lithium inside the active material. This inhibits contaminated oxides and carbonates from forming on the cathode surface [135].

Furthermore, it is evident that the FS cathodes cycle similar to the cathodes on the aluminium current collector for the ALD coated samples, justifying the need for using them in characterization techniques. However, the NMC 532 30 ALD Al and LCO 30 ALD Al showed instances of capacity fading during long term cycling, which could be attributed to non-uniform lithium distribution in the cathodes. This, hence results in the reversible loss in capacity [171].

5.3.3. Differential Capacitance of ALD Coated Cathodes

The improvement in the cycling performance for the ALD coated cathodes is analysed further in terms of differential capacity as shown in fig 5.5. The dQ/dV curves are calculated using the charge-discharge curves during long term cycling, and help to determine the degree of voltage stability of these cathodes during cycling.

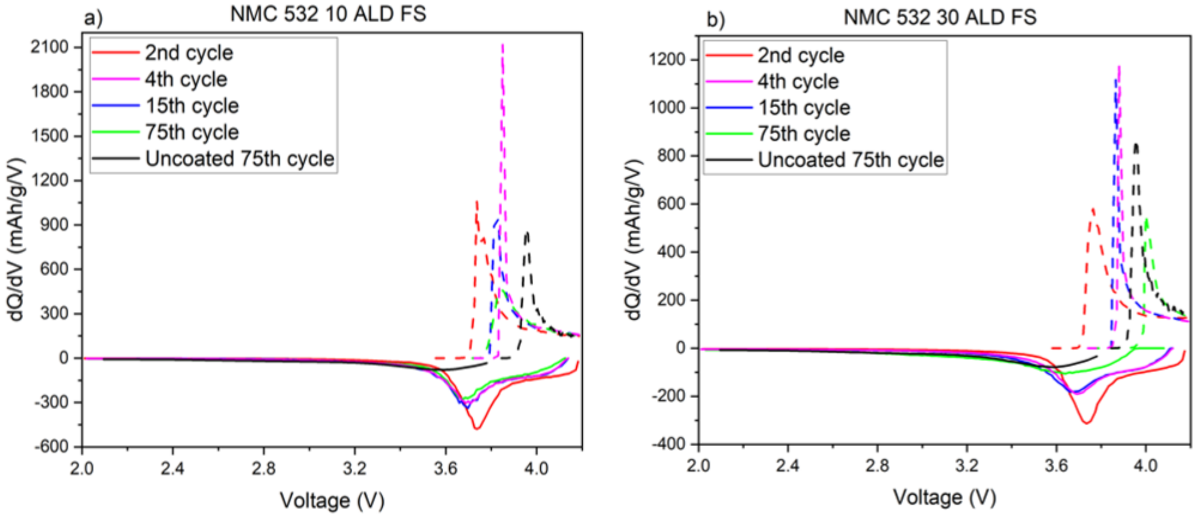

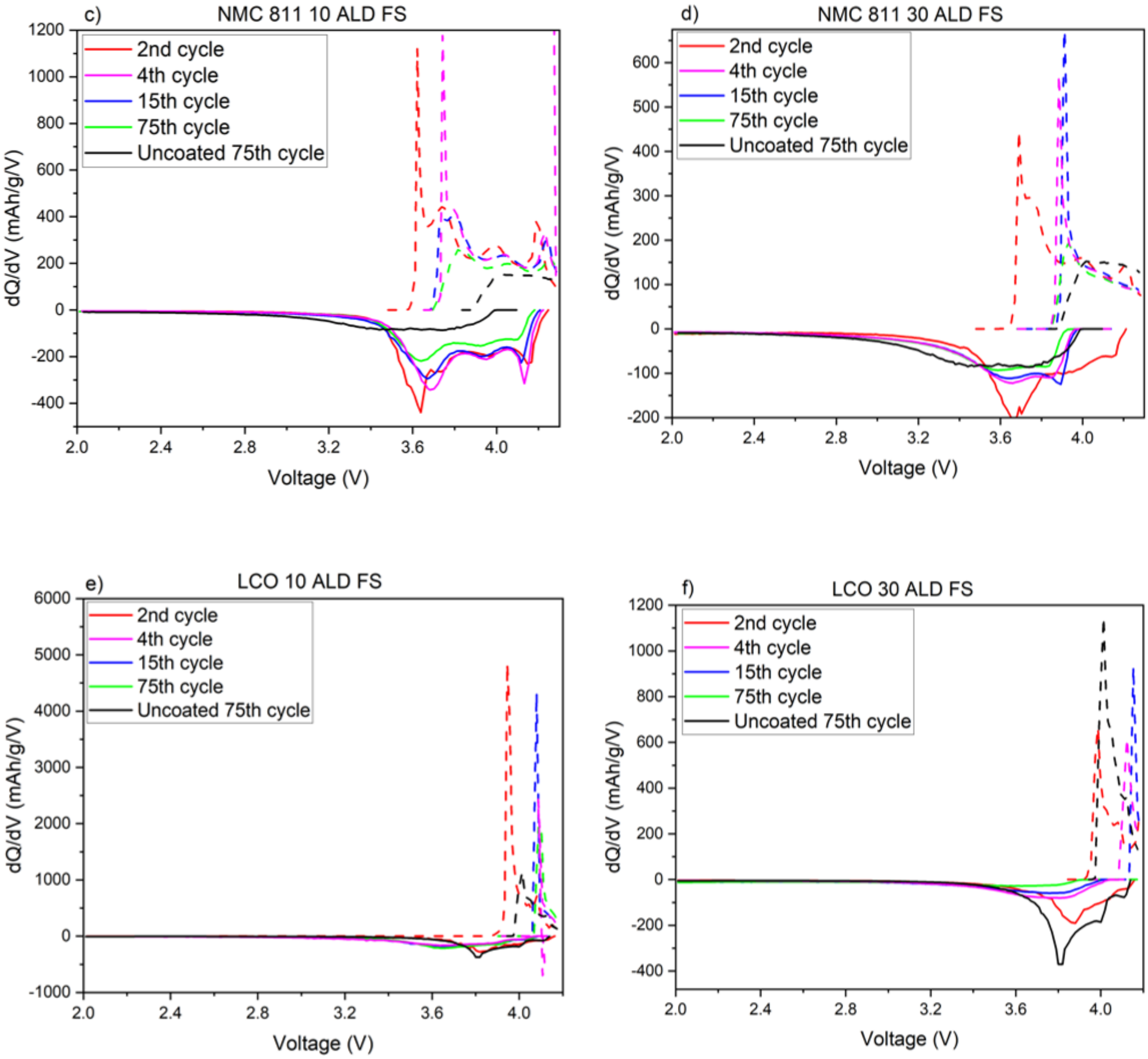

Figure 5.5: dQ/dV curves of FS NMC 532, NMC 811 and LCO cathodes (10 ALD and 30 ALD) after 2nd, 15th and 75th cycle*. For the respective cathodes, the dQ/dV curve of uncoated cathodes after 75 cycles is also added in the curve.
* 2nd cycle is at 0.1 C rate, while 4th, 15th and 75th cycles are at 1 C rates.

The graphs above show the oxidation and reduction peaks of the ALD coated cathodes as a function of their charge-discharge cycles. The graphs also contain the dQ/dV curve of the uncoated cathodes after 75 cycles, for the respective ALD coated cathode materials. This is added for comparison with the ALD coated cathodes. In the dQ/dV curve, the initial shift in the peak from 2nd cycle to the 4th cycle is attributed to the increase in the C rate from 0.1 C to 1 C during cycling. For the majority of ALD coated cathodes tested in this work, the oxidation and reduction peaks after the 4th, 15th and 75th cycles are significantly more stable than the uncoated cathodes (shown in fig 4.6). Furthermore, the ALD coated cathodes showed a substantially lower discharge voltage drop throughout cycling, in comparison to uncoated cathodes. This demonstrates the structural robustness of the coating layer and its ability to prevent electrolyte decomposition [169].

In NMC 811, we notice that the second redox peak begins to form at higher voltages in the 10 ALD sample, indicating a phase transition, similar as observed in the uncoated samples. This peak indicates the occurrence of a reaction other than the intercalation reactions within the cell [172]. The

30 ALD sample did not, however, produce a second peak at high voltages, indicating that the thicker ALD coating prevented the phase transition from happening and, as a result, prevented the formation of microcracks on its surface. On the other hand, for the NMC 532 30 ALD cathode, it can be seen that its oxidation peak shifts with cycling, although the reduction peak only marginally shifts. The shift in the oxidation peak may indicate reversible incorporation of Li_2O into the CEI, during delithiation [173].

5.3.4. Investigating the Impedance of ALD Coated Cathodes

In the previous subsection, it was observed that the peak shift associated with oxidation and reduction decreased in the ALD coated samples, in comparison to the uncoated samples during cycling. This decrease in the peak shift could imply a decrease in the cell resistance. To prove this, we conduct EIS measurements on the ALD coated FS cathodes. The results are shown in fig 5.6. The obtained spectra were fitted with the equivalent circuits, shown in fig 5.7.

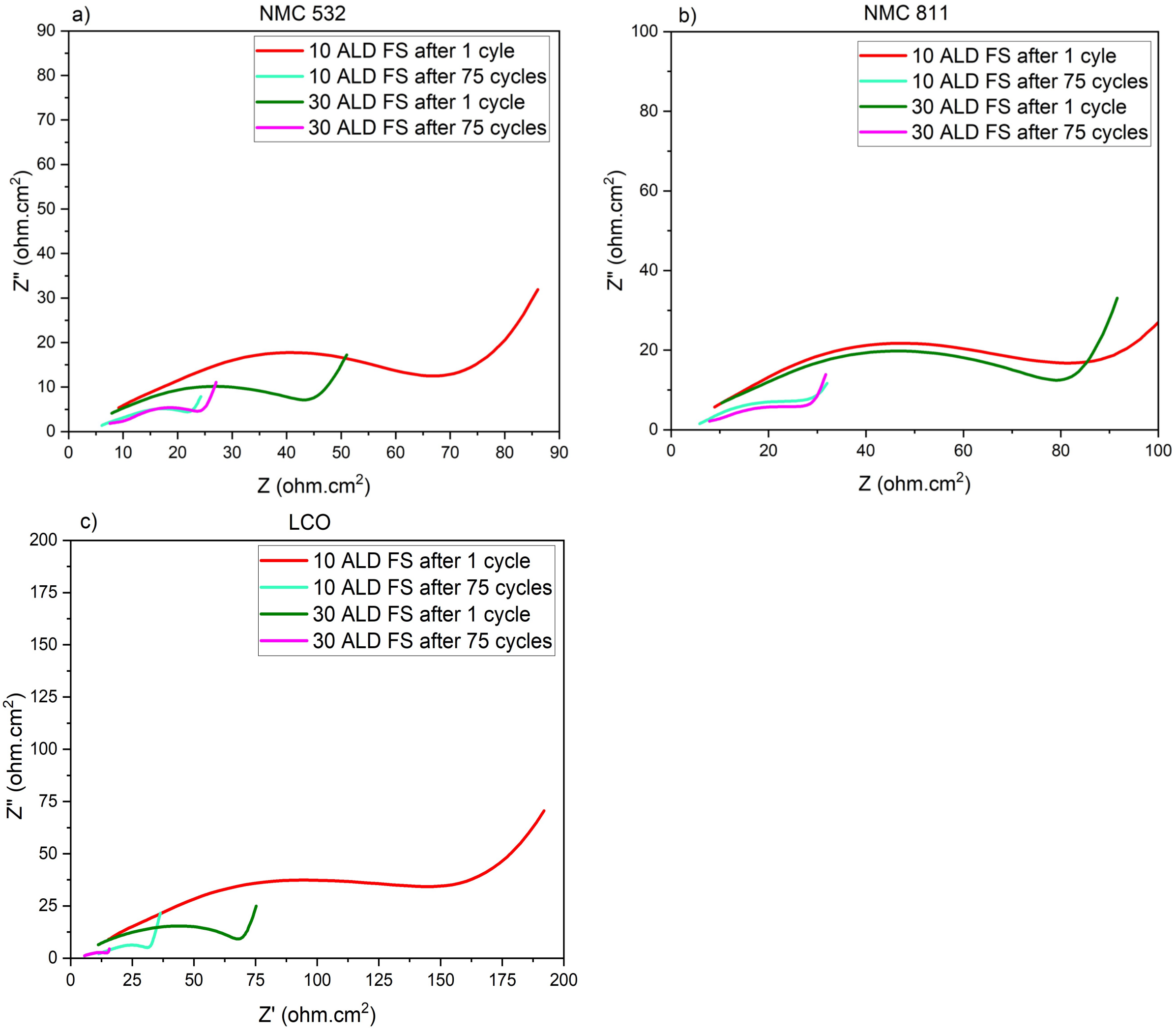

Figure 5.6: EIS spectra of FS NMC 532, NMC 811 and LCO ALD coated cathodes, *after the 1st and the 75th cycle.
* 1st cycle is at 0.1 C rate, while the 75th cycle is at 1 C rate.

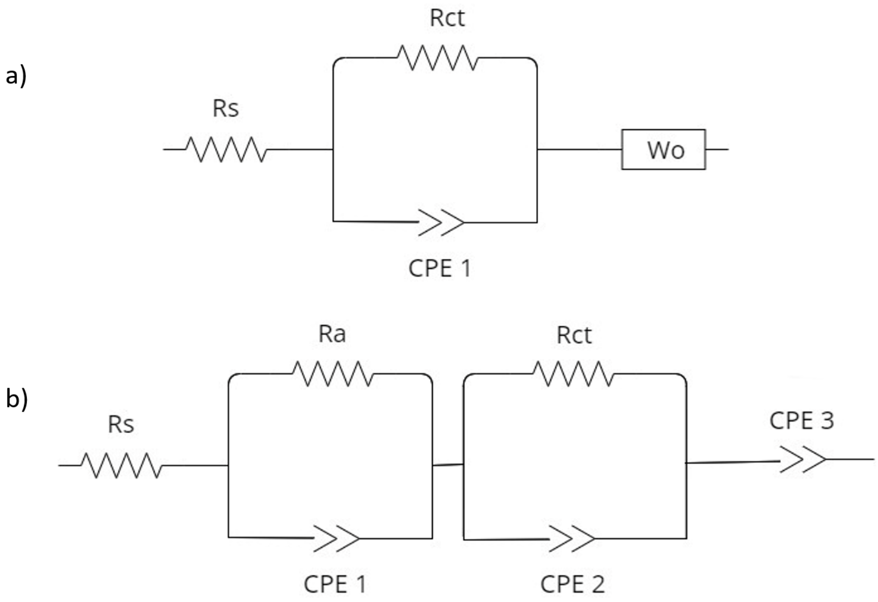

Figure 5.7: Equivalent circuit model for the impedance spectra after a) 1st cycle and b) 75th cycle.

The plot after 1 cycle consists of three regions. The intersection of the semicircle with the x-axis at high frequency region is attributable to the electrolyte resistance, as well as the resistance of the cell and wires (R_s). The charge transfer resistance is represented by a semicircle in the mid frequency region (R_{ct}), while the lithium ion diffusion is represented by the sloping line in the low frequency region (W_o). The Nyquist plot reveals the emergence of an extra semicircle after 75 cycles, which is caused due to the formation of the CEI layer. The resistance of this layer is denoted as R_a in the circuit. Each semi-circle in the Nyquist plot represents an R-P element in the equivalent circuit.

As can be seen in fig 5.6, the resistance decreases noticeably throughout cycling, which indicates a reduction in the charge transfer resistance. The significant decrease in the semicircle associated with the charge transfer resistance over cycling, could also be due to the formation of lithium dendrites on the anode [131, 132]. The circuit for the spectra follows the same model as obtained for the uncoated cathodes. After 1 cycle, the circuit contains a single R-P element, while after 75 cycles, another R-P element is added, owing to the formation of the CEI layer. The resistances after 75 cycles are calculated from the circuit model and are compared against those obtained from uncoated samples, tested in the previous chapter.

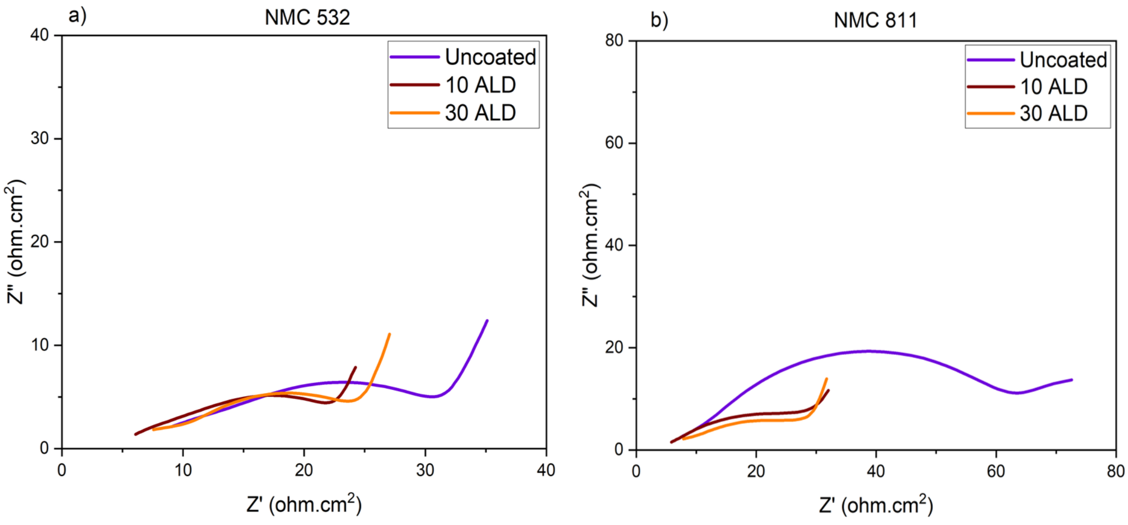

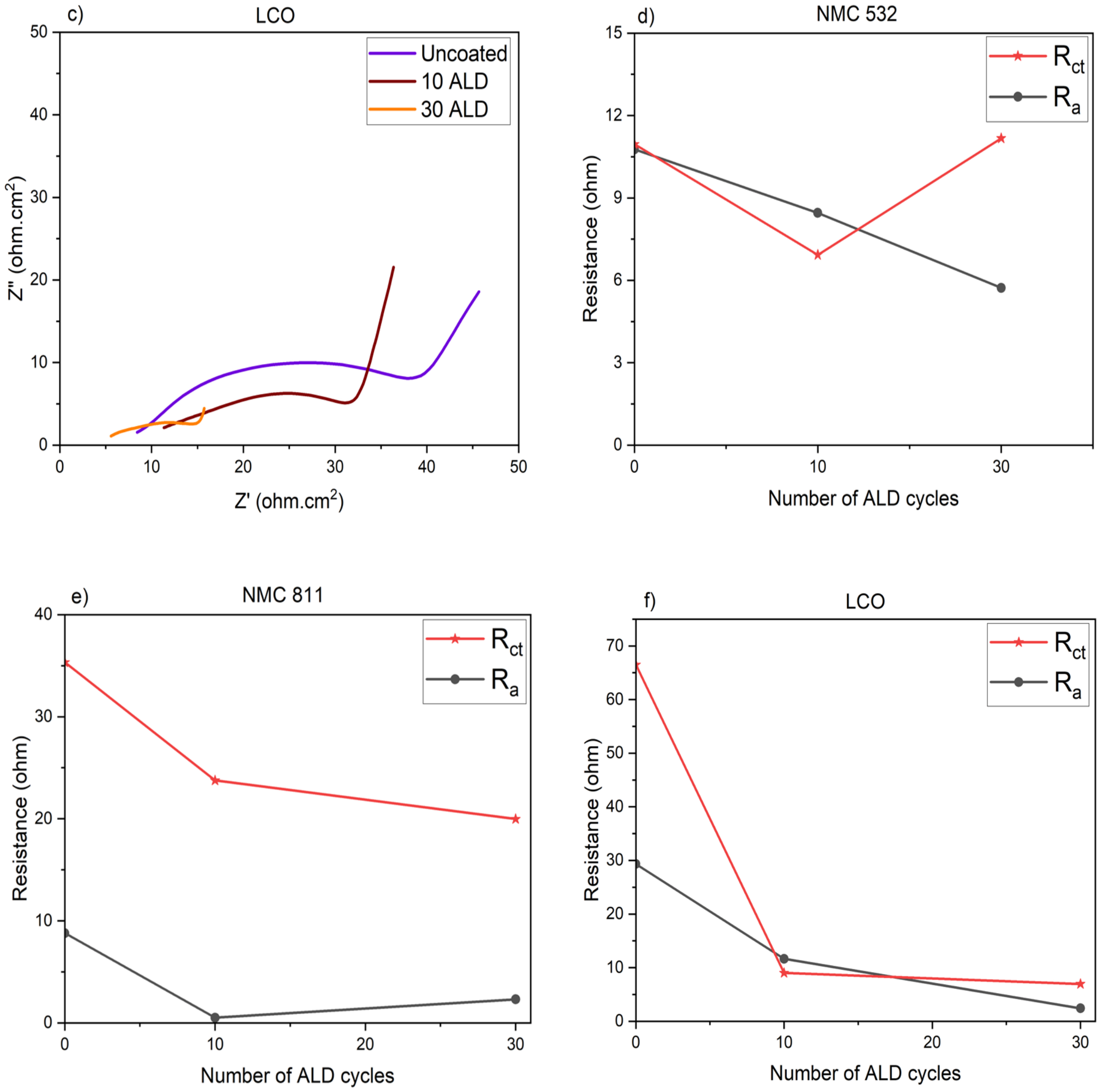

Figure 5.8: EIS spectra after 75 cycles for NMC 532, NMC 811 and LCO cathodes ((a), (b) and (c)). The resistances R_{ct} and R_a are plotted as a function of ALD cycles for the above cathodes after 75 cycles ((d), (e) and (f)).

The plot containing R_{ct} and R_a for uncoated, 10 ALD and 30 ALD cathodes are shown in fig 5.8. This figure also includes a comparison of the impedance spectra for uncoated cathodes, along with 10 ALD and 30 ALD cathodes after 75 cycles. From fig 5.8, we can verify that, after long term cycling, there is a significant decrease in the impedance observed for the ALD coated samples compared to the uncoated samples. This decrease thereby led to lesser charge transfer resistances for the ALD coated samples. This proves that the deposition of Al_2O_3 helped produce a superior cathode surface, which facilitates faster lithium diffusion. Furthermore, the bulk ionic conduction in the NMC and LCO cathodes is enhanced by the deposition of Al_2O_3, which helps prevent undesirable reactions with the electrolyte during cycling [174].

With an increase in ALD coating thickness, both the charge transfer resistance and the CEI layer resistances drop. The NMC 532 30 ALD cathode did, however, experience a higher charge transfer resistance, which could be a result of its thick coating layer, causing a hindrance in the diffusion of lithium ions. This can be correlated to the peak shift observed in dQ/dV analysis, discussed in the previous subsection.

For the uncoated NMCs, intergranular cracking as a result of continuous electrolyte decomposition, causes reduced electrical contact and accumulation of CEI layers, resulting in high impedance. The presence of Al_2O_3 acts as an HF scavenger and prevents this decomposition, contributing to a low cell impedance. This coating also aids in preventing the leaching of transition metals, which in turn prevents surface reconstruction [175, 176]. However, for some of the 30 ALD cathodes, we notice a higher impedance. This could be because of the thick coating that prevents lithium ion conduction, as a result causing the resistance to increase. This phenomenon can be verified from their cycling behaviour and from the dQ/dV curves [133].

5.3.5. Examining the Cathode Microstructure using SEM-EDS

The results from the electrochemical cycling and EIS indicated that the Al_2O_3 coating induces a stable CEI layer, helping to prevent electrolyte decomposition and capacity fading. The ALD coated cathodes, after long term cycling are subjected to SEM analysis, to study their surface morphology and structure. The results for the 10 ALD and 30 ALD FS cathodes are shown in fig 5.9.

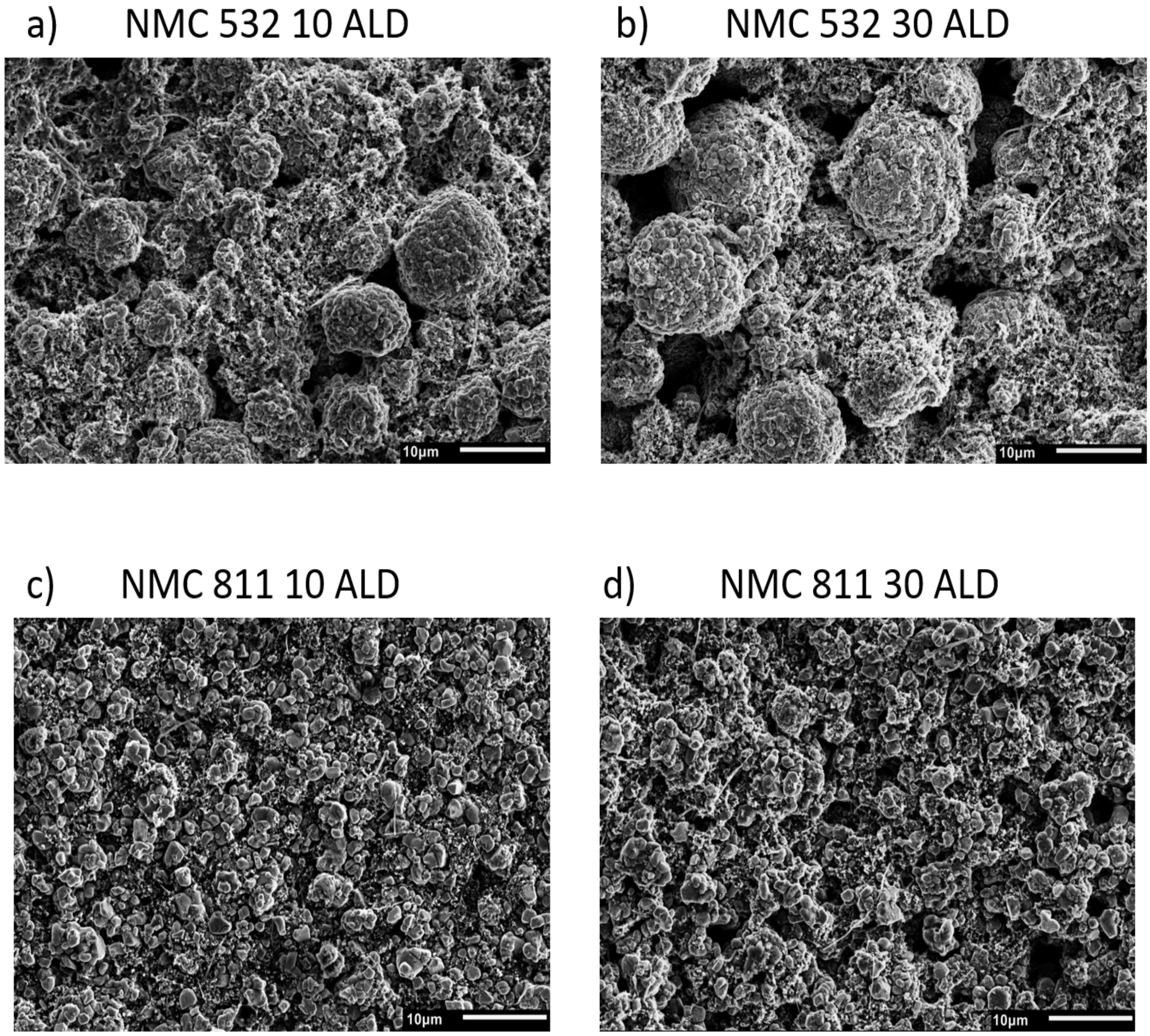

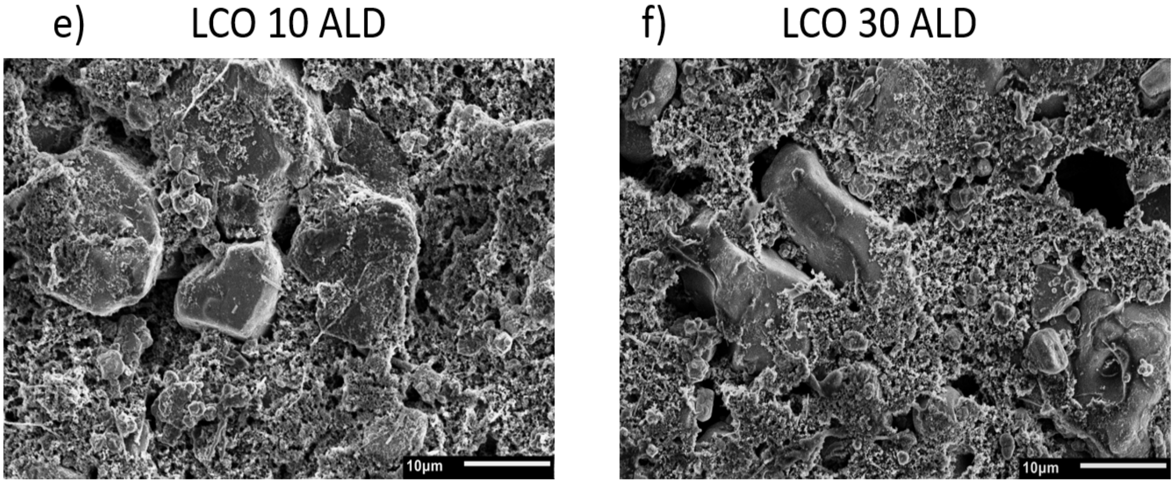

Figure 5.9: SEM micrographs of 10 ALD and 30 ALD coated NMC 532, NMC 811 and LCO FS cathodes after 75 cycles. The images are taken at 2000x magnification and 5 kV acceleration voltage.

The above images show that after long term cycling, there are no surface cracks observed on the ALD coated cathodes. This can be attributed to the stability and robustness of the Al_2O_3 layer, which aids the electrode in recovering its original structure from volume expansions during cycling and preserve the electrode network, which was absent in the uncoated cathodes [177]. The absence of cracks on the surface of the NMC 532 30 ALD FS cathode, indicates that the structural instability of the cathode, which could have been a result of a high charge transfer resistance observed in the previous subsection, was not detectable in SEM.

In order to ascertain how the elemental composition, specifically the concentration of aluminium, changes over cycling in the ALD coated cathodes, EDS analysis was performed. The results from this analysis are shown in B.5. The results show that with an increasing ALD coating thickness, the composition of aluminium increases in the cathodes. The presence of aluminium in the EDS spectrum after long term cycling, indicates that the Al_2O_3 layer remains present in the cathodes. However, for the other elements, EDS was inconclusive to ascertain their changes in composition upon cycling.

The SEM images of the ALD coated cathodes on aluminium current collectors, which were likewise subjected to long-term cycling, are shown in B.6. The results were in line with those attained using FS cathodes. This indicates that the ALD coating had a major impact on the cathodes' ability to maintain a stable surface during cycling, which improved their overall performance.

5.3.6. XRD Results

The XRD measurements were initially performed on the ALD coated powders to detect the presence of impurities after ALD coating. Shown below is a representation of the data obtained from the measurement of NMC 532 powder sample. The NMC 811 and LCO powder samples showed a similar peak pattern, which are depicted in fig B.8. For an accurate comparison, the diffraction pattern of the uncoated powder sample, obtained from the previous chapter, is also included to the plot.

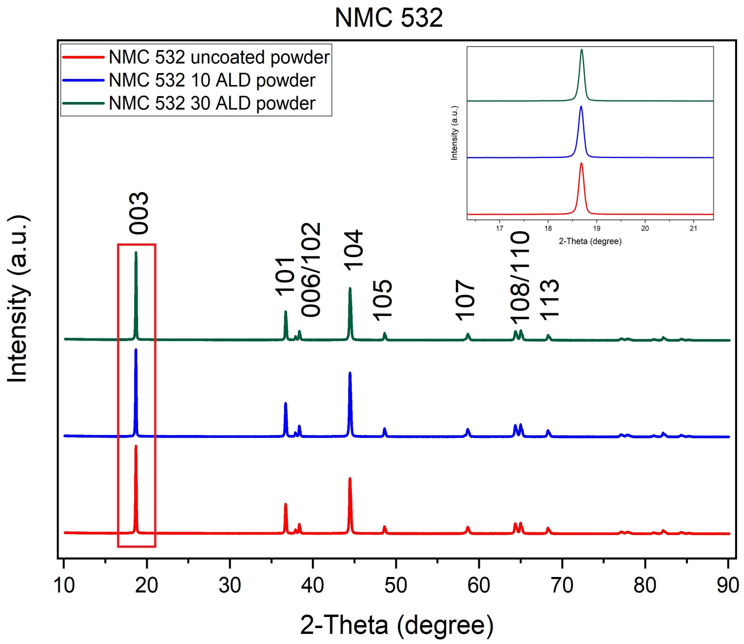

Figure 5.10: Diffraction patterns of *NMC 532 uncoated, 10 ALD and 30 ALD powder samples. The pattern on the top right is the zoomed image of the highlighted region in the main pattern.
* The measurement for NMC 532 was performed using a monochromator for 15 hrs, while measurements for NMC 811 and LCO were performed using an anti-scatter slit for 2 hrs. An open sample holder was used for the measurements.

It is clear from the plot that the powder sample had no evidence of any additional peaks, following the ALD coating. Additionally, it can be seen that the peaks are in line with one another and do not shift after ALD treatment. This shows that following the application of the ALD coating, the powder's structure and crystallinity did not alter [138, 36]. Due to the splitting of the 006/112 and 108/110 peaks, the patterns suggest that the ALD coated cathodes have an ordered hexagonal layered structure [127]. Additionally, the absence of an Al_2O_3 peak in the ALD coated samples illustrates that the coating is thin and amorphous. From the previous subsections, it was learned that the Al_2O_3 coating layer added structural stability to the NMC and LCO cathodes, which inhibited the formation of cracks during cycling. The ALD coated cathodes are subjected to XRD in order to assess their structural stability throughout electrochemical cycling. The results are show in fig 5.11.

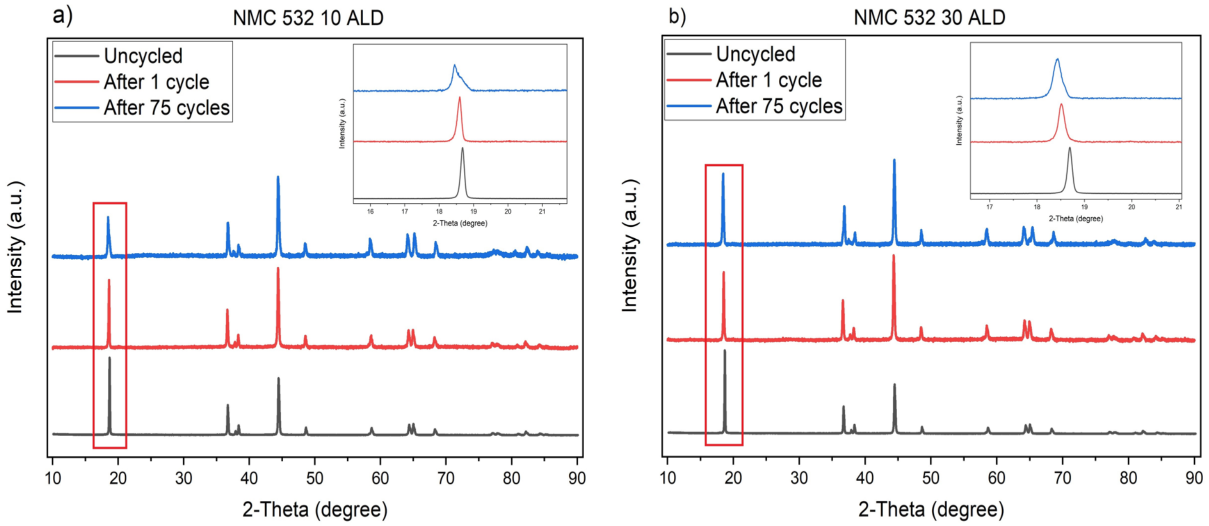

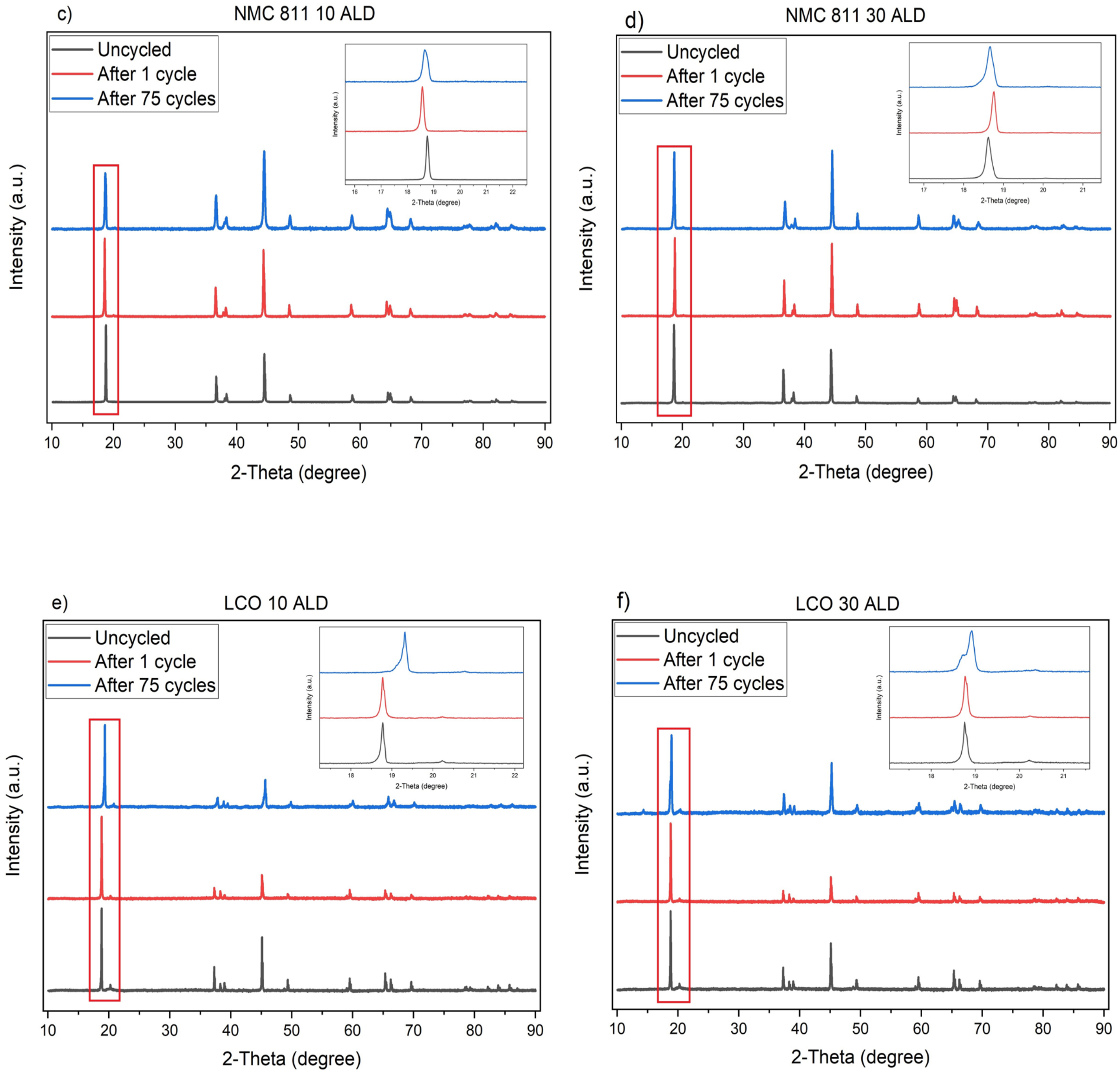

Figure 5.11: XRD patterns of *FS ALD coated NMC 532, NMC 811 and LCO cathodes before cycling, **after 1 cycle and after 75 cycles.
* All the uncycled NMC 532 and NMC 811 cathodes were measured with a monochromator for 15 hrs in an open sample holder. The LCO cathodes after 75 cycles were measured with an anti-scatter slit using an air-tight sample holder. The remaining cathodes were measured with an anti-scatter slit using an open sample holder.
** 1st cycle is at 0.1 C rate, while the 75th cycle is at 1 C rate.

It is clear from the plots that the ALD coated cathodes show a peak shift, particularly after 75 cycles. The shift could have been due to lattice parameter expansion, displacement error or strain on the sample. To investigate the contributing factors for this peak shift, Rietveld refinement is performed. The refinement results for NMC 532 10 ALD FS cathode after 75 cycles is shown in fig 5.12a, where R_w is the weighted profile parameter. The refinement results for the remaining samples are shown in B.9.

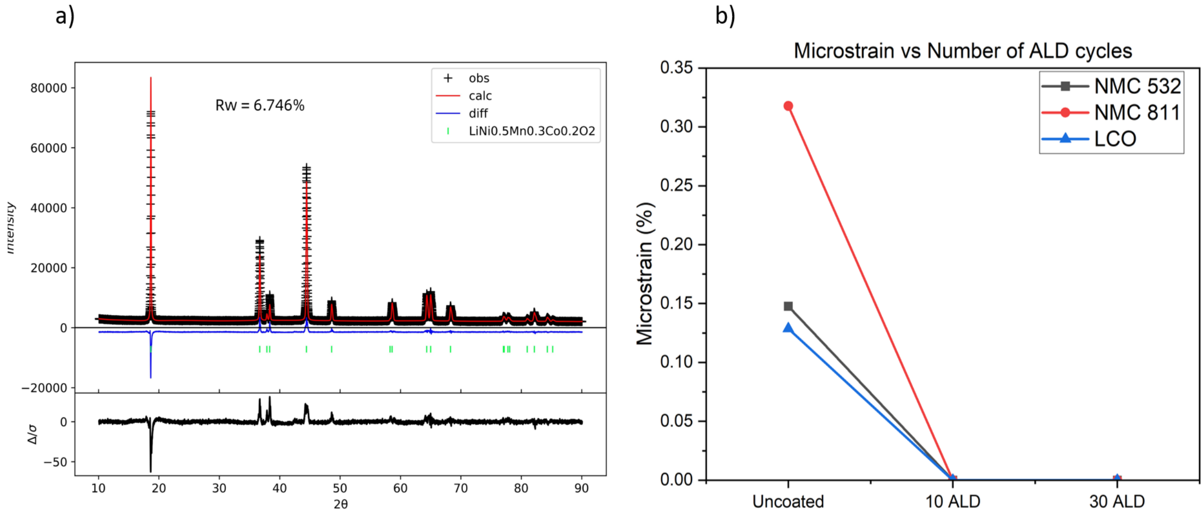

Figure 5.12: a) Rietveld refinement result for NMC 532 10 ALD FS cathode after 75 cycles. b) Microstrain values for uncoated and ALD coated cathodes after 75 cycles.

From the refinement, the cause of the peak shifts seen in fig 5.11, seemed to be due to displacement error. This error arises due to the changes in the height of the samples used for measurement. There was no presence of microstrain observed after the refinement of the ALD coated cathodes after 75 cycles, as seen in fig 5.12b. Additionally, similar to the uncoated cathodes, the spinel structure of the ALD coated cathodes remain unchanged after cycling. This implies that the ALD coated cathodes' original structure was preserved, with no discernible significant phase transformations.

5.3.7. Surface Analysis using XPS

The ALD coated powder samples were tested with XPS to evaluate the stoichiometry of the surface elements present in the samples. Investigated scans include Al 2p, C 1s, O 1s, and Li 1s. The scans for transition metals contained high background, and are hence added in B.7. Fig 5.13 and fig 5.14 show the XPS results of the 10 ALD and 30 ALD cathode powders, respectively.

The Al 2p scan clearly reveals the presence of a peak at 74 eV, which corresponds to the Al_2O_3 coating on the samples. Due to the greater thickness of the Al_2O_3 layer, the 30 ALD samples have an even more definite, obvious peak than the 10 ALD samples. This scan also has a peak at 67.8 eV, attributed to the Ni 3p satellite and Co 3p satellite in NMC and LCO powders, respectively.

The C 1s scan consists of four peaks at 284.8 eV, 286.3 eV, 288.3 eV and 289.6 eV. The peak at 284.8 eV is due to adventitious carbon while the peak at 286.3 eV is caused by the C-O bonds in the carbon layer or due to the presence of carbonate species on the powder surface. The peaks at 288.3 eV and 289.6 eV are caused by the presence of Li_2CO_3 residue. This is a product formed by the reaction of the Li_2O present on the powder surface, with moisture. On comparing the peaks for the ALD coated powders with the uncoated powders (see fig 4.14), it was found that the ALD coated samples show reduced peaks for Li_2CO_3. This shows that the Li_2CO_3 residue was greatly reduced from the powder's surface, thanks to the presence of Al_2O_3. When powders are coated using ALD, the precursor TMA combines with the -OH and $-CO_3{}^{2-}$ groups on the surface of the powder particles. This creates a layer of Al_2O_3 that can remove any undesirable residues from the surface. As a result, the sample's surface develops a favourable $LiAlO_2$ layer. This hence reduces the negative surface interaction, which otherwise could could slow the cycling process and cause an increase in impedance [178].

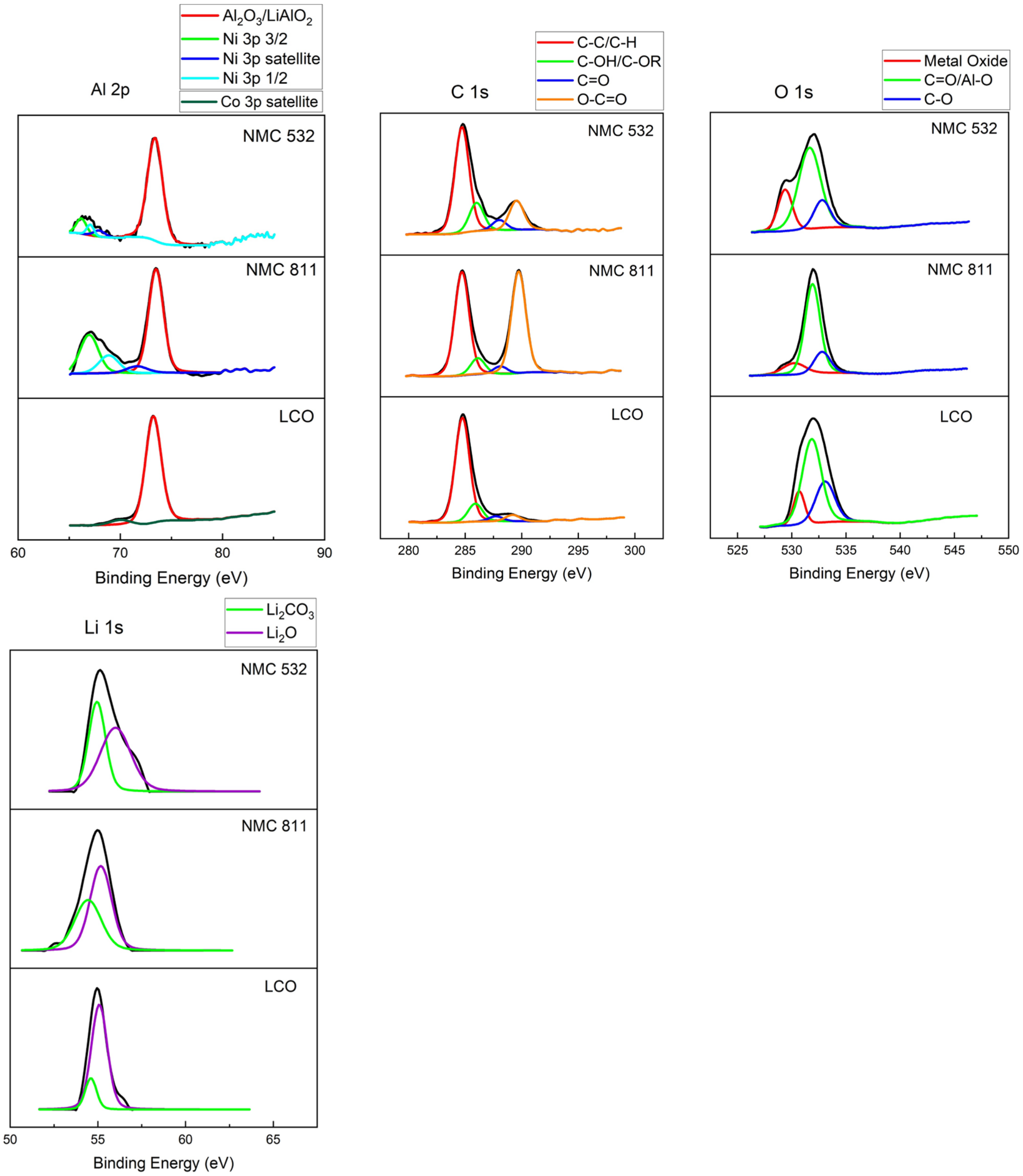

Figure 5.13: Fitted photoelectron spectra of (from left to right, top and bottom row) Al 2p, C 1s, O 1s and Li 1s for NMC 532, NMC 811 and LCO 10 ALD powder samples

The O 1s scan for both the ALD coated powders show a distinct peak attributed to C=O. This peak could indicate a possible Li_2CO_3 residue on the surface of the sample. Additionally, this peak also contains contribution from the Al-O bond of the Al_2O_3 layer. A large contribution to the C=O peak is brought about by the high bond energy of Al-O (511 kJ/mol) [179, 180]. The Li 1s scan reveals that the peak for Li_2CO_3 is lower in ALD coated powders than it is in uncoated powders, demonstrating the efficiency of the ALD coating layer in minimizing residuals from accumulating on the surface.
]

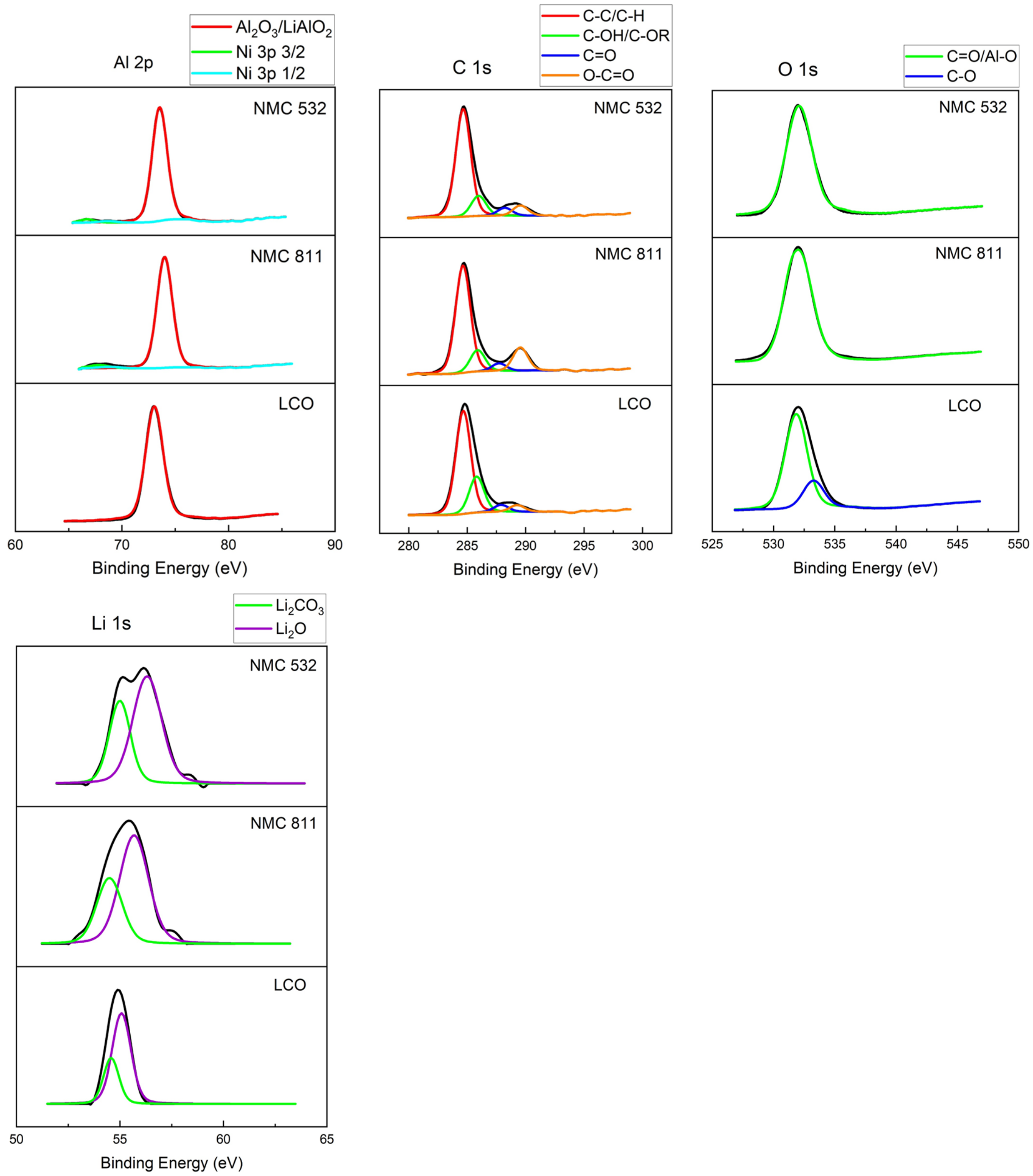

Figure 5.14: Fitted photoelectron spectra of (from left to right, top and bottom row) Al 2p, C 1s, O 1s and Li 1s for NMC 532, NMC 811 and LCO 30 ALD powder samples

According to scans of transition metal elements (see B.7), Ni is typically found in the +2 and +3 valence states in NMCs, whereas Mn and Co are found in +4 and +3 states, respectively. On the other hand, in LCO, Co exists predominantly in both +3 and +4 valence states [105]. The cathodes made from these powders are examined using XPS, to determine the degree to which the composition of their surface elements has changed, before and after cycling. The results are depicted below, according to each elemental scan.

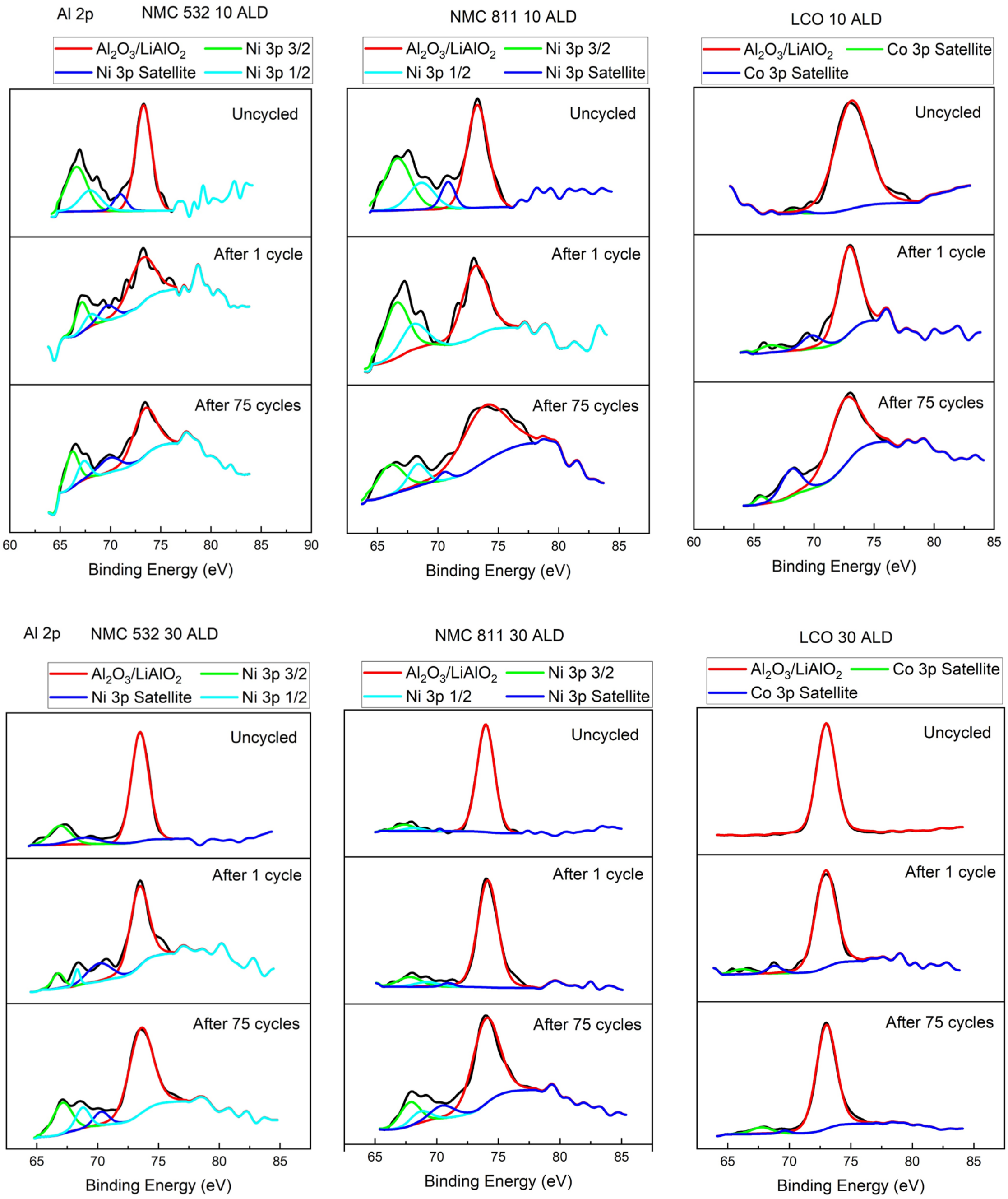

Figure 5.15: Fitted Al 2p spectra of (from top to bottom row) 10 ALD and 30 ALD, (from left to right) NMC 532, NMC 811 and LCO FS cathode samples. The cathode samples are tested before cycling, after 1 cycle and after 75 cycles.

The ALD coated cathodes show a clear peak for Al 2p, confirming the presence of Al_2O_3 or $LiAlO_2$ from the ALD coating. With a thicker ALD coating (30 ALD), the peak observed is more pronounced. The presence of this peak in the cathodes after 75 cycles indicates that the Al_2O_3 layer remains intact over cycling.

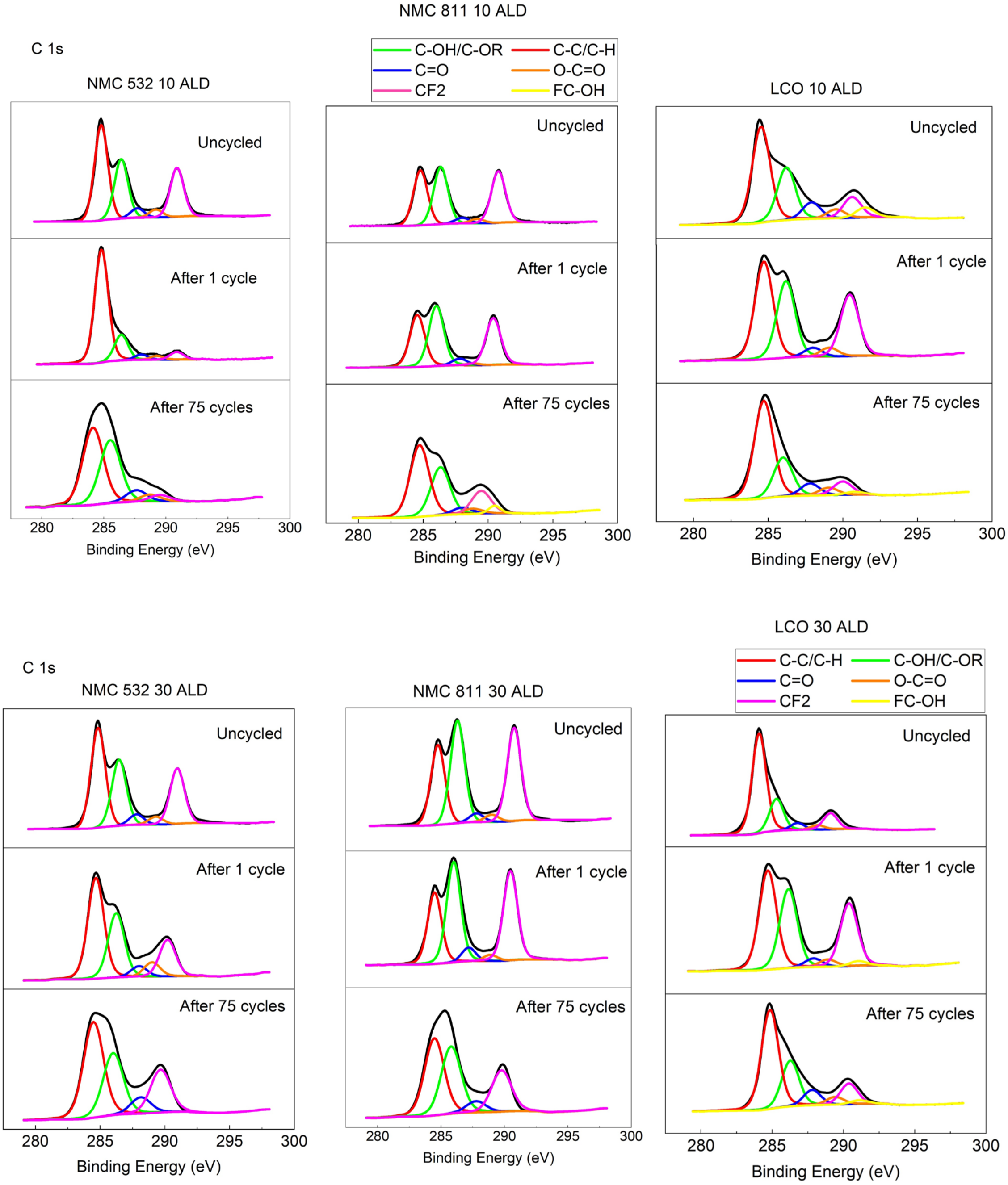

Figure 5.16: Fitted C 1s spectra of (from top to bottom row) 10 ALD and 30 ALD, (from left to right) NMC 532, NMC 811 and LCO FS cathode samples. The cathode samples are tested before cycling, after 1 cycle and after 75 cycles.

During cycling, the decomposition of the electrolyte results in the formation of $ROCO_2Li$, Li_2CO_3 and $LiPF_xO_y$ products on the cathode surface [133]. The C=O, O=C-O, Li-F and O-F peaks in the elemental scans serve as a sign for this. After cycling, it can be observed that the C=O and O=C-O peaks are less prominent than they were on the uncoated cathode. This shows that in the ALD coated cathodes, the contaminants Li_2CO_3 and $ROCO_2Li$ are not the dominanting ones in the CEI film.

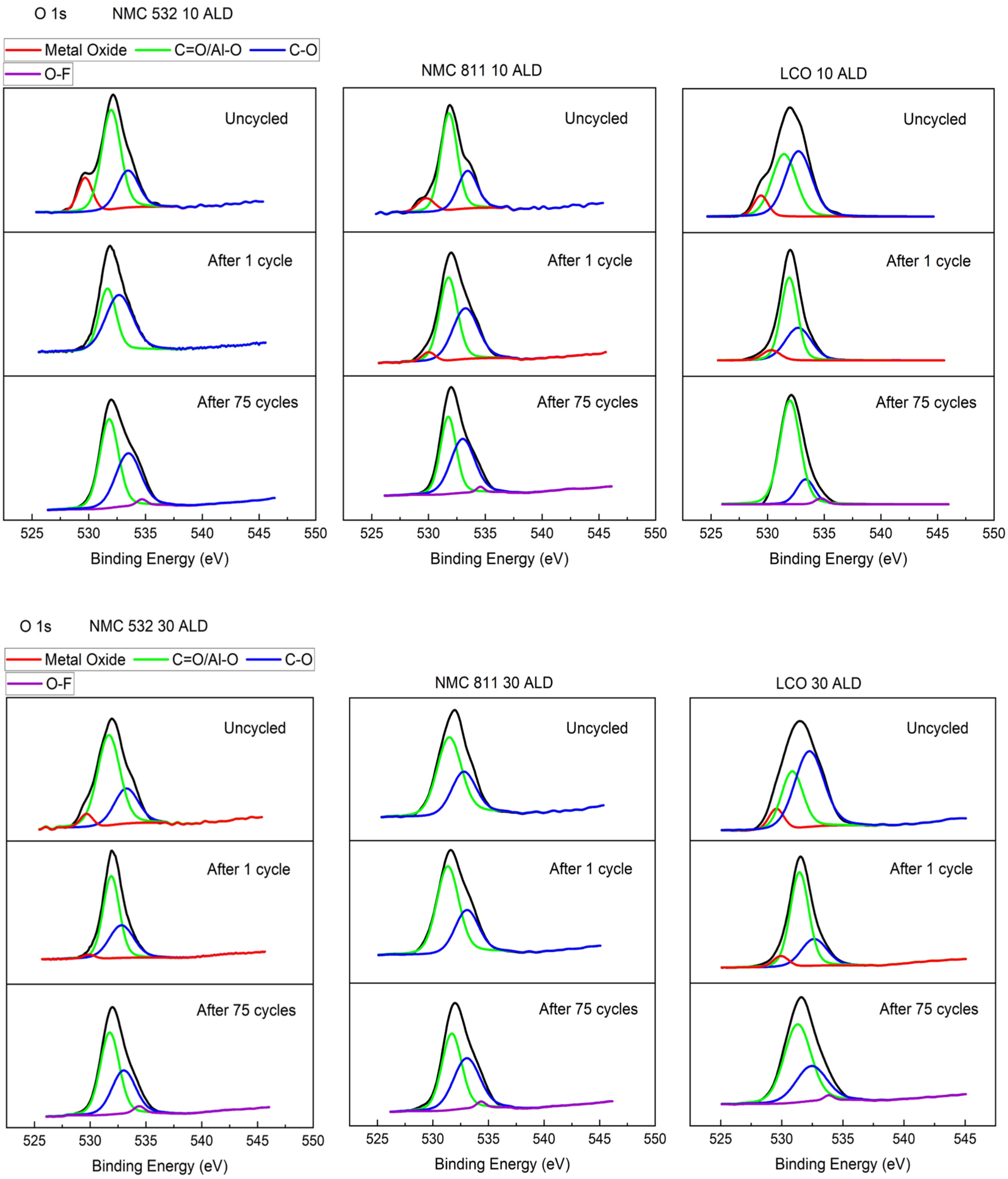

Figure 5.17: Fitted O 1s spectra of (from top to bottom row) 10 ALD and 30 ALD, (from left to right) NMC 532, NMC 811 and LCO FS cathode samples. The cathode samples are tested before cycling, after 1 cycle and after 75 cycles.

The O 1s scan contains an O-F peak at 534.8 eV, associated with the formation of $LiPF_xO_y$ as a result of electrolyte salt decomposition. This peak is less intense, in comparison to the peak observed for uncoated cathodes after cycling (fig 4.16), which could imply a decrease in the decomposition of electrolyte salt upon coating the cathodes with Al_2O_3. The oxygen atoms in the NMC and LCO crystal lattice are responsible for the metal oxide peak at 529.5 eV. There were no detectable peaks for metal oxide after cycling due to the existence of a CEI layer on the cathode surface [181].

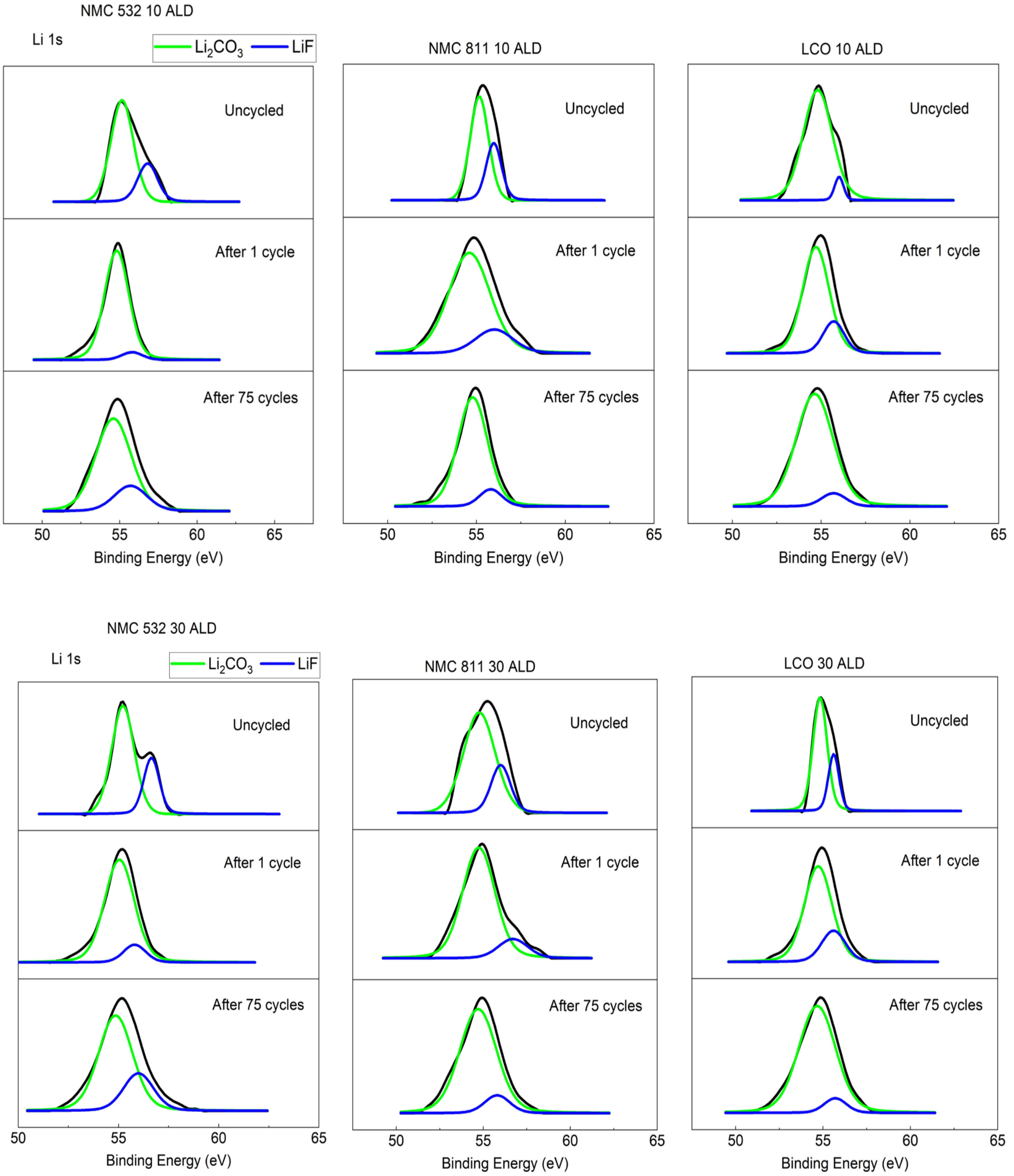

Figure 5.18: Fitted Li 1s spectra of (from top to bottom row) 10 ALD and 30 ALD, (from left to right) NMC 532, NMC 811 and LCO FS cathode samples. The cathode samples are tested before cycling, after 1 cycle and after 75 cycles.

The LiF peak in the Li 1s scan can also be used to detect the formation of $LiPF_xO_y$ contaminant. Its decreased peak intensity indicates that the ALD coating was successful in alleviating electrolyte decomposition. Another explanation for a decrease in peak intensity is that the cathode samples were washed before being measured with DMC, which could have washed away the surface LiF [182, 183]. In the uncycled cathodes, the LiF peak could be from the electrode fabrication, which facilitates a reaction between PVDF and Li_2CO_3/LiOH present on the cathode surface. A notable peak for Li_2CO_3 can be observed in the Li 1s scan, which may help improve interface stability [133].

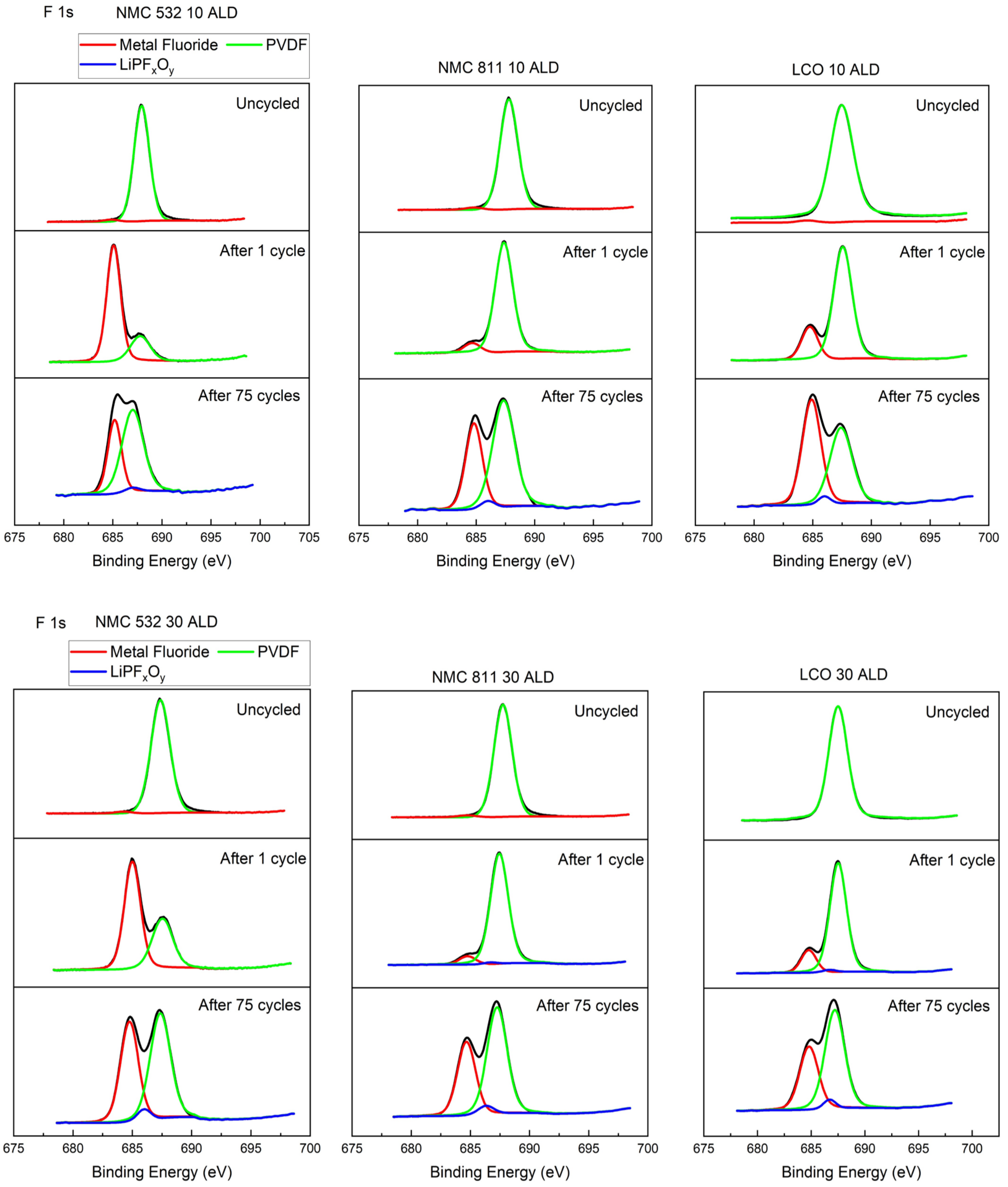

Figure 5.19: Fitted F 1s spectra of (from top to bottom row) 10 ALD and 30 ALD, (from left to right) NMC 532, NMC 811 and LCO FS cathode samples. The cathode samples are tested before cycling, after 1 cycle and after 75 cycles.

In the F 1s scan, the strong peak associated with metal fluoride at 684.8 eV is observed after cycling. The uncoated cathodes also exhibit this peak, but only after 75 cycles (fig 4.18). In the ALD coated cathodes, the presence of this peak after 1 cycle, could imply that the metal fluoride formed is Al-F. This could indicate that the Al_2O_3 coating layer acts as an HF scavenger, which lowers the acidity of the electrolyte near the cathode surface. Consequently, the electrolyte/electrode parasitic interfacial reaction is suppressed [148, 133]. The peak at 687.5 eV represents PVDF, while the peak at 685.6 eV is due to the presence of $LiPF_xO_y$ contaminant.

By acting as an HF scavenger and aiding in the formation of a stable CEI film, the Al_2O_3 coated cathodes considerably minimised the electrolyte decomposition, as may be inferred from the aforementioned observations. This reduces the accumulation of inorganic contaminants like LiF, $LiPF_xO_y$ and Li_2CO_3 on the cathode surface.

5.3.8. NMR Results

In this study, the NMR experiments were performed on two different nuclei, ^{27}Al and ^{7}Li. The latter is solely used for LCO 30 ALD cathodes, in order to monitor changes in their lithium environment. Due to the existence of paramagnetic centres, the ^{7}Li measurements on NMCs were difficult to measure, and no clear information could be inferred. All the 30 ALD cathodes were investigated with ^{27}Al NMR to examine how the Al_2O_3 coating layer changes with cycling and contrast how this affects the cathodes' performance.

^{27}Al NMR

The results for the ^{27}Al NMR spectra for NMC 532, NMC 811 and LCO cathodes are shown in fig 5.20. In both the NMC and LCO spectra, the peak at 9 ppm indicates the presence of 6-coordinate Al environments within the coating. This central peak denotes the presence of Al_2O_3 and/or $Al(OH)_3$ [184, 185]. However, none of the scans produced a separate resonance for the 4-coordinate $LiAlO_2$. The peak intensity differences observed between the 4- and 6- coordinate peaks were very minimal, which may mean that less $LiAlO_2$ was formed after cycling [186].

When comparing the peaks of the NMC cathodes, it can be seen that cycling had no effect on the peak position. The fact that the ^{27}Al is a quadrupolar nucleus, which produces broad signals, may be one of the reasons of this lack of change in the spectra of ^{27}Al. For a quadrupolar nucleus, the charge distribution around its nucleus is anisotropic, making it sensitive to the symmetry of the electric field gradient of its surrounding. Line broadening occurs if this electric field gradient is not symmetric [162, 187].

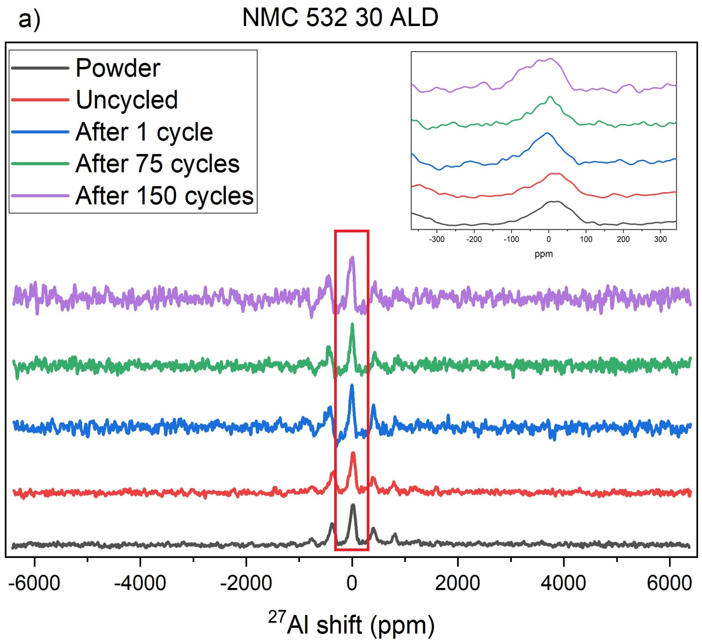

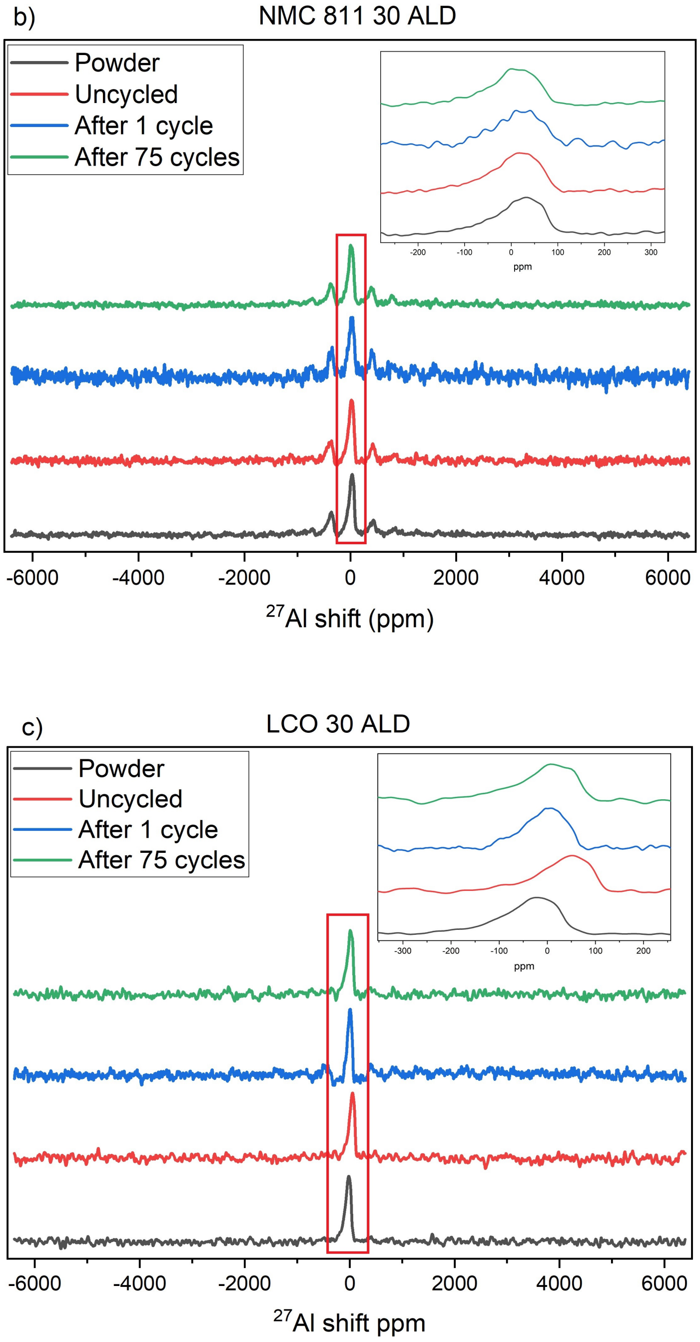

Figure 5.20: ^{27}Al solid state NMR spectra of a) NMC 532, b) NMC 811 and c) LCO 30 ALD powder and FS cathode samples.

The identical peak positions may also result from the increased presence of unpaired paramagnetic Ni^{2+}/Ni^{3+} and Mn^{4+} metal centers surrounding Al in the NMCs. This diminishes their resolution by hyperfine interaction, resulting in paramagnetic broadening, as seen in the spectra [188, 189]. Half-integer quadrupolar nuclei in paramagnetic systems experience both the paramagnetic effects and the quadrupolar interaction, which contributes to the lineshape and, as a result, makes it extremely difficult to extract NMR parameters [190]. From the ^{27}Al NMR spectra of the LCO samples (fig 5.20c), it can be seen that the uncycled LCO cathode exhibits a peak shift to $\approx$ 56 ppm. This could signify the formation of 4-coordinate α-$LiAlO_2$ phase, owing to the interfacial reaction between the alumina coating layer with the lithium species on the surface of the cathode [185]. This phase, however disappears after cycling as observed in the spectra.

In order to determine whether the storage environment had an impact on the peak resonances, a fresh batch of NMC 622 powder samples prepared under different storage conditions were subjected to ^{27}Al NMR measurement. The results (see B.15) showed that leaving the samples in ambient atmosphere produced large, distinct peaks in the spectra. This indicates that the storage environment has an effect on the peak resonances observed.

Overall, the findings from this work's ^{27}Al NMR were insufficient to explain how cycling affects the aluminium environment. A different strategy using high magnetic fields and high rotor spinning speed might help to lessen quadrupolar interactions and create distinct resonances [191, 192].

^{7}Li NMR

The spectra for the ^{7}Li NMR on the 30 ALD LCO samples are shown in fig 5.21.

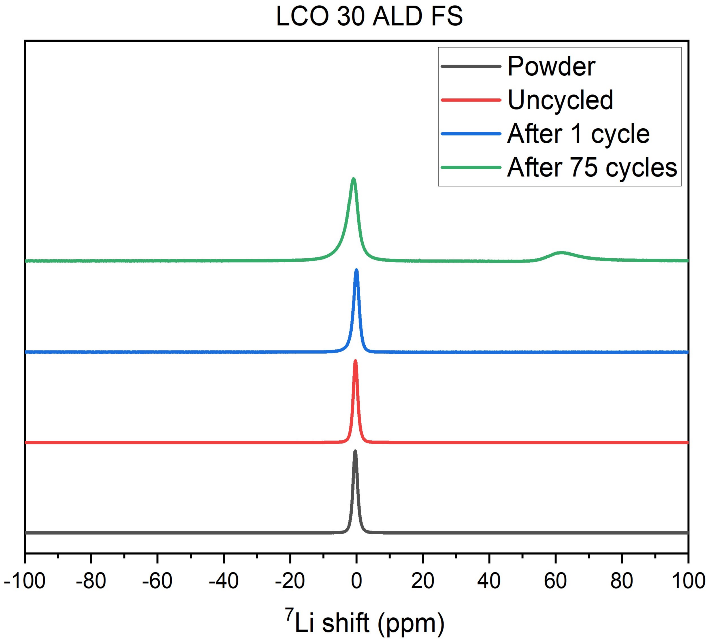

Figure 5.21: ^{7}Li Solid State NMR spectra of LCO 30 ALD powder and FS cathode samples.

The clear peak at 0 ppm in the spectra is attributed to the lithium ions inside the LCO. From the spectra, it can be observed that there is no change in the central peak position over cycling. However, after 75 cycles, the presence of a weak resonance can be observed at 60 ppm. The formation of a lithiated spinel phase (Li_xCoO_2) in the LCO, is thought to be the cause of this resonance. A lithiated spinel phase forms when the LCO starts to show a metallic behaviour after a particular level of lithiation. Electronic delocalisation within LCO is the cause of this. Due to the involvement of lithium's orbitals in the conduction band, the nature of the hyperfine interaction it experiences, changes from Fermi shift to a Knight shift as a result, leading to a weak resonance becoming apparent in the spectra [193, 194, 195].

Overall, the ^{7}Li NMR successfully demonstrated how cycling affects the spectra due to the changes in the oxidation states of cobalt ions present in LCO. Furthermore, this also indicated the presence of a reversible first order phase transition after long term cycling.

5.4. Conclusion

The chapter's goal was to look into how the the ALD coating impacted the NMC and LCO cathodes during cycling. The behaviour of the cathodes was examined using a variety of tests, including electrochemical cycling, EIS, SEM, XRD, XPS, and NMR. The results were contrasted with those seen in the previous chapter, with uncoated cathodes.

The results showed that coating the cathodes with Al_2O_3 drastically improved their cycling performances. These cathodes also saw a lower charge transfer resistance due to the presence of a stable CEI layer, which enhances the transport of lithium ions. By acting as an HF scavenger, the Al_2O_3 in the ALD coated cathodes assisted to produce a cathode surface that was nearly free of impurities. As a result, the cathode surface was stable and free of microcracks, which inhibited the development of microstrain and minimised electrolyte decomposition during cycling. Thus, coating the cathodes with ALD proved to be successful in improving its performance, specifically during the long term cycling.

6

Conclusion and Outlook

6.1. Conclusion

The aim of this thesis was to gain insight into the chemistry of uncoated and ALD coated cathodes during electrochemical cycling. This research was performed on three different LIB cathode materials: NMC 532, NMC 811 and LCO. Furthermore, this investigation demanded the usage of a free-standing cathode, which was made and cycled in a half cell configuration. To address the research questions of this thesis, these cathodes were further tested using different characterization techniques.

According to the literature reviewed in chapter 2, there is a lot of room for doing LIB research with ALD coated FS cathodes to keep enhancing its cycling behaviour. These cathodes could potentially be put through tests at high potentials and at various temperatures to evaluate any changes in their cycling behaviour. The conclusions drawn from chapters 4 and 5 of this study, provide answers to the research questions posed in chapter 3 of this thesis. The answers are given below.

How are FS cathodes made and how does the cycling performance of a FS cathode compare against a cathode with aluminium current collector?

In the current work, a release liner is used for making FS cathodes, which are then meticulously extracted to create the cathode. These cathodes show very similar cycling behaviour to the cathodes with the aluminium current collector, as depicted in chapter 4. From SEM observation, it was discovered that the structure was identical for both the cathodes. This outcome provided the motivation to carry out the remainder of the research, specifically the elemental characterizations, using FS cathodes.

What are the changes in cycling behaviour of an ALD coated cathode compared to an uncoated cathode?

In comparison to uncoated cathodes, the ALD coated cathodes exhibit improved cycling stability, as shown in chapter 5. The presence of the Al_2O_3 layer facilitates the formation of a stable CEI, which reduces the impedance by enhancing the diffusion of lithium ions into the cathode lattice.

The uncoated cathodes experienced capacity fading during long term cycling, as a result of electrolyte decomposition brought on by the unstable CEI layer. This caused the appearance of microcracks on their surface observed by SEM, resulting in microstrain observed by XRD and Rietveld refinement. The complete absence of this phenomena in the ALD coated cathodes demonstrated the beneficial role played by Al_2O_3 in preventing lattice collapse. Additionally, to obtain high capacities during cycling, it is advised to keep the ALD coating as thin as possible, to prevent any hindrance in lithium and electron transport.

What are the elemental changes observed for the coated and uncoated cathodes when subjected *to electrochemical cycling?*

From the surface analysis of the cathode samples using XPS, it was found that the uncoated cathode powders had impurities on their surface, as a result of a moisture-induced reaction with the surface elements present. These impurities were significantly reduced when Al_2O_3 was applied to these powders through ALD.

The uncoated cathodes, after long term cycling, had contaminants from electrolyte decomposition present on their surface, which was discovered using XPS in chapter 4. These contaminants began to form during the initial cycle and gradually grew in quantity upon cycling for long. Upon coating the cathodes with Al_2O_3, these contaminants were greatly diminished. Al_2O_3 acts as an HF scavenger and prevents electrolyte oxidation in the cells containing the coated cathodes, ensuring good cycle stability.

How does the aluminium environment change for an ALD coated cathode over cycling?

After cycling, the alumina layer on the cathode surface was still clearly apparent, as was found using XPS in chapter 5. However, the NMR findings failed to provide conclusive evidence about the changes that occur in the aluminium environment over cycling. The findings of chapter 5 show that the resolution was insufficient to detect distinct peak changes between the scans.

In conclusion, the application of ALD to coat the cathodes was successful in reducing electrolyte decomposition and displaying an improved performance. This demonstrates its suitability for use in a commercial LIB for enhanced performance. The goal of this effort, which was to examine the cathode chemistry using multiple techniques, was also considerably aided by the use of a FS cathode.

6.2. Further Scope of Research

The findings of this thesis offer a variety of intriguing possibilities for further research. As stated in chapter 2, the main goal of this thesis was to examine the behaviour of cathodes. Hence, a half cell with lithium as anode was employed. Future work on the ALD coated cathodes, could employ a full cell for cathode investigation. Graphite serves as the anode in a commercial LIB cell, which can both limit the growth of lithium dendrites and aid in the analysis of the cell's behaviour as a whole [19].

A particularly interesting future avenue for the FS cathodes would be to enhance its degree of flexibility. This would be extremely valuable when used in flexible electronic devices. The FS cathodes used in this study frequently broke apart when bent past a certain threshold. Future research could alter the cathode-making process to help create an electrode with a high degree of flexibility.

An existing challenge that is faced by commercial LIBs, is their performance at high voltage and high rate conditions. For the LIB cathode materials, higher voltage cycling above 4.5 V vs Li^+/Li is necessary in order to attain high capacities. This is hampered by the presence of $LiPF_6$ electrolyte, which causes the dissolution of transition metals and irreversible phase transitions, when cycling at high voltages. Future research could look into an alternative electrolyte. Polymer electrolytes have demonstrated reasonable success in this regard [196, 197, 198].

In this work, XPS was used to identify the stoichiometry of the elements present on the cathode surfaces, as shown in chapters 4 and 5. However, the scans for transition metal elements yielded a weak signal, making it ineffective to examine them. The high background detected could have several causes, one of which being surface contamination [199]. In order to avoid this contamination, care should be taken when handling the sample. Increasing the number of scans for these elements can be another approach to attempt, in order to obtain a clear signal.

As stated in chapter 5, the ^{27}Al NMR experiments could be carried out at a high magnetic field and with high spinning speeds to detect clear resonances and minimise the quadrupolar interactions, when studying the aluminium environment in cathodes.

References

[1] Dave Murden. *WHAT ARE THE 14 MOST POPULAR APPLICATIONS USES OF LITHIUM BATTERIES*. 2022. URL: `https://ecotreelithium.co.uk/news/lithium-batteries-uses-and-applications/`.

[2] Nathaniel Bullard. *This Is the Dawning of the Age of the Battery*. 2020. URL: `https://www.bloomberg.com/news/articles/2020-12-17/this-is-the-dawning-of-the-age-of-the-battery`.

[3] Johnny Wood. *Batteries are a key part of the energy transition. Here's why*. 2021. URL: `https://www.weforum.org/agenda/2021/09/batteries-lithium-ion-energy-storage-circular-economy/`.

[4] Andreas Breiter, Evan Horetsky, Martin Linder, and Raphael Rettig. *Power spike: How battery makers can respond to surging demand from EVs*. 2022. URL: `https://www.mckinsey.com/capabilities/operations/our-insights/power-spike-how-battery-makers-can-respond-to-surging-demand-from-evs`.

[5] Beth E Murdock, Kathryn E Toghill, and Nuria Tapia-Ruiz. "A perspective on the sustainability of cathode materials used in lithium-ion batteries". In: *Advanced Energy Materials* 11.39 (2021), p. 2102028.

[6] Arumugam Manthiram. "A reflection on lithium-ion battery cathode chemistry". In: *Nature communications* 11.1 (2020), p. 1550.

[7] Monu Malik, Ka Ho Chan, and Gisele Azimi. "Review on the synthesis of LiNixMnyCo1-x-yO2 (NMC) cathodes for lithium-ion batteries". In: *Materials Today Energy* 28 (2022), p. 101066.

[8] Seung-Yong Lee et al. "Revisiting primary particles in layered lithium transition-metal oxides and their impact on structural degradation". In: *Advanced Science* 6.6 (2019), p. 1800843.

[9] Kenji Fukuda et al. "Foliated natural graphite as the anode material for rechargeable lithium-ion cells". In: *Journal of power sources* 69.1-2 (1997), pp. 165–168.

[10] Hao Zhang et al. "Graphite as anode materials: Fundamental mechanism, recent progress and advances". In: *Energy Storage Materials* 36 (2021), pp. 147–170.

[11] Doron Aurbach et al. "Design of electrolyte solutions for Li and Li-ion batteries: a review". In: *Electrochimica acta* 50.2-3 (2004), pp. 247–254.

[12] Julian Kalhoff et al. "Safer electrolytes for lithium-ion batteries: state of the art and perspectives". In: *ChemSusChem* 8.13 (2015), pp. 2154–2175.

[13] Yuede Pan et al. "Functional membrane separators for next-generation high-energy rechargeable batteries". In: *National Science Review* 4.6 (2017), pp. 917–933.

[14] Sheng Shui Zhang. "A review on the separators of liquid electrolyte Li-ion batteries". In: *Journal of power sources* 164.1 (2007), pp. 351–364.

[15] Mitsuru Yamada et al. "Review of the design of current collectors for improving the battery performance in lithium-ion and post-lithium-ion batteries". In: *Electrochem* 1.2 (2020), pp. 124–159.

[16] Vivian Murray, David S Hall, and JR Dahn. "A guide to full coin cell making for academic researchers". In: *Journal of The Electrochemical Society* 166.2 (2019), A329–A333.

[17] Lénaïc Madec and Hervé Martinez. "Impact of the metal electrode size in half-cells studies: Example of graphite/Li coin cells". In: *Electrochemistry Communications* 90 (2018), pp. 61–64.

[18] Gabin Yoon et al. "Deposition and stripping behavior of lithium metal in electrochemical system: continuum mechanics study". In: *Chemistry of Materials* 30.19 (2018), pp. 6769–6776.

[19] Muhammad-Sadeeq Balogun et al. "A review of the development of full cell lithium-ion batteries: The impact of nanostructured anode materials". In: *Nano research* 9 (2016), pp. 2823–2851.

[20] Christophe R Birkl et al. “A parametric open circuit voltage model for lithium ion batteries”. In: *Journal of The Electrochemical Society* 162.12 (2015), A2271.

[21] Jiadeng Zhu et al. “Understanding glass fiber membrane used as a novel separator for lithium–sulfur batteries”. In: *Journal of membrane science* 504 (2016), pp. 89–96.

[22] Yue-E Miao et al. “Electrospun polyimide nanofiber-based nonwoven separators for lithium-ion batteries”. In: *Journal of Power Sources* 226 (2013), pp. 82–86.

[23] John S Okasinski et al. “In situ X-ray spatial profiling reveals uneven compression of electrode assemblies and steep lateral gradients in lithium-ion coin cells”. In: *Physical Chemistry Chemical Physics* 22.38 (2020), pp. 21977–21987.

[24] Allan J Jacobson and Linda F Nazar. “Intercalation chemistry”. In: *Encyclopedia of Inorganic Chemistry* (2006).

[25] Apurba Ray and Bilge Saruhan. “Application of ionic liquids for batteries and supercapacitors”. In: *Materials* 14.11 (2021), p. 2942.

[26] Sungjemmenla et al. “Understanding the Cathode–Electrolyte Interphase in Lithium-Ion Batteries”. In: *Energy Technology* 10.9 (2022), p. 2200421.

[27] Huaping Wang et al. “Formation and modification of cathode electrolyte interphase: A mini review”. In: *Electrochemistry Communications* 122 (2021), p. 106870.

[28] Nan Zhang et al. “Modified cathode-electrolyte interphase toward high-performance batteries”. In: *Cell Reports Physical Science* (2022).

[29] Yoon Seok Jung et al. “Unexpected improved performance of ALD coated LiCoO2/graphite Li-ion batteries”. In: *Advanced Energy Materials* 3.2 (2013), pp. 213–219.

[30] Yan Jin et al. “Stabilizing Interfacial Reactions for Stable Cycling of High-Voltage Sodium Batteries”. In: *Advanced Functional Materials* 32.40 (2022), p. 2204995.

[31] Rui Martim Salgado et al. “The latest trends in electric vehicles batteries”. In: *Molecules* 26.11 (2021), p. 3188.

[32] Kai Wang et al. “Recent advances and historical developments of high voltage lithium cobalt oxide materials for rechargeable Li-ion batteries”. In: *Journal of Power Sources* 460 (2020), p. 228062.

[33] Jeffrey W Fergus. “Recent developments in cathode materials for lithium ion batteries”. In: *Journal of power sources* 195.4 (2010), pp. 939–954.

[34] Benjamin L Brugman et al. “Cobalt Blues: an overview of the thermodynamics of a critical element in short supply”. In: *Materials Today Energy* (2023), p. 101382.

[35] Naoki Nitta et al. “Li-ion battery materials: present and future”. In: *Materials today* 18.5 (2015), pp. 252–264.

[36] Tianyu Li et al. “Degradation mechanisms and mitigation strategies of nickel-rich NMC-based lithium-ion batteries”. In: *Electrochemical Energy Reviews* 3 (2020), pp. 43–80.

[37] Angelika Basch et al. “Chemical delithiation and exfoliation of LixCoO2”. In: *Journal of Solid State Chemistry* 220 (2014), pp. 102–110.

[38] Christian M Julien and Alain Mauger. “NCA, NCM811, and the route to Ni-richer lithium-ion batteries”. In: *Energies* 13.23 (2020), p. 6363.

[39] Chixia Tian, Feng Lin, and Marca M Doeff. “Electrochemical characteristics of layered transition metal oxide cathode materials for lithium ion batteries: surface, bulk behavior, and thermal properties”. In: *Accounts of chemical research* 51.1 (2017), pp. 89–96.

[40] Patrick Rozier and Jean Marie Tarascon. “Li-rich layered oxide cathodes for next-generation Li-ion batteries: chances and challenges”. In: *Journal of The Electrochemical Society* 162.14 (2015), A2490.

[41] Florian Schipper et al. “Recent advances and remaining challenges for lithium ion battery cathodes”. In: *Journal of The Electrochemical Society* 164.1 (2016), A6220.

[42] Shixuan Wang et al. “Enabling stable and high-rate cycling of a Ni-rich layered oxide cathode for lithium-ion batteries by modification with an artificial Li+-conducting cathode-electrolyte interphase”. In: *Journal of Materials Chemistry A* 9.19 (2021), pp. 11623–11631.

[43] LS Kanevskii and VS Dubasova. “Degradation of lithium-ion batteries and how to fight it: A review”. In: *Russian Journal of Electrochemistry* 41 (2005), pp. 1–16.

[44] Yoon Seok Jung et al. “Enhanced stability of LiCoO2 cathodes in lithium-ion batteries using surface modification by atomic layer deposition”. In: *Journal of The Electrochemical Society* 157.1 (2009), A75.

[45] Christoph R Birkl et al. “Degradation diagnostics for lithium ion cells”. In: *Journal of Power Sources* 341 (2017), pp. 373–386.

[46] Jijiang Huang et al. “Flexible Free-Standing VO2 (B) Nanobelt Films as Additive-Free Cathode for Lithium-Ion Batteries”. In: *International Journal of Electrochemical Science* 6.5 (2011), pp. 1709–1719.

[47] Liya Guo et al. “Degradation in lithium ion battery current collectors”. In: *Journal of Physics: Energy* 3.3 (2021), p. 032015.

[48] Agnieszka Gabryelczyk et al. “Corrosion of aluminium current collector in lithium-ion batteries: A review”. In: *Journal of Energy Storage* 43 (2021), p. 103226.

[49] Sekar Praveen et al. “3D-printed self-standing electrodes for flexible Li-ion batteries”. In: *Applied Materials Today* 26 (2022), p. 100980.

[50] Chenfei Shen et al. “Hierarchical carbon-coated ball-milled silicon: synthesis and applications in free-standing electrodes and high-voltage full lithium-ion batteries”. In: *ACS nano* 12.6 (2018), pp. 6280–6291.

[51] AM Kannan, Lew Rabenberg, and A Manthiram. “High capacity surface-modified LiCoO2 cathodes for lithium-ion batteries”. In: *Electrochemical and solid-state letters* 6.1 (2002), A16.

[52] Xiaokai Ding et al. “An ultra-long-life lithium-rich Li1. 2Mn0. 6Ni0. 2O2 cathode by three-in-one surface modification for lithium-ion batteries”. In: *Angewandte Chemie International Edition* 59.20 (2020), pp. 7778–7782.

[53] Dina Becker et al. “Surface modification of Ni-rich LiNi0. 8Co0. 1Mn0. 1O2 cathode material by tungsten oxide coating for improved electrochemical performance in lithium-ion batteries”. In: *ACS applied materials & interfaces* 11.20 (2019), pp. 18404–18414.

[54] David S Hall et al. “New chemical insights into the beneficial role of Al2O3 cathode coatings in lithium-ion cells”. In: *ACS applied materials & interfaces* 11.15 (2019), pp. 14095–14100.

[55] Juliya Jeyakumar et al. “Surface-modified quaternary layered Ni-rich cathode materials by Li2ZrO3 for improved electrochemical performance for high-power Li-ion batteries”. In: *ACS Applied Energy Materials* 5.4 (2022), pp. 4796–4807.

[56] Sung-Beom Kim et al. “Li-ion diffusivity and electrochemical performance of Ni-rich cathode material doped with fluoride ions”. In: *Journal of Power Sources* 506 (2021), p. 230219.

[57] Chih-Chieh Wang et al. “Nanolaminated ZnO–TiO2 coated lithium-rich layered oxide cathodes by atomic layer deposition for enhanced electrochemical performances”. In: *Journal of Alloys and Compounds* 842 (2020), p. 155845.

[58] Junchao Chen et al. “LiNi0. 8Co0. 15Al0. 05O2 cathodes exhibiting improved capacity retention and thermal stability due to a lithium iron phosphate coating”. In: *Electrochimica Acta* 312 (2019), pp. 179–187.

[59] Seong-Ju Sim et al. “Use of carbon coating on LiNi0. 8Co0. 1Mn0. 1O2 cathode material for enhanced performances of lithium-ion batteries”. In: *Scientific Reports* 10.1 (2020), p. 11114.

[60] Yang Li et al. “Stabilizing the (003) Facet of Micron-Sized LiNi0. 6Co0. 2Mn0. 2O2 Cathode Material Using Tungsten Oxide as an Exemplar”. In: *Inorganics* 10.8 (2022), p. 111.

[61] Junqing Yan et al. “Recent progress on the modification of high nickel content NCM: Coating, doping, and single crystallization”. In: *Interdisciplinary Materials* 1.3 (2022), pp. 330–353.

[62] Seungsuk Oh et al. “Effect of Al2O3 coating on electrochemical performance of LiCoO2 as cathode materials for secondary lithium batteries”. In: *Journal of Power Sources* 132.1-2 (2004), pp. 249–255.

[63] Elise R Østli et al. “Limitations of Ultrathin Al2O3 Coatings on LNMO Cathodes”. In: *ACS omega* 6.45 (2021), pp. 30644–30655.

[64] Sina Karimzadeh et al. “Emerging Atomic Layer Deposition for the Development of High-Performance Lithium-Ion Batteries”. In: *Electrochemical Energy Reviews* 6.1 (2023), p. 24.

[65] Debasish Mohanty et al. “Modification of Ni-rich FCG NMC and NCA cathodes by atomic layer deposition: preventing surface phase transitions for high-voltage lithium-ion batteries”. In: *Scientific reports* 6.1 (2016), p. 26532.

[66] Yantao Su et al. “Enhancing the high-voltage cycling performance of LiNi0. 5Mn0. 3Co0. 2O2 by retarding its interfacial reaction with an electrolyte by atomic-layer-deposited Al2O3”. In: *ACS applied materials & interfaces* 7.45 (2015), pp. 25105–25112.

[67] Kuok Hau Seng et al. “Free-standing V2O5 electrode for flexible lithium ion batteries”. In: *Electrochemistry Communications* 13.5 (2011), pp. 383–386.

[68] Chih-Hung Chen et al. “Simple way of making free-standing cathode electrodes for flexible lithium-ion batteries”. In: *RSC advances* 12.15 (2022), pp. 9249–9255.

[69] Jun Wang. “Development of new electrode materials for lithium ion batteries and lithium oxygen batteries”. In: (2016).

[70] Dafang He et al. “A flexible free-standing FeF3/reduced graphene oxide film as cathode for advanced lithium-ion battery”. In: *Journal of Alloys and Compounds* 909 (2022), p. 164702.

[71] Carl D Reynolds et al. “Rheology and Structure of Lithium-Ion Battery Electrode Slurries”. In: *Energy Technology* 10.10 (2022), p. 2200545.

[72] W Blake Hawley and Jianlin Li. “Beneficial rheological properties of lithium-ion battery cathode slurries from elevated mixing and coating temperatures”. In: *Journal of Energy Storage* 26 (2019), p. 100994.

[73] Werner Bauer and Dorit Nötzel. “Rheological properties and stability of NMP based cathode slurries for lithium ion batteries”. In: *Ceramics International* 40.3 (2014), pp. 4591–4598.

[74] Sung Hoon Ha, Yo Sub Jeong, and Yun Jung Lee. “Free standing reduced graphene oxide film cathodes for lithium ion batteries”. In: *ACS applied materials & interfaces* 5.23 (2013), pp. 12295–12303.

[75] Yang-kyu Park et al. “Robust free-standing electrodes for flexible lithium-ion batteries prepared by a conventional electrode fabrication process”. In: *Electrochimica Acta* 247 (2017), pp. 371–380.

[76] Guangmin Zhou, Feng Li, and Hui-Ming Cheng. “Progress in flexible lithium batteries and future prospects”. In: *Energy & Environmental Science* 7.4 (2014), pp. 1307–1338.

[77] Zlata Kelar Tučeková et al. “Adhesive Properties of Silicone-Coated Release Liner Paper Enhanced by Atmospheric Pressure Plasma Pre-and Post-Treatment”. In: *Coatings* 10.11 (2020), p. 1102.

[78] Ben Rowden and Nuria Garcia-Araez. “Estimating lithium-ion battery behavior from half-cell data”. In: *Energy Reports* 7 (2021), pp. 97–103.

[79] Xuming Yang and Andrey L Rogach. “Electrochemical techniques in battery research: a tutorial for nonelectrochemists”. In: *Advanced Energy Materials* 9.25 (2019), p. 1900747.

[80] Anke Parschau et al. “Cycle Tests on the Influence of Different Charging Currents—A Case Study on Different Commercial, Cylindrical Lithium Ion Cells”. In: *Batteries* 9.2 (2023), p. 83.

[81] Muhammad Rashid and Amit Gupta. “Effect of relaxation periods over cycling performance of a Li-ion battery”. In: *Journal of The Electrochemical Society* 162.2 (2015), A3145.

[82] Wesley M Dose et al. “Effect of anode slippage on cathode cutoff potential and degradation mechanisms in Ni-rich Li-ion batteries”. In: *Cell Reports Physical Science* 1.11 (2020).

[83] Chengyu Mao et al. “Identifying the limiting electrode in lithium ion batteries for extreme fast charging”. In: *Electrochemistry communications* 97 (2018), pp. 37–41.

[84] H Xia et al. “Electrochemical behavior and Li diffusion study of LiCoO□ thin film electrodes prepared by PLD”. In: (2007).

[85] Matthieu Dubarry, Arnaud Devie, and Bor Yann Liaw. “The value of battery diagnostics and prognostics”. In: *J. Energy Power Sources* 1.5 (2014), pp. 242–249.

[86] Ashley Fly and Rui Chen. “Rate dependency of incremental capacity analysis (dQ/dV) as a diagnostic tool for lithium-ion batteries”. In: *Journal of Energy Storage* 29 (2020), p. 101329.

[87] *Investigating battery aging using Differential Capacity Analysis (DCA)*. 2023. URL: `https://www.biologic.net/topics/investigating-battery-ageing-using-differential-capacity-analysis-dca/`.

[88] Nina Meddings et al. “Application of electrochemical impedance spectroscopy to commercial Li-ion cells: A review”. In: *Journal of Power Sources* 480 (2020), p. 228742.

[89] Miran Gaberšček. “Understanding Li-based battery materials via electrochemical impedance spectroscopy”. In: *Nature Communications* 12.1 (2021), p. 6513.

[90] *RelaxIS*. URL: `https://www.rhd-instruments.de/en/products/software/relaxis`.

[91] Krisztina J Szekeres et al. “Methods for the Determination of Valid Impedance Spectra in Non-stationary Electrochemical Systems: Concepts and Techniques of Practical Importance”. In: *ChemElectroChem* 8.7 (2021), pp. 1233–1250.

[92] Cameron W Tanner, Kuan-Zong Fung, and Anil V Virkar. “The effect of porous composite electrode structure on solid oxide fuel cell performance: I. theoretical analysis”. In: *Journal of the Electrochemical Society* 144.1 (1997), p. 21.

[93] Kalsoom Akhtar et al. “Scanning electron microscopy: Principle and applications in nanomaterials characterization”. In: *Handbook of materials characterization* (2018), pp. 113–145.

[94] *Scanning Electron Microscopy*. 2023. URL: `https://www.nanoscience.com/techniques/scanning-electron-microscopy/`.

[95] M Abd Mutalib et al. “Scanning electron microscopy (SEM) and energy-dispersive X-ray (EDX) spectroscopy”. In: *Membrane characterization*. Elsevier, 2017, pp. 161–179.

[96] Debasish Mohanty et al. “Structural transformation of a lithium-rich Li1. 2Co0. 1Mn0. 55Ni0. 15O2 cathode during high voltage cycling resolved by in situ X-ray diffraction”. In: *Journal of Power Sources* 229 (2013), pp. 239–248.

[97] Zhonghua Lu and Jeff R Dahn. “Understanding the anomalous capacity of Li/Li [Ni x Li (1/3-2x/3) Mn (2/3- x/3)] O 2 cells using in situ X-ray diffraction and electrochemical studies”. In: *Journal of the Electrochemical Society* 149.7 (2002), A815.

[98] Kyung-Wan Nam et al. “In situ X-ray diffraction studies of mixed LiMn2O4–LiNi1/3Co1/3Mn1/3O2 composite cathode in Li-ion cells during charge–discharge cycling”. In: *Journal of power sources* 192.2 (2009), pp. 652–659.

[99] Andrei A Bunaciu, Elena Gabriela UdriŞTioiu, and Hassan Y Aboul-Enein. “X-ray diffraction: instrumentation and applications”. In: *Critical reviews in analytical chemistry* 45.4 (2015), pp. 289–299.

[100] Worku Wubet Andualem. “GREEN SYNTHESIS OF CUO NANOPARTICLES FOR THE APPLICATION OF DYE SENSITIZED SOLAR CELL”. In: (2020).

[101] Marcus H Mendenhall, David Black, and James P Cline. “The optics of focusing bent-crystal monochromators on X-ray powder diffractometers with application to lattice parameter determination and microstructure analysis”. In: *Journal of applied crystallography* 52.5 (2019), pp. 1087–1094.

[102] Andrei N Salak et al. “High-power ultrasonic synthesis and magnetic-field-assisted arrangement of nanosized crystallites of cobalt-containing layered double hydroxides”. In: *ChemEngineering* 3.3 (2019), p. 62.

[103] *Match! - Phase Analysis using Powder Diffraction*. URL: `https://www.crystalimpact.com/match/`.

[104] *GSAS-II - Crystallographic Data Analysis Software*. URL: `https://subversion.xray.aps.anl.gov/trac/pyGSAS`.

[105] James L White et al. “Nickel and cobalt oxidation state evolution at Ni-rich NMC cathode surfaces during treatment”. In: *The Journal of Physical Chemistry C* 124.30 (2020), pp. 16508–16514.

[106] L.J. Bannenberg. *X-ray Spectroscopy, CH3765 Advanced Materials Analysis by Radiation Instrumentation*. 2022.

[107] XD Huang et al. “Electrochemical performance of thermally-grown SiO 2 as diffusion barrier layer for integrated lithium-ion batteries”. In: *Frontiers in Energy* 12 (2018), pp. 225–232.

[108] Ida Källquist et al. “Advances in studying interfacial reactions in rechargeable batteries by photoelectron spectroscopy”. In: *Journal of Materials Chemistry A* 10.37 (2022), pp. 19466–19505.

[109] *CasaXPS: Processing Software for XPS, AES, SIMS and More*. URL: `http://www.casaxps.com/`.

[110] Tao Zhang et al. “Surface analysis of cobalt-enriched crushed products of spent lithium-ion batteries by X-ray photoelectron spectroscopy”. In: *Separation and Purification Technology* 138 (2014), pp. 21–27.

[111] George H Major et al. “Practical guide for curve fitting in x-ray photoelectron spectroscopy”. In: *Journal of Vacuum Science & Technology A* 38.6 (2020).

[112] *X-ray Photoelectron Spectroscopy (XPS) Reference Pages*. URL: `http://www.xpsfitting.com/`.

[113] B Vincent Crist. *Handbooks of monochromatic XPS spectra*. 2019.

[114] David Mogk. *X-Ray Photoelectron Spectroscopy (XPS; aka Electron Spectroscopy for Chemical Analysis, ESCA)*. URL: `https://serc.carleton.edu/msu_nanotech/methods/xps.html`.

[115] Ines Hamam et al. “Study of the reactions between Ni-rich positive electrode materials and aqueous solutions and their relation to the failure of Li-ion cells”. In: *Journal of the Electrochemical Society* 167.13 (2020), p. 130521.

[116] Luqman Azhari et al. “Effects of Extended Aqueous Processing on Structure, Chemistry, and Performance of Polycrystalline LiNi x Mn y Co z O2 Cathode Powders”. In: *ACS Applied Materials & Interfaces* 12.52 (2020), pp. 57963–57974.

[117] J Kasnatscheew et al. “The truth about the 1st cycle Coulombic efficiency of LiNi 1/3 Co 1/3 Mn 1/3 O 2 (NCM) cathodes”. In: *Physical chemistry chemical physics* 18.5 (2016), pp. 3956–3965.

[118] Xinyong Tian et al. “High-Performance High-Nickel Multi-Element Cathode Materials for Lithium-Ion Batteries”. In: *Batteries* 9.6 (2023), p. 319.

[119] Yongxiu Chen et al. “Revealing the rate-limiting electrode of lithium batteries at high rates and mass loadings”. In: *Chemical Engineering Journal* 450 (2022), p. 138275.

[120] Xiaoyu Zhang et al. “Direct observation of Li-ion transport in electrodes under nonequilibrium conditions using neutron depth profiling”. In: *Advanced Energy Materials* 5.15 (2015), p. 1500498.

[121] Jing Zhang et al. “Balancing particle properties for practical lithium-ion batteries”. In: *Particuology* 61 (2022), pp. 18–29.

[122] Chong S Yoon et al. “Extracting maximum capacity from Ni-rich Li [Ni 0.95 Co 0.025 Mn 0.025] O 2 cathodes for high-energy-density lithium-ion batteries”. In: *Journal of materials chemistry A* 6.9 (2018), pp. 4126–4132.

[123] Aleksandr O Kondrakov et al. “Anisotropic lattice strain and mechanical degradation of high-and low-nickel NCM cathode materials for Li-ion batteries”. In: *The journal of physical chemistry C* 121.6 (2017), pp. 3286–3294.

[124] Isaac N Lund et al. “The Cycling Performance and Surface Passivation Qualities of a Heterogeneous Amorphous NixSiOy/Polycrystalline NiSi2 Core Shell Nanowire Used as a Li-Ion Battery Anode”. In: *Journal of The Electrochemical Society* 161.12 (2014), A1772.

[125] Yingchun Lyu et al. “An overview on the advances of LiCoO2 cathodes for lithium-ion batteries”. In: *Advanced Energy Materials* 11.2 (2021), p. 2000982.

[126] Lars Bläubaum et al. “Impact of particle size distribution on performance of lithium-ion batteries”. In: *ChemElectroChem* 7.23 (2020), pp. 4755–4766.

[127] Fuqing Wang et al. “Does polarization increase lead to capacity fade?” In: *Journal of The Electrochemical Society* 167.9 (2020), p. 090549.

[128] Junbin Choi et al. “Relationship of chemical composition and moisture sensitivity in LiNi x Mn y Co1- X- Y O2 for lithium-ion batteries”. In: *Journal of Electrochemical Energy Conversion and Storage* 18.4 (2021), p. 041009.

[129] Wentao Wu et al. “Two-Step Solid State Synthesis of Medium Entropy LiNi0. 5Mn1. 5O4 Cathode with Enhanced Electrochemical Performance”. In: *Batteries* 9.2 (2023), p. 91.

[130] Rajesh Pathak et al. “Fluorinated hybrid solid-electrolyte-interphase for dendrite-free lithium deposition”. In: *Nature communications* 11.1 (2020), p. 93.

[131] R Hernandez-Maya et al. “Dynamic characterization of dendrite deposition and growth in Li-surface by electrochemical impedance spectroscopy”. In: *Journal of The Electrochemical Society* 162.4 (2015), A687.

[132] Georg Bieker, Martin Winter, and Peter Bieker. “Electrochemical in situ investigations of SEI and dendrite formation on the lithium metal anode”. In: *Physical Chemistry Chemical Physics* 17.14 (2015), pp. 8670–8679.

[133] Yongqiang Liu et al. “Atomic-scale tuned interface of nickel-rich cathode for enhanced electrochemical performance in lithium-ion batteries”. In: *Journal of Materials Science & Technology* 54 (2020), pp. 77–86.

[134] Katharina Fitzek et al. “High-frequency features in the distribution of relaxation times related to frequency dispersion effects in sofcs”. In: *Journal of The Electrochemical Society* 169.1 (2022), p. 014501.

[135] Marcel J Herzog, Daniel Esken, and Jürgen Janek. “Improved cycling performance of high-nickel NMC by dry powder coating with nanostructured fumed Al2O3, TiO2, and ZrO2: a comparison”. In: *Batteries & Supercaps* 4.6 (2021), pp. 1003–1017.

[136] Aaron Wade et al. “First cycle cracking behaviour within Ni-rich cathodes during high-voltage charging”. In: *Journal of The Electrochemical Society* (2022).

[137] Hyeseung Chung et al. “Mitigating anisotropic changes in classical layered oxide materials by controlled twin boundary defects for long cycle life Li-ion batteries”. In: *Chemistry of Materials* 34.16 (2022), pp. 7302–7312.

[138] Yong-Ning Zhou et al. “Tuning charge–discharge induced unit cell breathing in layer-structured cathode materials for lithium-ion batteries”. In: *Nature communications* 5.1 (2014), p. 5381.

[139] Eung-Ju Lee et al. “Development of microstrain in aged lithium transition metal oxides”. In: *Nano letters* 14.8 (2014), pp. 4873–4880.

[140] A Leineweber et al. “The hkl dependences of microstrain and of macrostress-induced macrostrain; a comparison for intrinsically extremely anisotropic cementite, Fe3C”. In: *Eleventh European Powder Diffraction Conference: Warsaw, September 19-22, 2008*. OLDENBOURG WISSENSCHAFTSVERLAG. 2009, pp. 103–108.

[141] Francis Amalraj Susai et al. “Stabilizing Ni-rich high energy cathodes for advanced lithium-ion batteries: the case of LiNi 0.9 Co 0.1 O 2”. In: *Journal of Materials Chemistry A* 11.24 (2023), pp. 12958–12972.

[142] Dong Ren et al. “Ni-rich LiNi0. 88Mn0. 06Co0. 06O2 cathode interwoven by carbon fiber with improved rate capability and stability”. In: *Journal of Power Sources* 447 (2020), p. 227344.

[143] Ming Jiang et al. “A review of degradation mechanisms and recent achievements for Ni-rich cathode-based Li-ion batteries”. In: *Advanced Energy Materials* 11.48 (2021), p. 2103005.

[144] Jingxi Li et al. “Addressing cation mixing in layered structured cathodes for lithium-ion batteries: A critical review”. In: *Nano Materials Science* (2022).

[145] Ning Li et al. “Layered-rocksalt intergrown cathode for high-capacity zero-strain battery operation”. In: *Nature communications* 12.1 (2021), p. 2348.

[146] Hanlei Zhang et al. “Oxygen loss in layered oxide cathodes for Li-ion batteries: Mechanisms, effects, and mitigation”. In: *Chemical Reviews* 122.6 (2022), pp. 5641–5681.

[147] Bernardine LD Rinkel et al. “Two electrolyte decomposition pathways at nickel-rich cathode surfaces in lithium-ion batteries”. In: *Energy & Environmental Science* 15.8 (2022), pp. 3416–3438.

[148] Xin Wang et al. “Atomic-scale constituting stable interface for improved LiNi0. 6Mn0. 2Co0. 2O2 cathodes of lithium-ion batteries”. In: *Nanotechnology* 32.11 (2020), p. 115401.

[149] Qinghao Li et al. “Investigations on the fundamental process of cathode electrolyte interphase formation and evolution of high-voltage cathodes”. In: *ACS applied materials & interfaces* 12.2 (2019), pp. 2319–2326.

[150] Wen Liu et al. “Significantly improving cycling performance of cathodes in lithium ion batteries: the effect of Al2O3 and LiAlO2 coatings on LiNi0. 6Co0. 2Mn0. 2O2”. In: *Nano Energy* 44 (2018), pp. 111–120.

[151] Jin Wook Kim et al. “Surface chemistry of LiNi0. 5Mn1. 5O4 particles coated by Al2O3 using atomic layer deposition for lithium-ion batteries”. In: *Journal of power sources* 274 (2015), pp. 1254–1262.

[152] Edy Riyanto et al. “A review of atomic layer deposition for high lithium-ion battery performance”. In: *Journal of Materials Research and Technology* 15 (2021), pp. 5466–5481.

[153] Xifei Li et al. “Atomic layer deposition of solid-state electrolyte coated cathode materials with superior high-voltage cycling behavior for lithium ion battery application”. In: *Energy & Environmental Science* 7.2 (2014), pp. 768–778.

[154] Alan J Elliot et al. “Controlling the thickness of Josephson tunnel barriers with atomic layer deposition”. In: *arXiv preprint arXiv:1408.3077* (2014).

[155] Haiyan Lu et al. “Engineering Al2O3 atomic layer deposition: Enhanced hard carbon-electrolyte interface towards practical sodium ion batteries”. In: *Nano Energy* 64 (2019), p. 103903.

[156] JN Ding et al. “The influence of substrate on the adhesion behaviors of atomic layer deposited aluminum oxide films”. In: *Surface and Coatings Technology* 205.8-9 (2011), pp. 2846–2851.

[157] Aleksander Cholewinski et al. “Polymer binders: Characterization and development toward aqueous electrode fabrication for sustainability”. In: *Polymers* 13.4 (2021), p. 631.

[158] Wenchang Zhu et al. “Ultrathin Al2O3 coating on LiNi0. 8Co0. 1Mn0. 1O2 cathode material for enhanced cycleability at extended voltage ranges”. In: *Coatings* 9.2 (2019), p. 92.

[159] Judith Alvarado et al. “Improvement of the cathode electrolyte interphase on P2-Na2/3Ni1/3Mn2/3O2 by atomic layer deposition”. In: *ACS applied materials & interfaces* 9.31 (2017), pp. 26518–26530.

[160] Abby R Haworth, Chris W Cook, and John M Griffin. “Solid-state NMR studies of coatings and interfaces in batteries”. In: *Current Opinion in Colloid & Interface Science* (2022), p. 101638.

[161] Mohamed Haouas, Francis Taulelle, and Charlotte Martineau. “Recent advances in application of 27Al NMR spectroscopy to materials science”. In: *Progress in nuclear magnetic resonance spectroscopy* 94 (2016), pp. 11–36.

[162] APM Kentgens. “A practical guide to solid-state NMR of half-integer quadrupolar nuclei with some applications to disordered systems”. In: *Geoderma* 80.3-4 (1997), pp. 271–306.

[163] Mariluce Gonçalves Fonseca. “Spin Echo Magnetic Resonance Imaging”. In: *Imaging and Radioanalytical Techniques in Interdisciplinary Research-Fundamentals and Cutting Edge Applications*. IntechOpen, 2013.

[164] Binghong Han et al. “Understanding the role of temperature and cathode composition on interface and bulk: optimizing aluminum oxide coatings for Li-ion cathodes”. In: *ACS applied materials & interfaces* 9.17 (2017), pp. 14769–14778.

[165] Matteo Tessaro. “NMR of Cathodes for Lithium Ion Batteries”. PhD thesis. 2016.

[166] SGJ Van Meerten, WMJ Franssen, and APM Kentgens. “ssNake: A cross-platform open-source NMR data processing and fitting application”. In: *Journal of Magnetic Resonance* 301 (2019), pp. 56–66.

[167] Klaus-Ruediger Peters. “Collection deficiencies of scanning electron microscopy signal contrasts measured and corrected by differential hysteresis image processing”. In: *Scanning: The Journal of Scanning Microscopies* 18.8 (1996), pp. 539–555.

[168] Michael T Postek and András E Vladár. “Does your SEM really tell the truth? How would you know? Part 4: charging and its mitigation”. In: *Scanning Microscopies 2015*. Vol. 9636. SPIE. 2015, p. 963605.

[169] Xin Wang et al. “High-performance LiNi0. 8Mn0. 1Co0. 1O2 cathode by nanoscale lithium sulfide coating via atomic layer deposition”. In: *Journal of Energy Chemistry* 69 (2022), pp. 531–540.

[170] Sven Neudeck et al. “Effect of low-temperature Al2O3 ALD coating on Ni-rich layered oxide composite cathode on the long-term cycling performance of lithium-ion batteries”. In: *Scientific reports* 9.1 (2019), p. 5328.

[171] Franz B Spingler, Maik Naumann, and Andreas Jossen. “Capacity recovery effect in commercial LiFePO4/graphite cells”. In: *Journal of The Electrochemical Society* 167.4 (2020), p. 040526.

[172] Jaeyoung Kim et al. “Electrochemical profiling method for diagnosis of inhomogeneous reactions in lithium-ion batteries”. In: *Cell Reports Physical Science* 4.4 (2023).

[173] Erwin Hüger, Chao Jin, and Harald Schmidt. “Electrochemical investigation of ion-beam sputter-deposited carbon thin films for Li-ion batteries”. In: *Journal of Applied Electrochemistry* 52.12 (2022), pp. 1715–1732.

[174] Xiang Peng Shipai Song et al. “Improved cycling stability of LiCoO2 at 4.5 V via surface modification of cathode plates with conductive LLTO”. In: ().

[175] Yonas Tesfamhret, Reza Younesi, and Erik J Berg. “Influence of Al2O3 coatings on HF induced transition metal dissolution from lithium-ion cathodes”. In: *Journal of The Electrochemical Society* 169.1 (2022), p. 010530.

[176] Xiangbo Meng. “Atomic and molecular layer deposition in pursuing better batteries”. In: *Journal of Materials Research* 36 (2021), pp. 2–25.

[177] Jonathan Travis. “Atomic and Molecular Layer Deposition for Enhanced Lithium Ion Battery Electrodes and Development of Conductive Metal Oxide/Carbon Composites”. PhD thesis. University of Colorado at Boulder, 2015.

[178] Han Yu et al. “Recovery of Degraded Ni-Rich NMC811 Particles for Lithium-Ion Batteries”. In: *Journal of The Electrochemical Society* 169.5 (2022), p. 050520.

[179] Longlong Wang et al. “Reviving lithium cobalt oxide-based lithium secondary batteries-toward a higher energy density”. In: *Chemical Society Reviews* 47.17 (2018), pp. 6505–6602.

[180] Jaehee Song et al. “Enhanced electrochemical stability of high-voltage LiNi 0.5 Mn 1.5 O 4 cathode by surface modification using atomic layer deposition”. In: *Journal of nanoparticle research* 16 (2014), pp. 1–8.

[181] Lalith Rao et al. “Multifunctional composite binder for thick high-voltage cathodes in lithium-ion batteries”. In: *ACS Applied Materials & Interfaces* 14.1 (2021), pp. 861–872.

[182] Yuefeng Su et al. “Strategies of removing residual lithium compounds on the surface of Ni-rich cathode materials”. In: *Chinese Journal of Chemistry* 39.1 (2021), pp. 189–198.

[183] Limhi Somerville et al. “The effect of pre-analysis washing on the surface film of graphite electrodes”. In: *Electrochimica Acta* 206 (2016), pp. 70–76.

[184] Brandon R Long et al. “Enabling high-energy, high-voltage lithium-ion cells: standardization of coin-cell assembly, electrochemical testing, and evaluation of full cells”. In: *Journal of The Electrochemical Society* 163.14 (2016), A2999.

[185] Binghong Han et al. “Influence of coating protocols on alumina-coated cathode material: atomic layer deposition versus wet-chemical coating”. In: *Journal of the Electrochemical Society* 166.15 (2019), A3679.

[186] Victor Riesgo-Gonzalez et al. “Effect of Annealing on the Structure, Composition, and Electrochemistry of NMC811 Coated with Al2O3 Using an Alkoxide Precursor”. In: *Chemistry of Materials* 34.21 (2022), pp. 9722–9735.

[187] Michael Stöcker. “Review on recent NMR results”. In: *Studies in Surface Science and Catalysis*. Vol. 85. Elsevier, 1994, pp. 429–507.

[188] Binghong Han et al. “From coating to dopant: how the transition metal composition affects alumina coatings on Ni-rich cathodes”. In: *ACS applied materials & interfaces* 9.47 (2017), pp. 41291–41302.

[189] Danna Qian et al. “Electronic spin transition in nanosize stoichiometric lithium cobalt oxide”. In: *Journal of the American Chemical Society* 134.14 (2012), pp. 6096–6099.

[190] José P Carvalho et al. “Separation of quadrupolar and paramagnetic shift interactions with TOP-STMAS/MQMAS in solid-state lighting phosphors”. In: *Magnetic Resonance in Chemistry* 58.11 (2020), pp. 1055–1070.

[191] Nalinda P Wickramasinghe, Medhat Shaibat, and Yoshitaka Ishii. “Enhanced sensitivity and resolution in 1H solid-state NMR spectroscopy of paramagnetic complexes under very fast magic angle spinning”. In: *Journal of the American Chemical Society* 127.16 (2005), pp. 5796–5797.

[192] Qing Zeng et al. “Boosting resolution in NMR spectroscopy by chemical shift upscaling”. In: *Analytica Chimica Acta* 1110 (2020), pp. 109–114.

[193] Eibar Flores et al. “Operando monitoring the insulator–metal transition of LiCoO2”. In: *ACS applied materials & interfaces* 13.19 (2021), pp. 22540–22548.

[194] Michel Ménétrier et al. “The insulator-metal transition upon lithium deintercalation from LiCoO2: electronic properties and 7Li NMR study”. In: *Journal of Materials Chemistry* 9.5 (1999), pp. 1135–1140.

[195] Guozhong Lu et al. “Probing the degradation of LiCoO 2 in batteries subjected to high-voltage cycling with 17 O solid-state NMR spectroscopy”. In: *Chemical Communications* (2023).

[196] Wengao Zhao et al. “High voltage operation of Ni-rich NMC cathodes enabled by stable electrode/electrolyte interphases”. In: *Advanced energy materials* 8.19 (2018), p. 1800297.

[197] Michael Metzger et al. “Evaluating the high-voltage stability of conductive carbon and ethylene carbonate with various lithium salts”. In: *Journal of The Electrochemical Society* 167.16 (2020), p. 160522.

[198] Adam Tornheim et al. “Effect of electrolyte composition on rock salt surface degradation in NMC cathodes during high-voltage potentiostatic holds”. In: *Nano Energy* 55 (2019), pp. 216–225.

[199] D Nanda Gopala Krishna and John Philip. “Review on surface-characterization applications of X-ray photoelectron spectroscopy (XPS): Recent developments and challenges”. In: *Applied Surface Science Advances* 12 (2022), p. 100332.

A

Supplementary Information - Uncoated Cathodes

A.1. Electrochemical Cycling Performance of Pressed and Unpressed Cathode

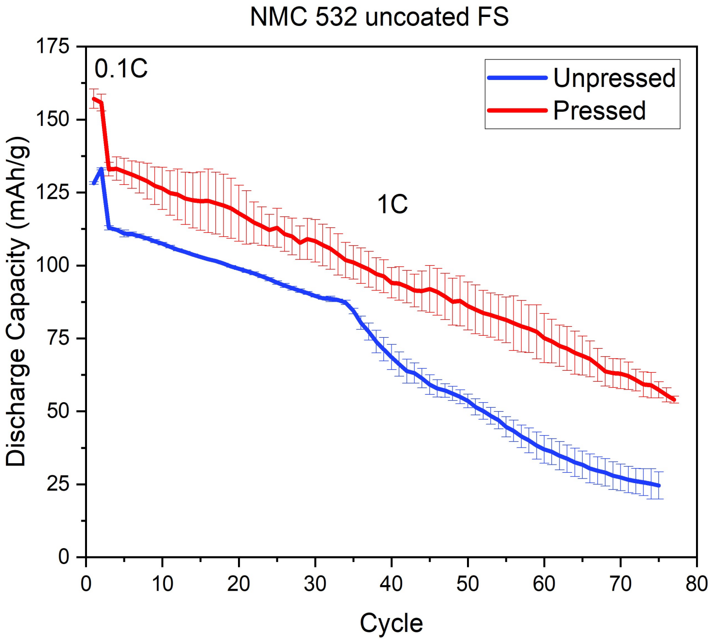

Figure A.1: Long term cycling test on uncoated NMC 532 FS cathode (pressed and unpressed).

A.2. EIS Results for Uncoated Cathodes

A.2.1. KKT Plots

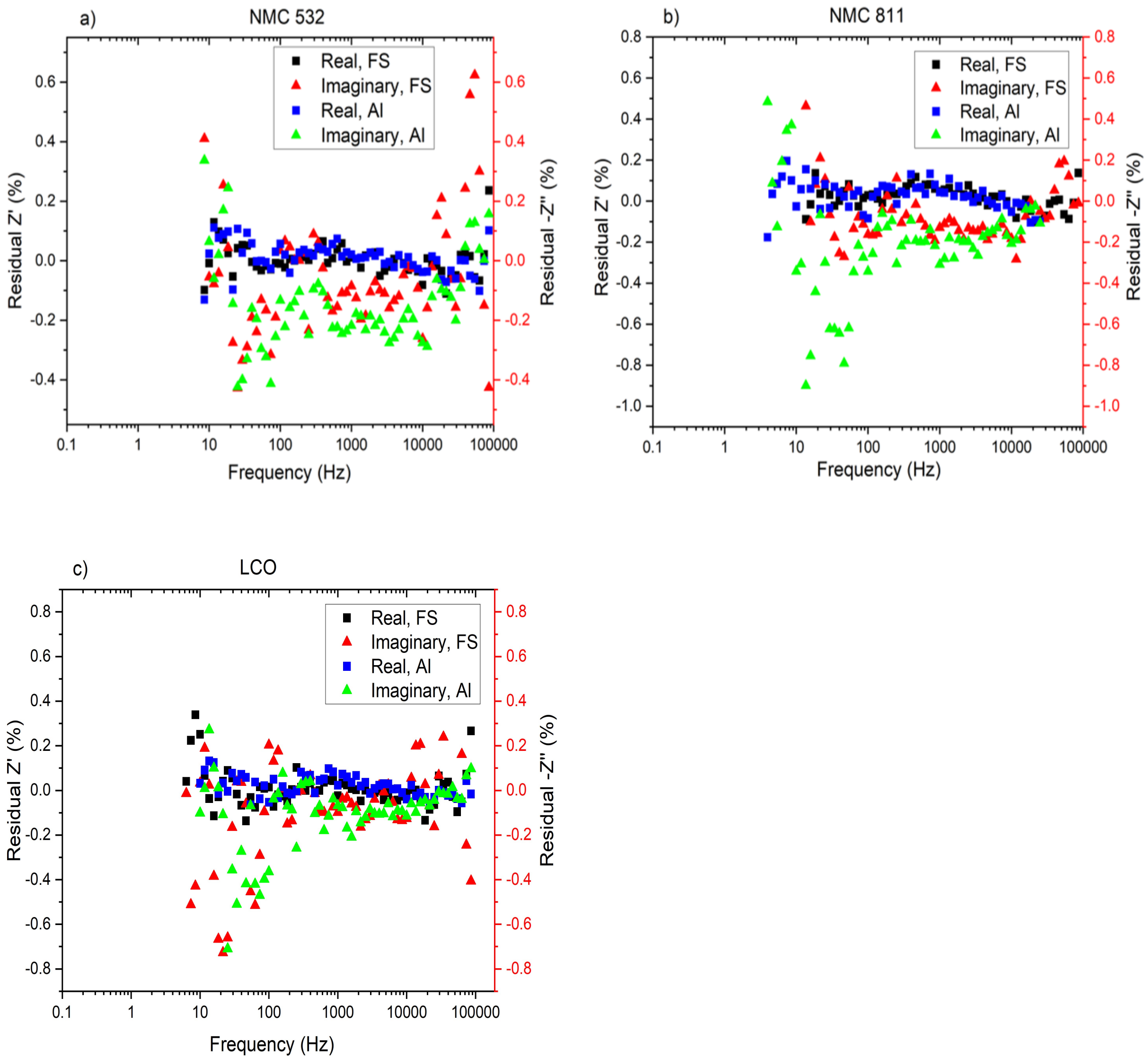

Figure A.2: KKT results of a) NMC 532, b) NMC 811 and c) LCO FS cathodes after 75 cycles.

A.3. SEM Results

A.3.1. After 1 cycle

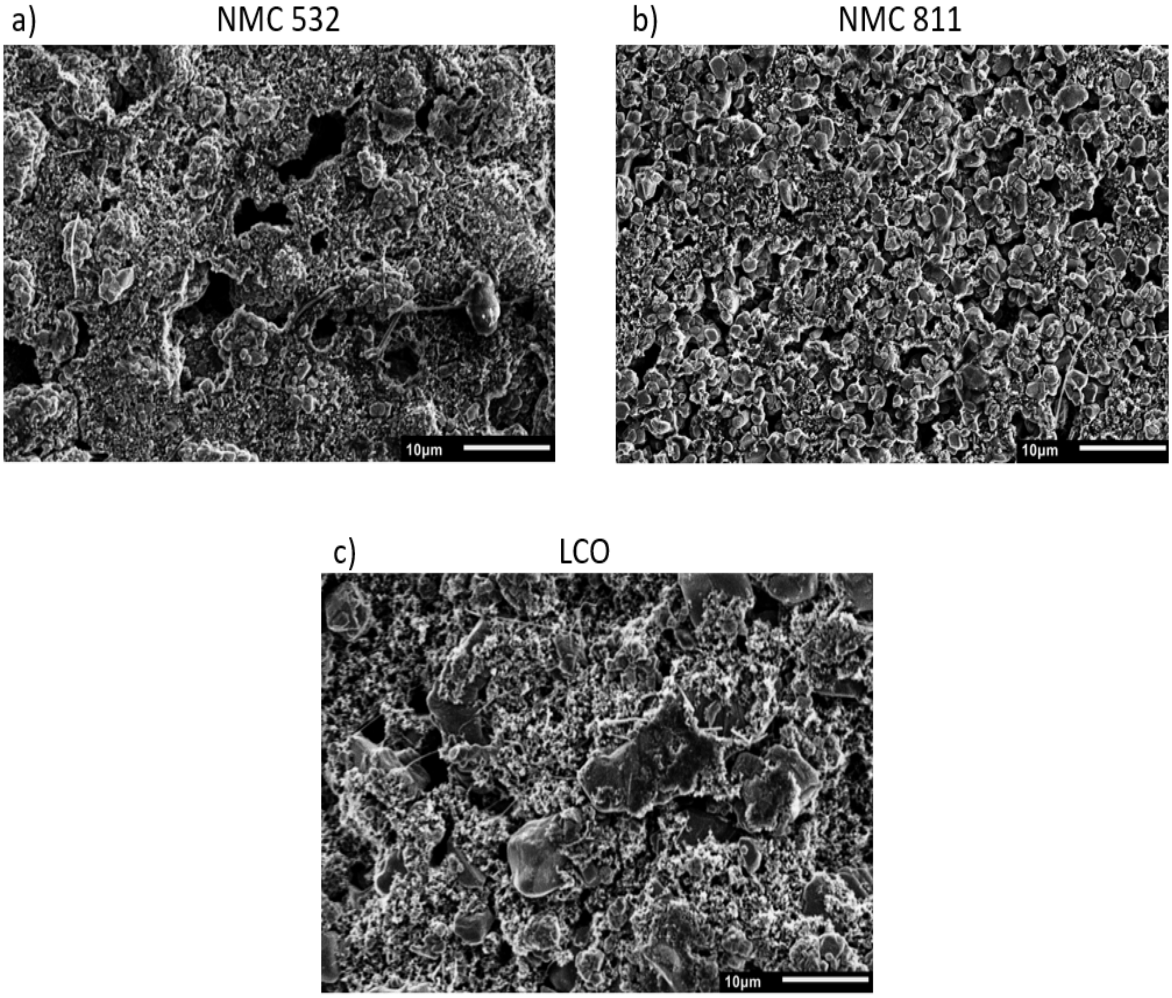

Figure A.3: SEM micrographs of uncoated a) NMC 532, b) NMC 811 and c) LCO FS cathodes after 1 cycle. The images are taken at 2000x magnification and 5 kV acceleration voltage.

A.3.2. After 75 cycles

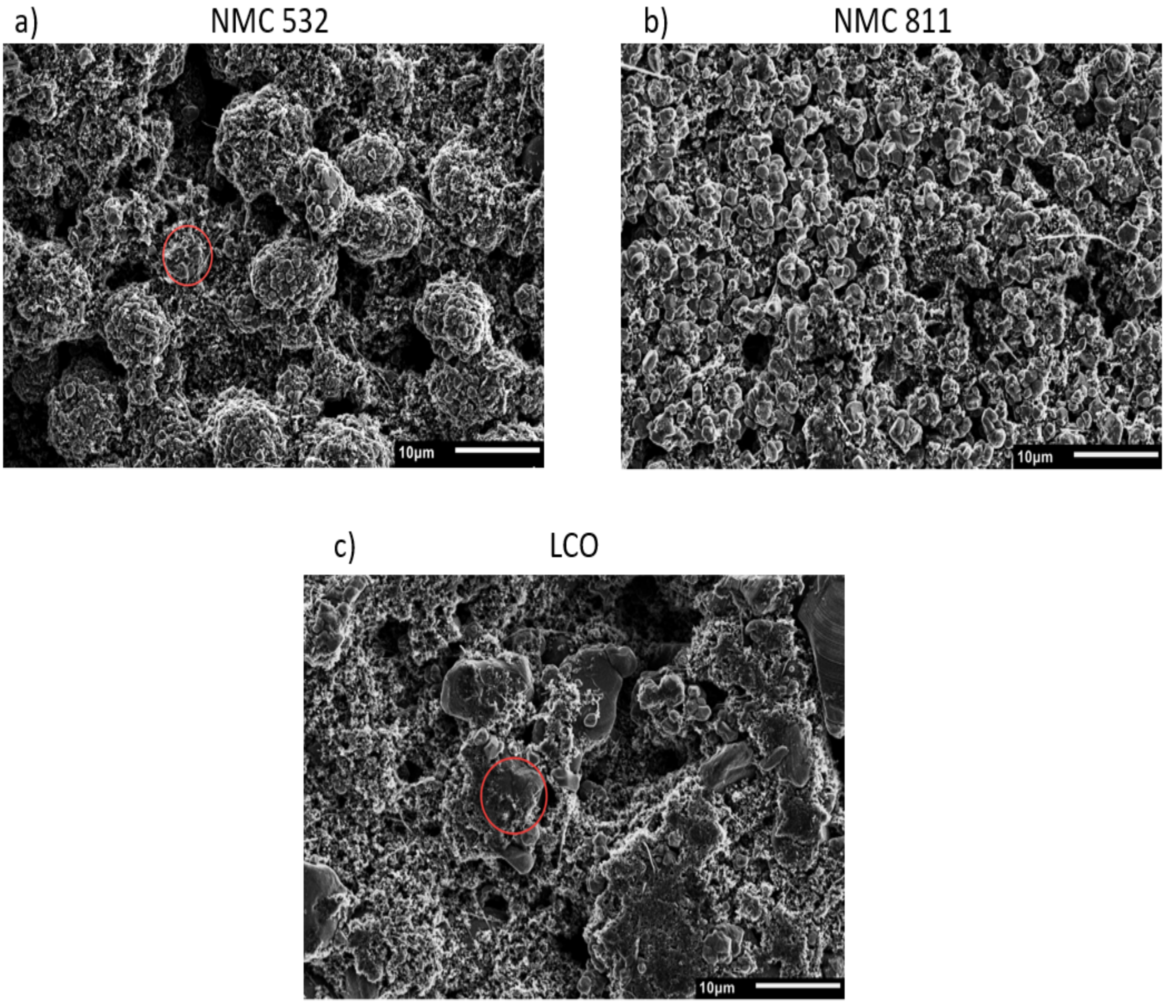

Figure A.4: SEM micrographs of uncoated a) NMC 532, b) NMC 811 and c) LCO Al cathodes after 75 cycles. The images are taken at 2000x magnification and 5 kV acceleration voltage. The highlighted region shows the presence of microcracks on the surface of the particles.

A.4. XRD Refinement Results

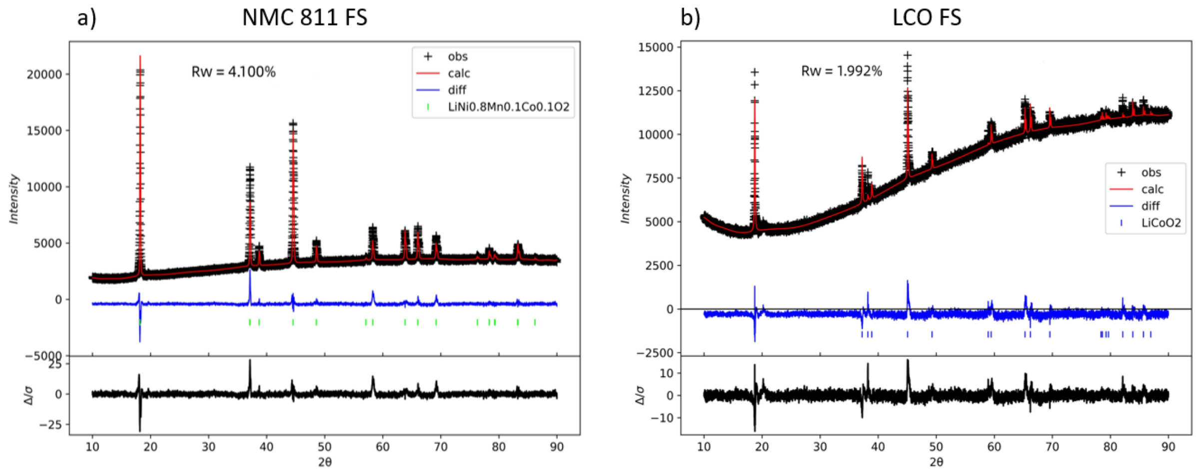

Figure A.5: Rietveld refinement patterns of uncoated NMC 811 and LCO FS cathodes after 75 cycles.

A.4.1. Lattice Parameters

Table A.1: Lattice parameters a, b, c and ratio c/a for uncoated NMC 532, NMC 811 and LCO FS cathodes, before cycling and after 75 cycles.

Cathode	**a**	**b**	**c**	**c/a**
NMC 532 FS uncycled	2.86839	2.86839	14.24063	4.9646
NMC 532 FS after 75 cycles	2.84805	2.84805	14.41015	5.0596
NMC 811 FS uncycled	2.87028	2.87028	14.18886	4.9433
NMC 811 FS after 75 cycles	2.82817	2.82817	14.55172	5.1453
LCO FS uncycled	2.81415	2.81415	14.055	4.9944
LCO FS after 75 cycles	2.80463	2.80463	14.14175	5.0422

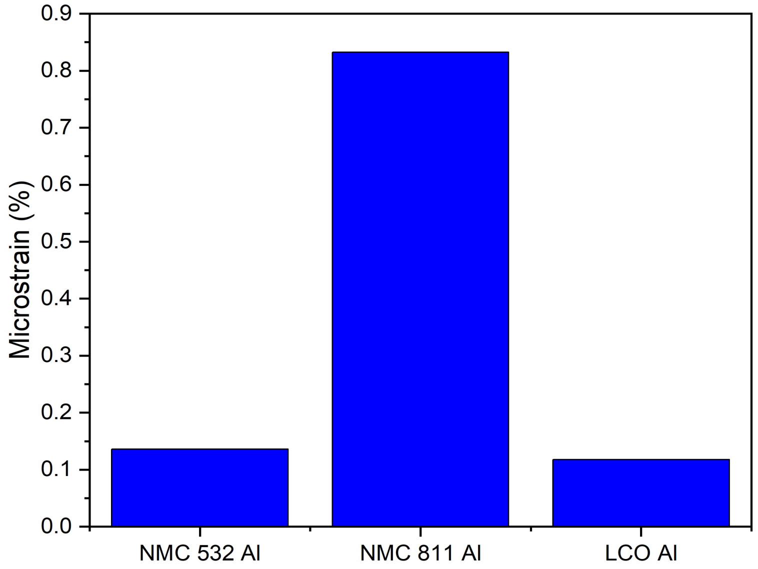

Figure A.6: Microstrain values obtained from Rietveld refinement of NMC 532, NMC 811 and LCO uncoated cathodes on aluminium current collector.

A.5. XPS Analysis of Transition Metal Elements in Powders and Cathodes

A.5.1. Powders

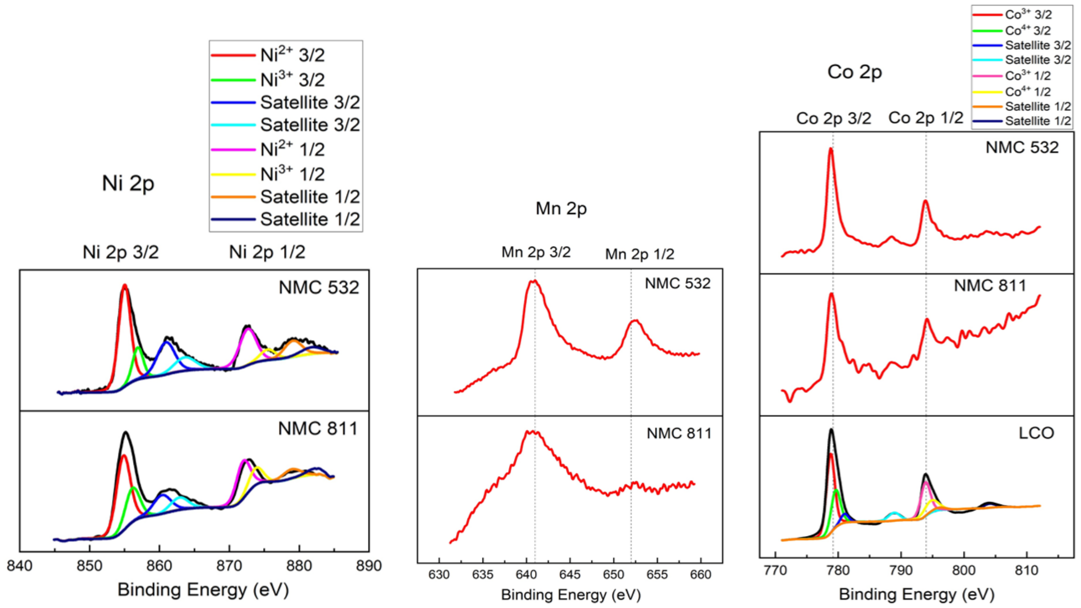

Figure A.7: (From left to right) Ni 2p, Mn 2p and Co 2p spectra of NMC 532 and NMC 811 cathode powders.

A.5.2. Cathodes

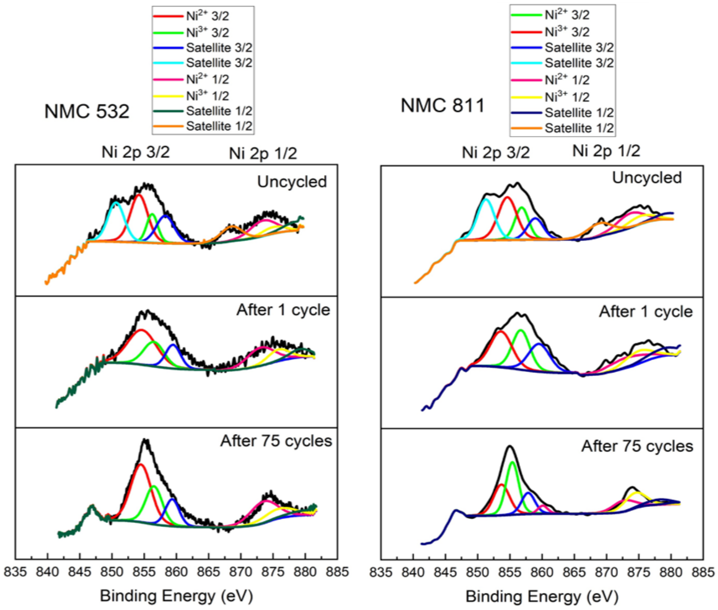

Figure A.8: Ni 2p spectra of (from left to right) NMC 532 and NMC 811 FS cathode samples. The cathode samples are tested before cycling, after 1 cycle and after 75 cycles.

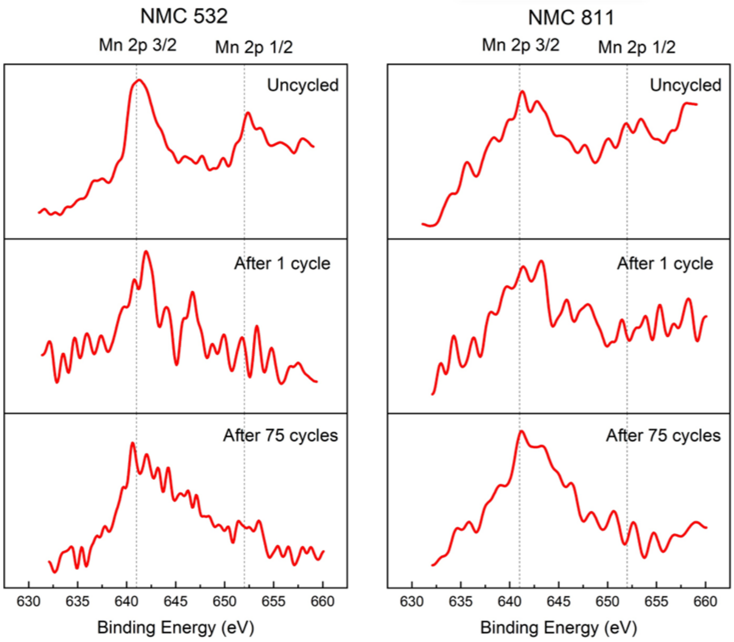

Figure A.9: Mn 2p spectra of (from left to right) NMC 532 and NMC 811 FS cathode samples. The cathode samples are tested before cycling, after 1 cycle and after 75 cycles.

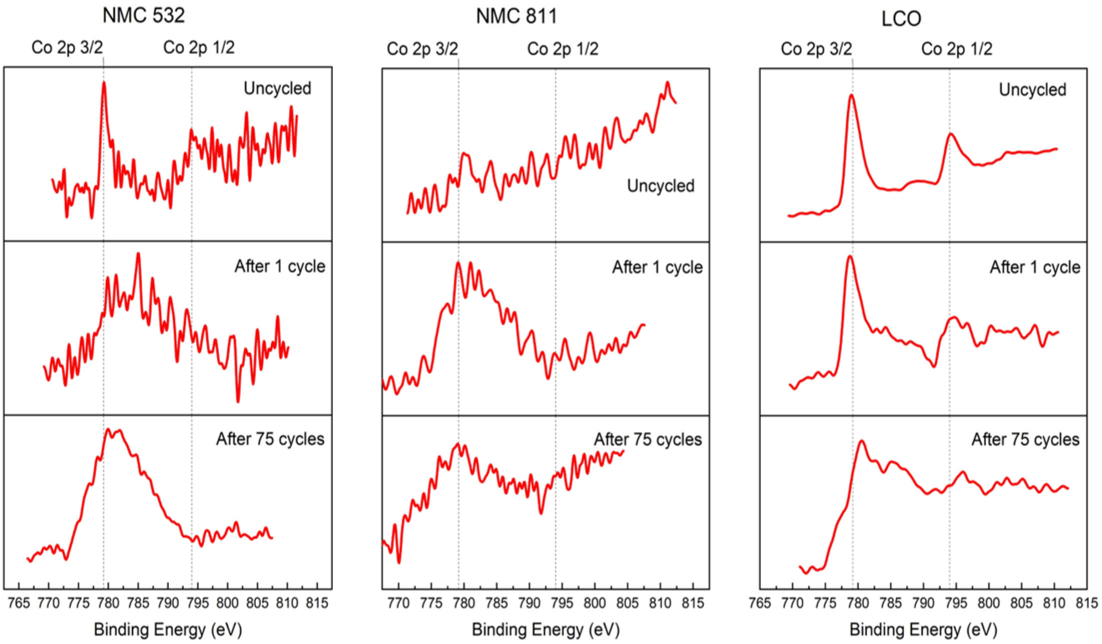

Figure A.10: Co 2p spectra of (from left to right) NMC 532, NMC 811 and LCO FS cathode samples. The cathode samples are tested before cycling, after 1 cycle and after 75 cycles.

B

Supplementary Information - ALD Coated Cathodes

B.1. Electrochemical Cycling Performance of a Full Cell and a Half Cell

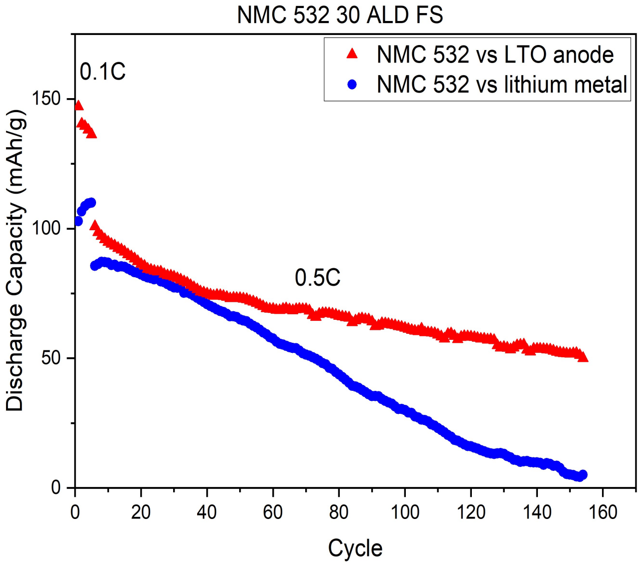

Figure B.1: Long term cycling test on NMC 532 30 FS cathode used in a full cell and a half cell. The test was performed for 150 cycles at 0.5 C rate, in addition to 5 formation cycles at 0.1 C rate. The anode used in a full cell and a half cell was lithium titanate (LTO) and lithium metal, respectively.

B.2. dQ/dV Analysis of ALD Coated Cathodes on Aluminium Current Collector

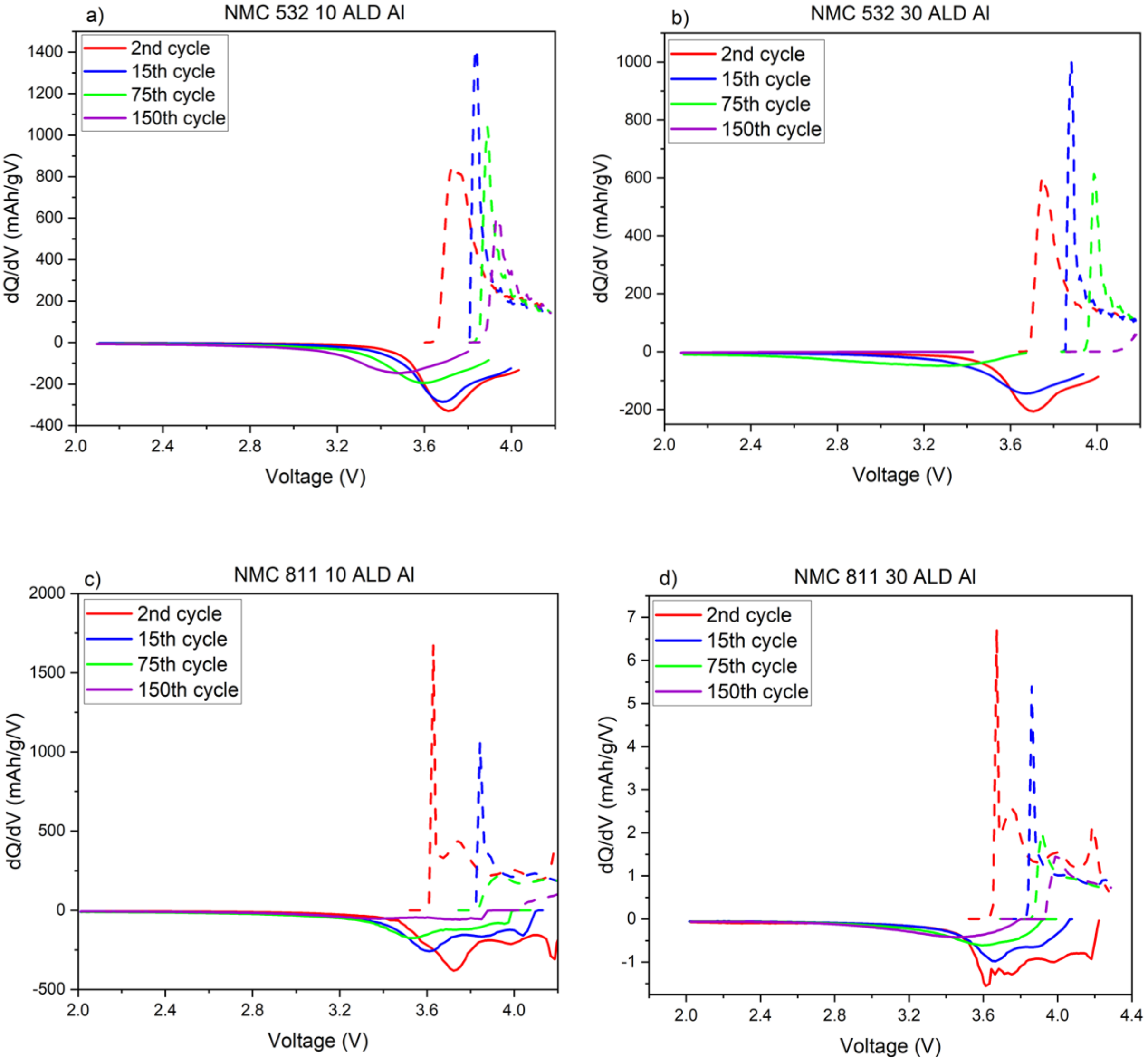

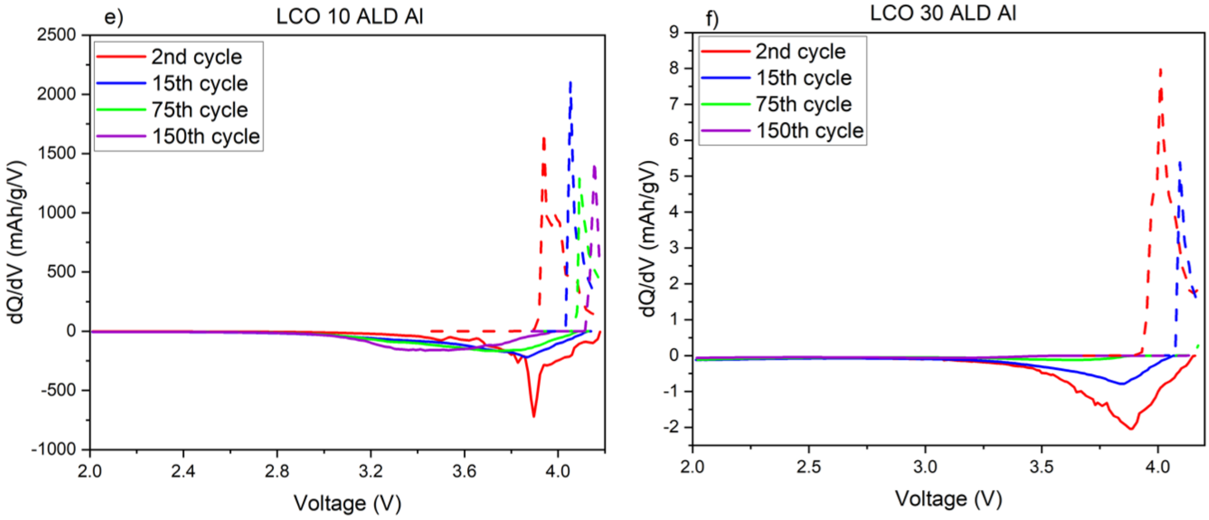

Figure B.2: dQ/dV curves of Al NMC 532, NMC 811 and LCO cathodes (10 ALD and 30 ALD) after 2nd, 15th, 75th and 150th cycle*. * 2nd cycle is at 0.1 C rate, while 15th, 75th and 150th cycles are at 1 C rates.

B.3. EIS Results for ALD Coated Cathodes on Aluminium Current Collector

B.3.1. EIS Spectra

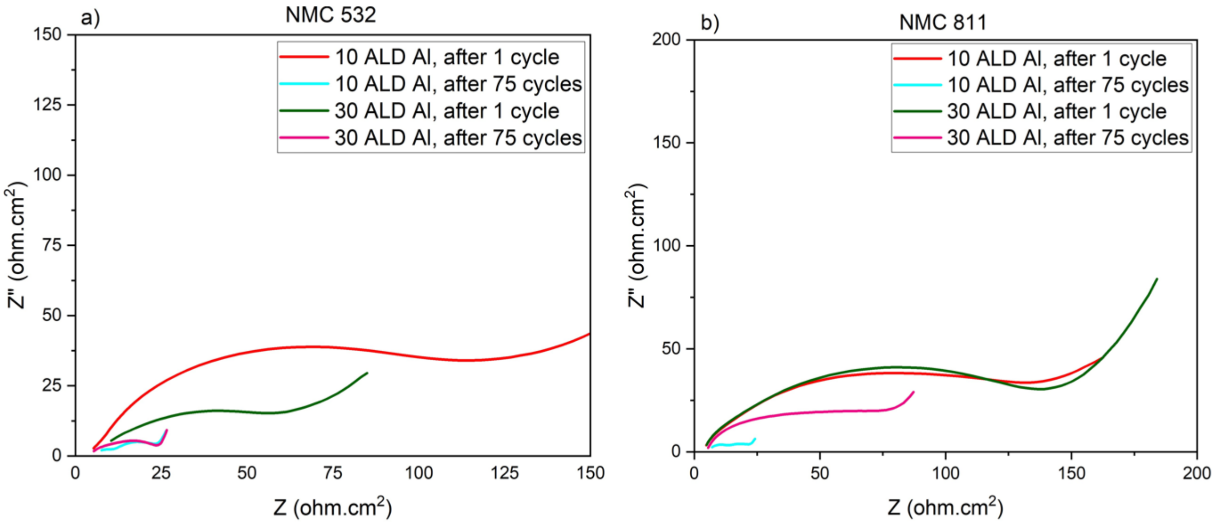

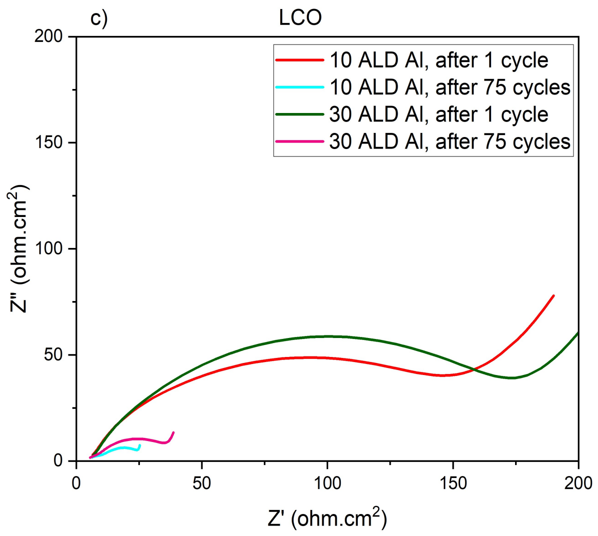

Figure B.3: EIS spectra of NMC 532, NMC 811 and LCO ALD coated cathodes on aluminium current collector, *after the 1st and the 75th cycle. The spectra follows the circuit model as shown in fig 5.7. * 1st cycle is at 0.1 C rate, while the 75th cycle is at 1 C rate.

B.3.2. KKT Results

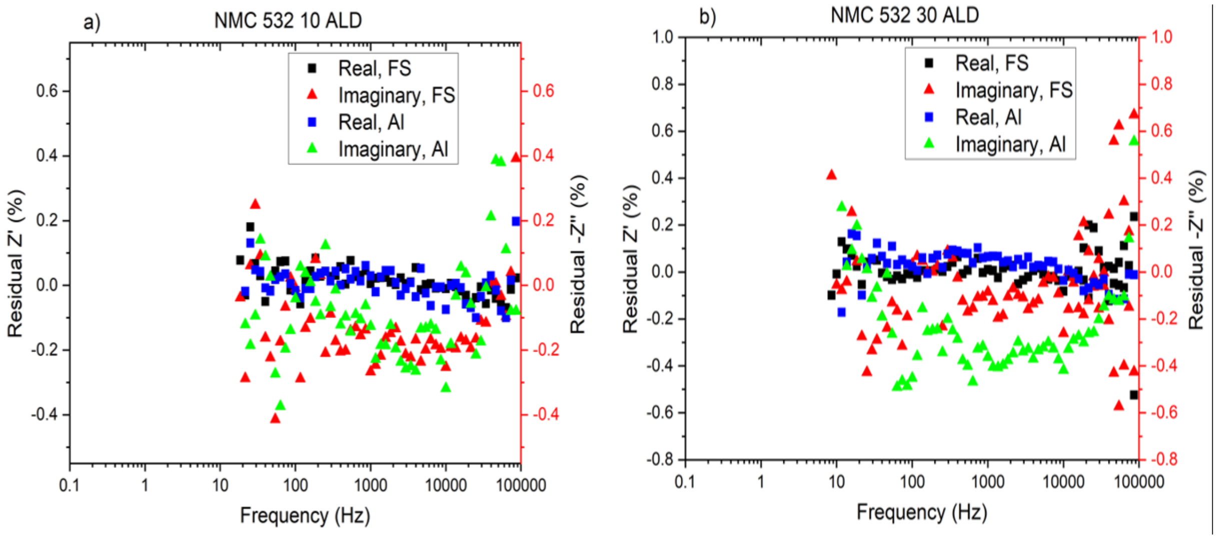

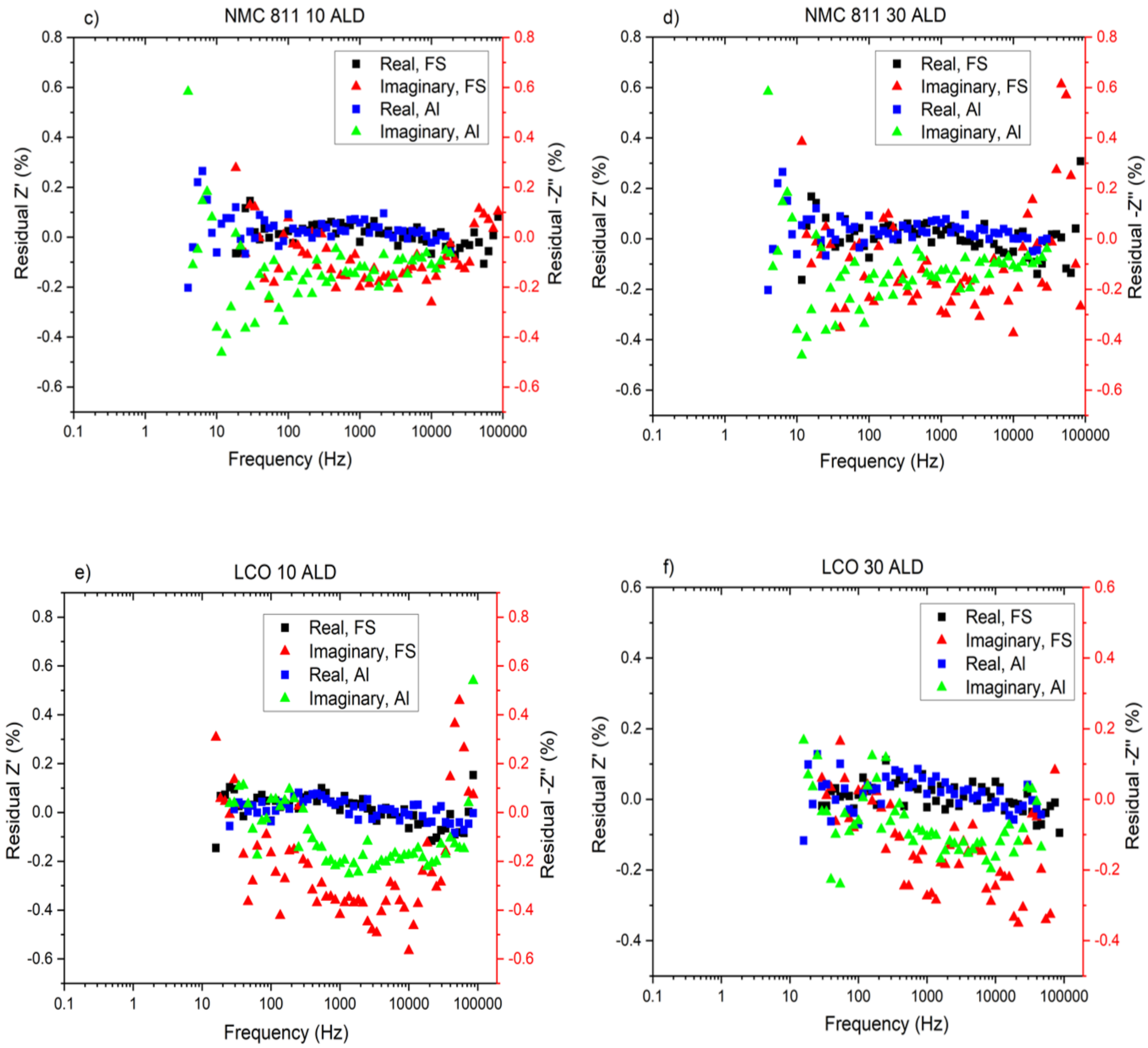

Figure B.4: KKT results of NMC 532, NMC 811 and LCO ALD coated cathodes after 75 cycles.

B.4. SEM Microstructure of ALD Coated Cathodes

B.4.1. After 1 cycle

a) NMC 532 10 ALD

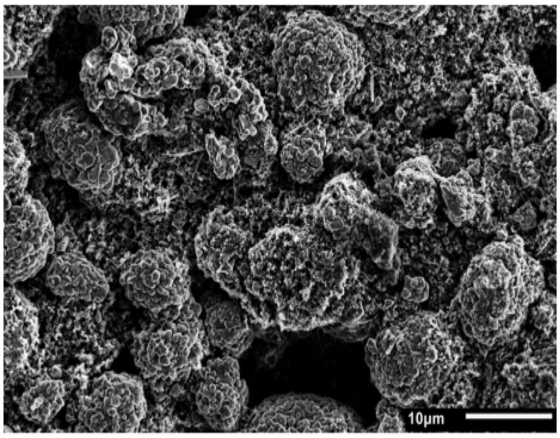

b) NMC 532 30 ALD

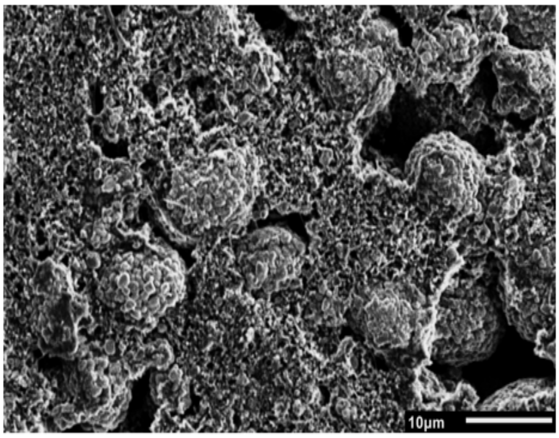

c) NMC 811 10 ALD

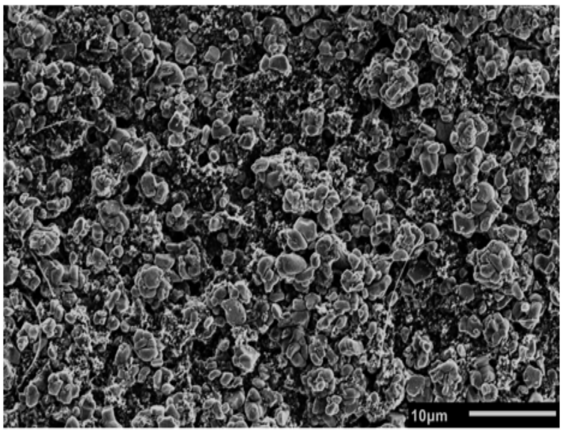

d) NMC 811 30 ALD

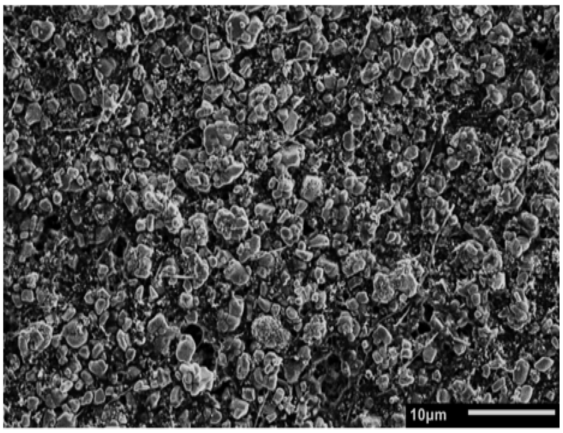

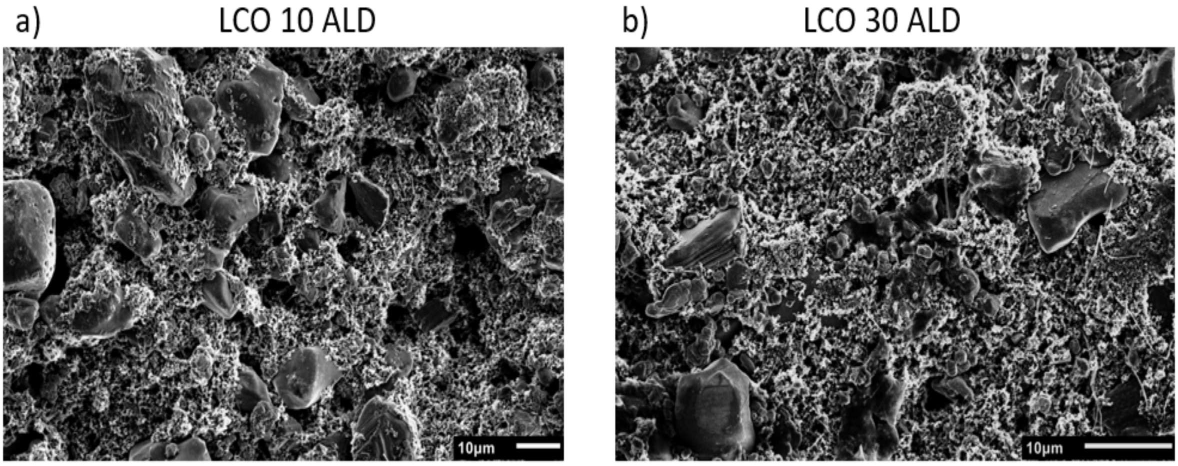

Figure B.5: SEM micrographs of ALD coated NMC 532, NMC 811 and LCO FS cathodes after 1 cycle. The images are taken at 2000x magnification and 5 kV acceleration voltage.

B.4.2. After 75 cycles

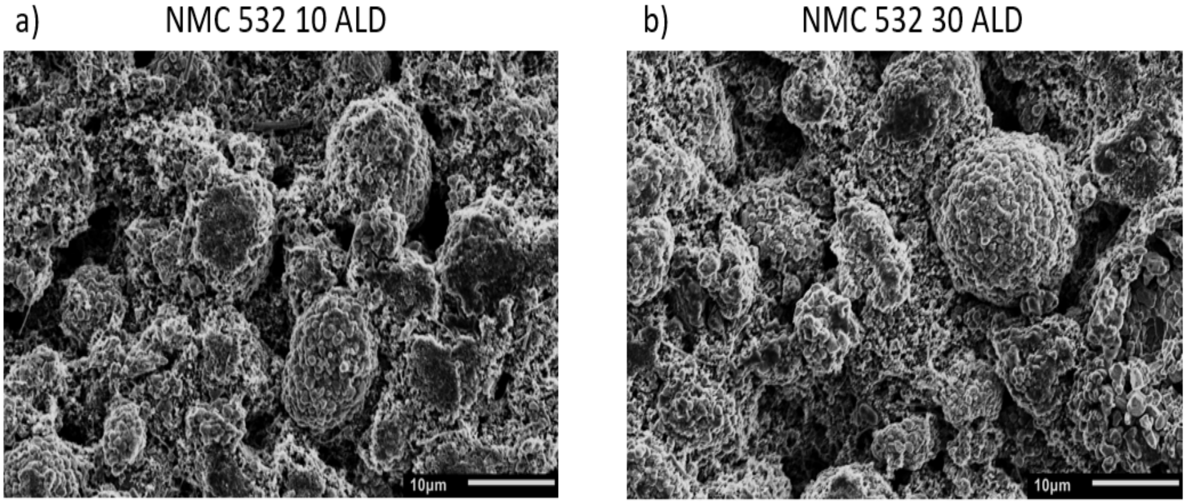

c) NMC 811 10 ALD

d) NMC 811 30 ALD

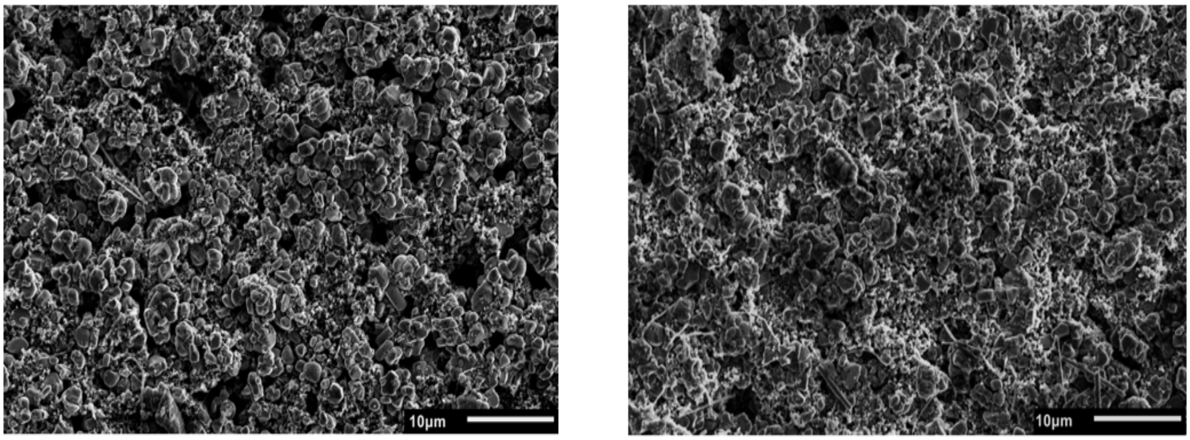

a) LCO 10 ALD

b) LCO 30 ALD

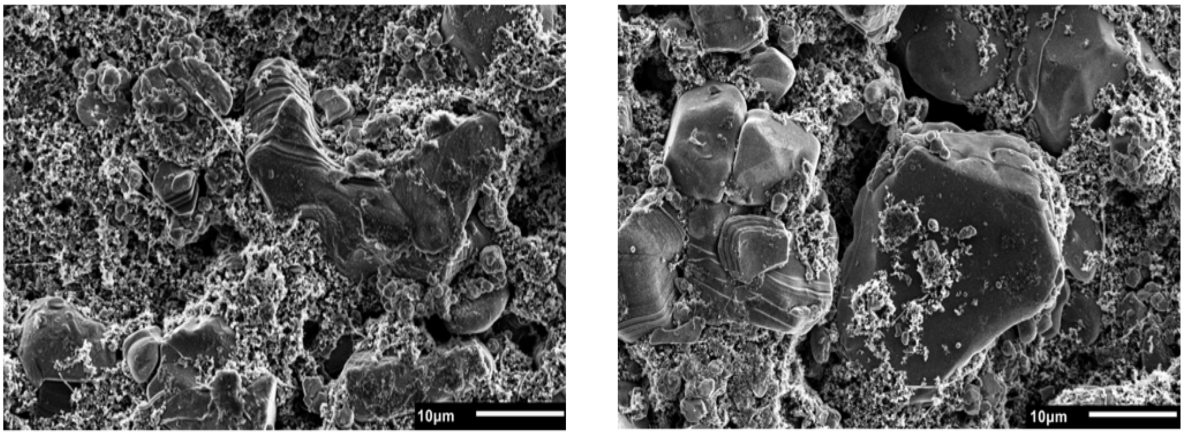

Figure B.6: SEM micrographs of ALD coated NMC 532, NMC 811 and LCO cathodes on aluminium current collector after 75 cycles. The images are taken at 2000x magnification and 5 kV acceleration voltage.

B.5. EDS Results

B.5.1. NMC 532

Table B.1: SEM-EDS results of NMC 532 uncoated, 10 ALD and 30 ALD cathodes after 75 cycles.

Elements		**NMC 532 uncoated FS**			**NMC 532 10 ALD FS**			**NMC 532 30 ALD FS**	
		Mass %	**Atom %**		**Mass %**	**Atom %**		**Mass %**	**Atom %**
C		26.73	45.19		29.19	47.09		27.07	45.44
O		27.1	34.39		28.15	34.1		27.58	34.81
F		5.71	6.1		6.3	6.42		5.07	5.38
Al		0	0		0.17	0.12		0.43	0.32
P		0.13	0.08		0.23	0.14		0.13	0.11
Mn		12.7	4.69		11.28	3.98		12.58	4.62
Co		7.79	2.68		7.04	2.32		7.69	2.63
Ni		19.85	6.86		17.66	5.83		19.45	6.68

B.5.2. NMC 811

Table B.2: SEM-EDS results of NMC 811 uncoated, 10 ALD and 30 ALD cathodes after 75 cycles.

Elements		**NMC 811 uncoated FS**			**NMC 811 10 ALD FS**			**NMC 811 30 ALD FS**	
		Mass %	**Atom %**		**Mass %**	**Atom %**		**Mass %**	**Atom %**
C		17.99	34.55		22.37	39.15		21.05	38.2
O		28.96	41.74		28.87	67.68		28.03	38.1
F		3.33	4.04		7.53	8.28		5.72	6.55
Al		0	0		0.29	0.23		0.59	0.48
P		0.23	0.17		0.24	0.15		0.12	0.14
Mn		2.8	1.18		2.34	0.89		2.51	0.99
Co		5.62	2.2		4.6	1.63		5.16	1.91
Ni		41.06	16.13		33.74	12		36.81	13.64

B.5.3. LCO

Table B.3: SEM-EDS results of LCO uncoated, 10 ALD and 30 ALD cathodes after 75 cycles.

Elements		**LCO uncoated FS**			**LCO 10 ALD FS**			**LCO 30 ALD FS**	
		Mass %	**Atom %**		**Mass %**	**Atom %**		**Mass %**	**Atom %**
C		30.14	47.81		31.76	47.72		33.59	50.67
O		30.23	36.01		30.69	35.74		28.65	32.44
F		4.8	4.81		6.26	6.14		7.88	7.51
Al		0	0		0.25	0.18		0.39	0.26
P		0.16	0.1		0.35	0.21		0.18	0.1
Co		34.67	11.27		32.68	10.01		29.32	9.01

The EDS data for NMC 532, NMC 811 and LCO show that with an increasing ALD coating thickness, the composition of aluminium increases. The presence of aluminium in the EDS spectrum after long term cycling, indicates that the Al_2O_3 layer remains present in the cathodes. Furthermore, in all the cathodes, a large quantity of C and O is present. A significant amount of this could arise from the carbon tape used during measurement. To verify this, an EDS measurement is performed with a plain carbon tape. The results are shown in table B.4 and its corresponding elemental maps are shown in fig B.7. The results clearly show a large quantity of carbon and oxygen present in the carbon tape, which may account for their higher prevalence in the cathode scans.

Table B.4: EDS measurement on carbon tape

Elements		**Carbon tape**	
		Mass %	**Atom %**
C		65.51	71.92
O		33.91	27.94
Al		0.05	0.03
Cu		0.53	0.11

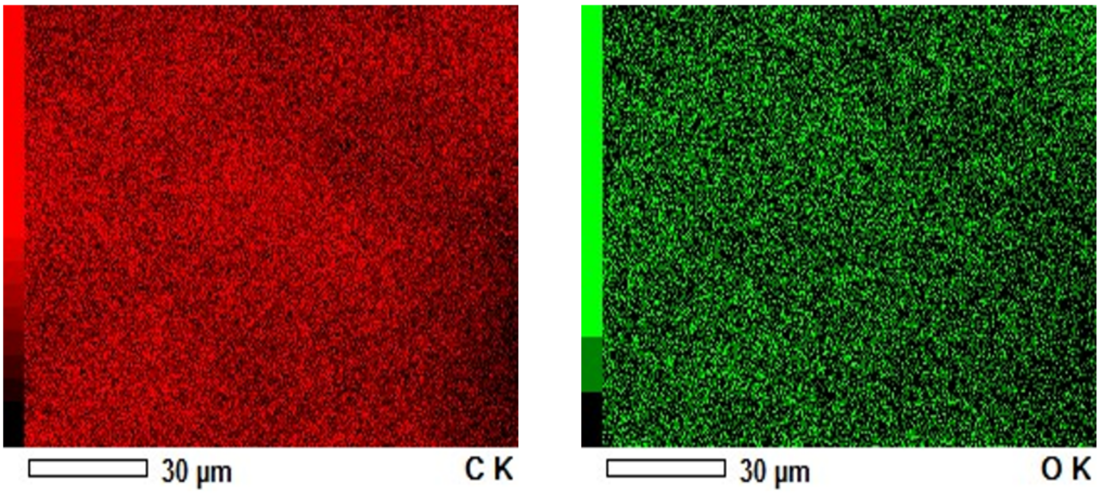

Figure B.7: Elemental maps for carbon and oxygen in the carbon tape, obtained from EDS.

B.6. XRD Results

B.6.1. Diffraction Patterns of NMC 811 and LCO Powder Samples

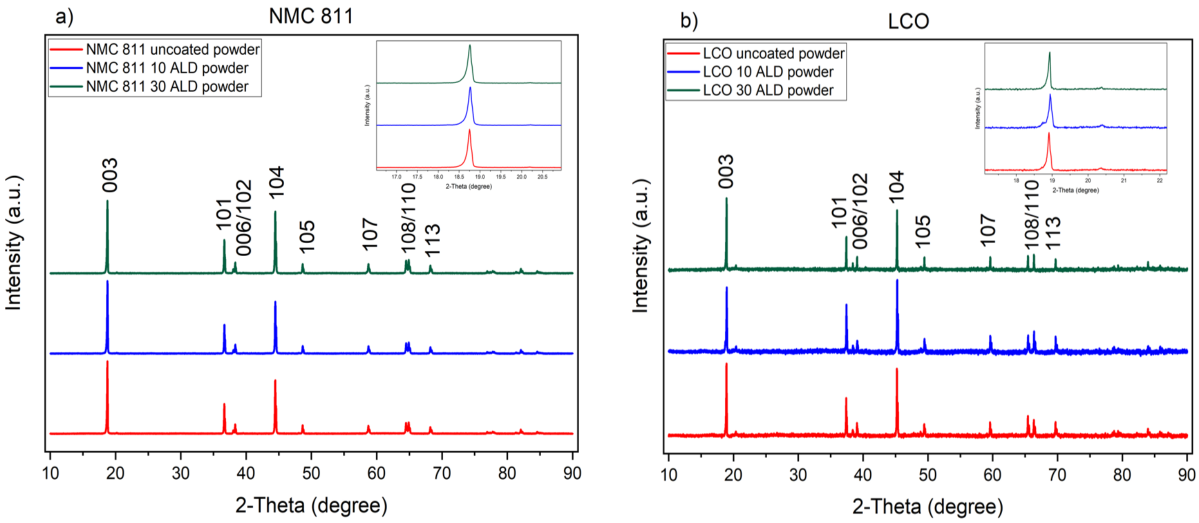

Figure B.8: Diffraction patterns of uncoated, 10 ALD coated and 30 ALD coated NMC 532, NMC 811 and LCO powder samples.

B.6.2. Rietveld Refinement on ALD Coated Cathodes

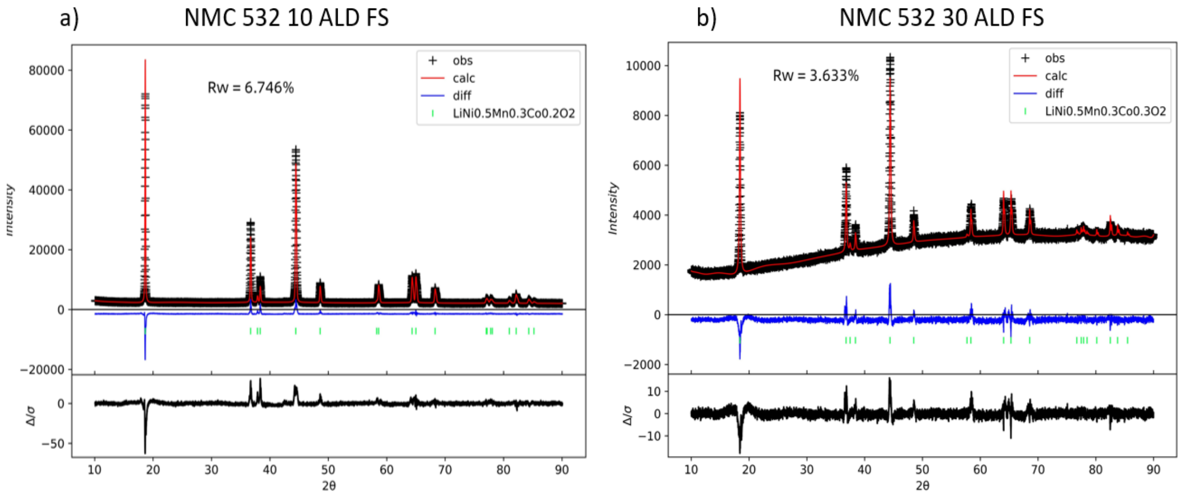

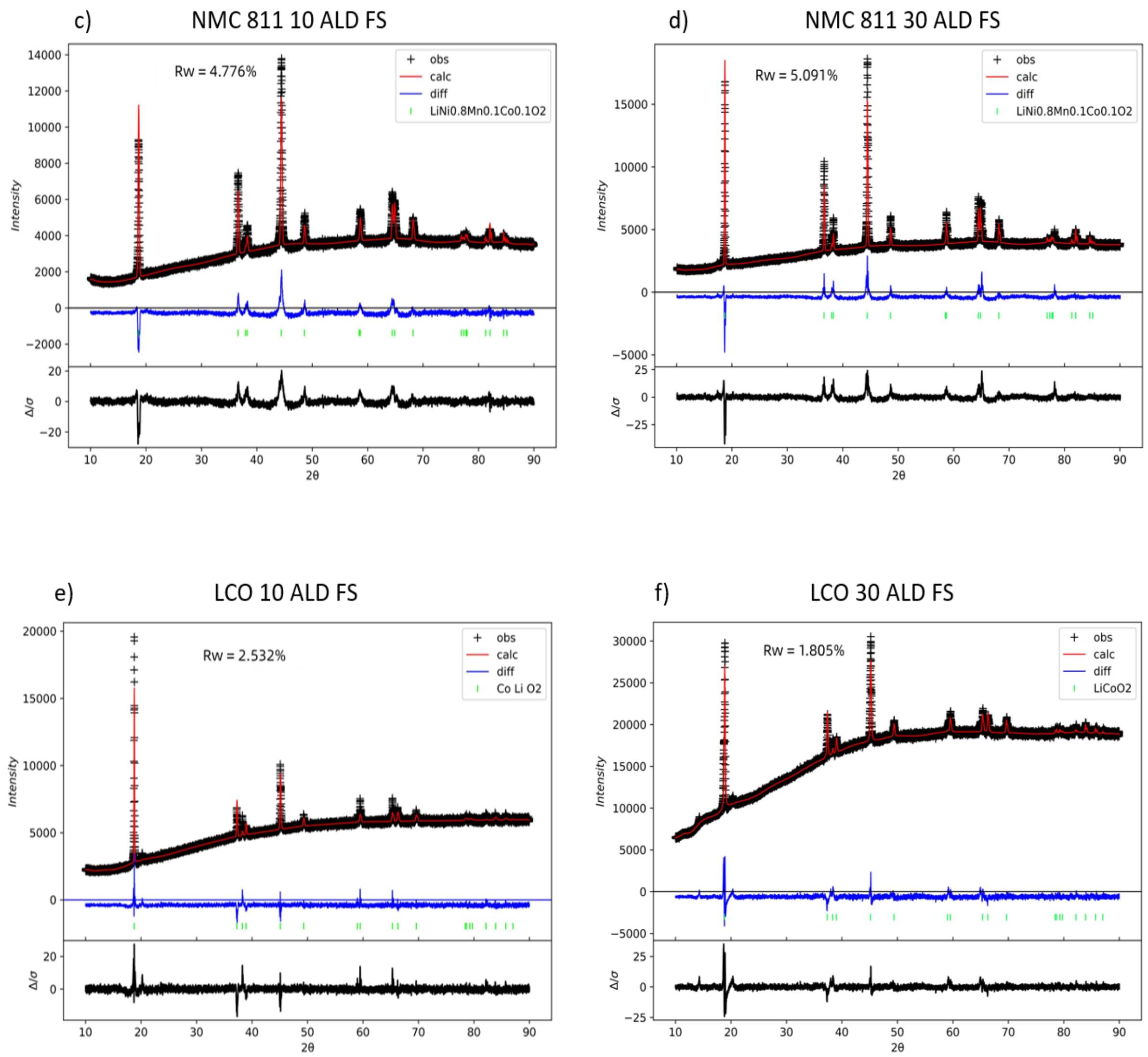

Figure B.9: Rietveld refinement patterns of ALD coated NMC 532, NMC 811 and LCO FS cathodes after 75 cycles.

B.6.3. Lattice Parameters

Table B.5: Lattice parameters a, b, c and c/a ratio of 10 ALD and 30 ALD NMC 532, NMC 811 and LCO FS cathodes, before cycling and after 75 cycles.

Cathode	**a**	**b**	**c**	**c/a**
NMC 532 10 ALD FS uncycled	2.86615	2.86615	14.2305	4.9650
NMC 532 10 ALD FS after 75 cycles	2.86615	2.86615	14.23047	4.9650
NMC 532 30 ALD FS uncycled	2.86608	2.86608	14.2299	4.9649
NMC 532 30 ALD FS after 75 cycles	2.85004	2.85004	14.33771	5.0307
NMC 811 10 ALD FS uncycled	2.86610	2.86610	14.16288	4.9415
NMC 811 10 ALD FS after 75 cycles	2.86755	2.86755	14.18383	4.9463
NMC 811 30 ALD FS uncycled	2.87012	2.87012	14.17437	4.9386
NMC 811 30 ALD FS after 75 cycles	2.87108	2.87108	14.18114	4.9393
LCO 10 ALD FS uncycled	2.82044	2.82044	14.10534	5.0011
LCO 10 ALD FS after 75 cycles	2.82127	2.82127	14.09829	4.9971
LCO 30 ALD FS uncycled	2.82333	2.82333	14.11551	4.9996
LCO 30 ALD FS after 75 cycles	2.81725	2.81725	14.06271	4.9916

B.7. XPS Analysis on Transition Metal Elements

B.7.1. Powders

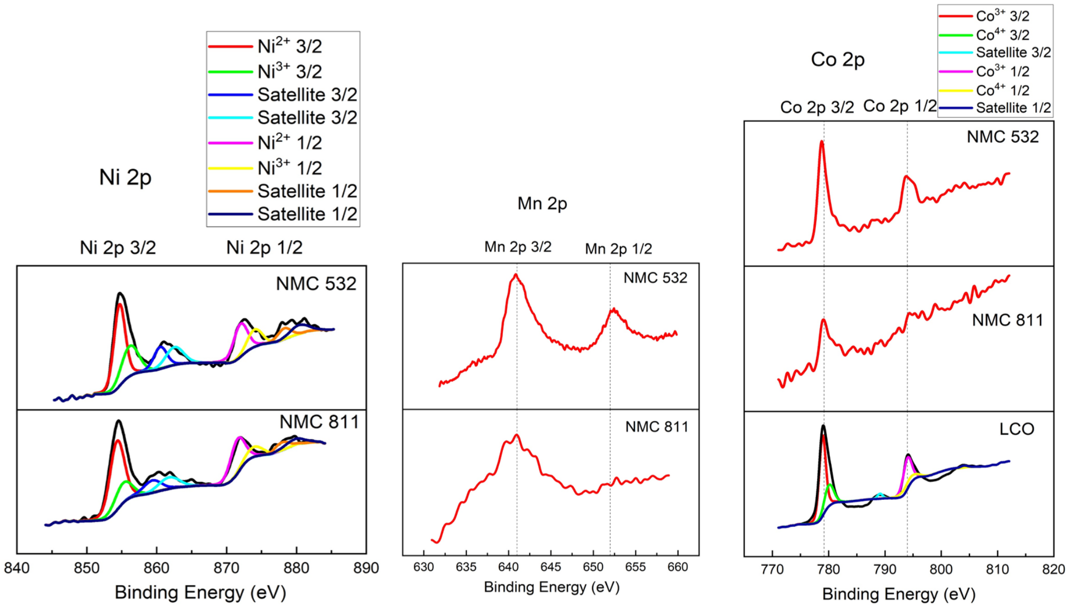

Figure B.10: (From left to right) Ni 2p, Mn 2p and Co 2p spectra of NMC 532 and NMC 811 10 ALD cathode powders.

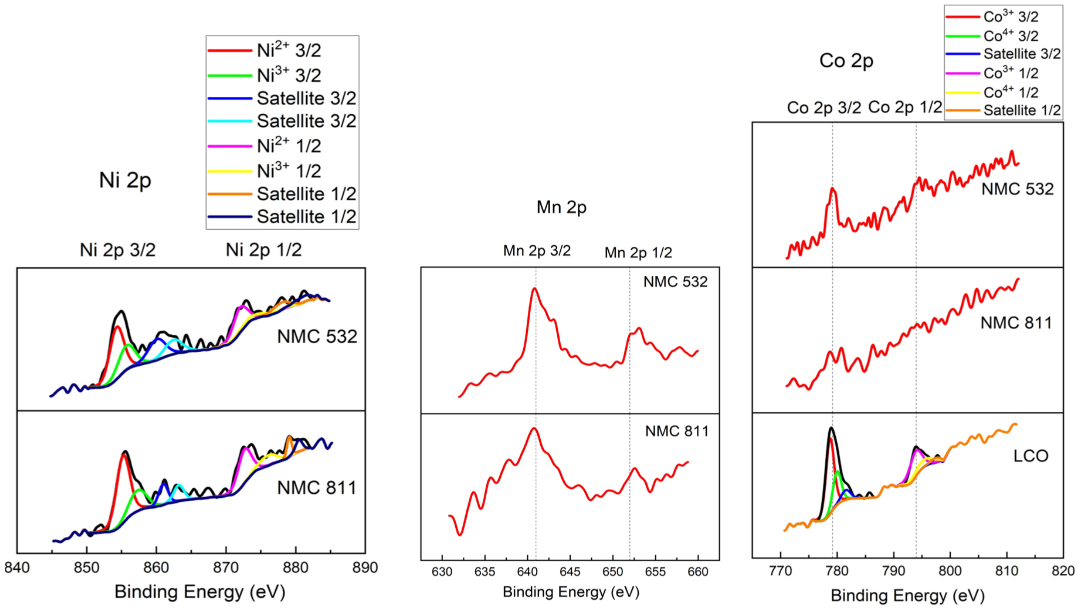

Figure B.11: (From left to right) Ni 2p, Mn 2p and Co 2p spectra of NMC 532 and NMC 811 30 ALD cathode powders.

B.7.2. Cathodes

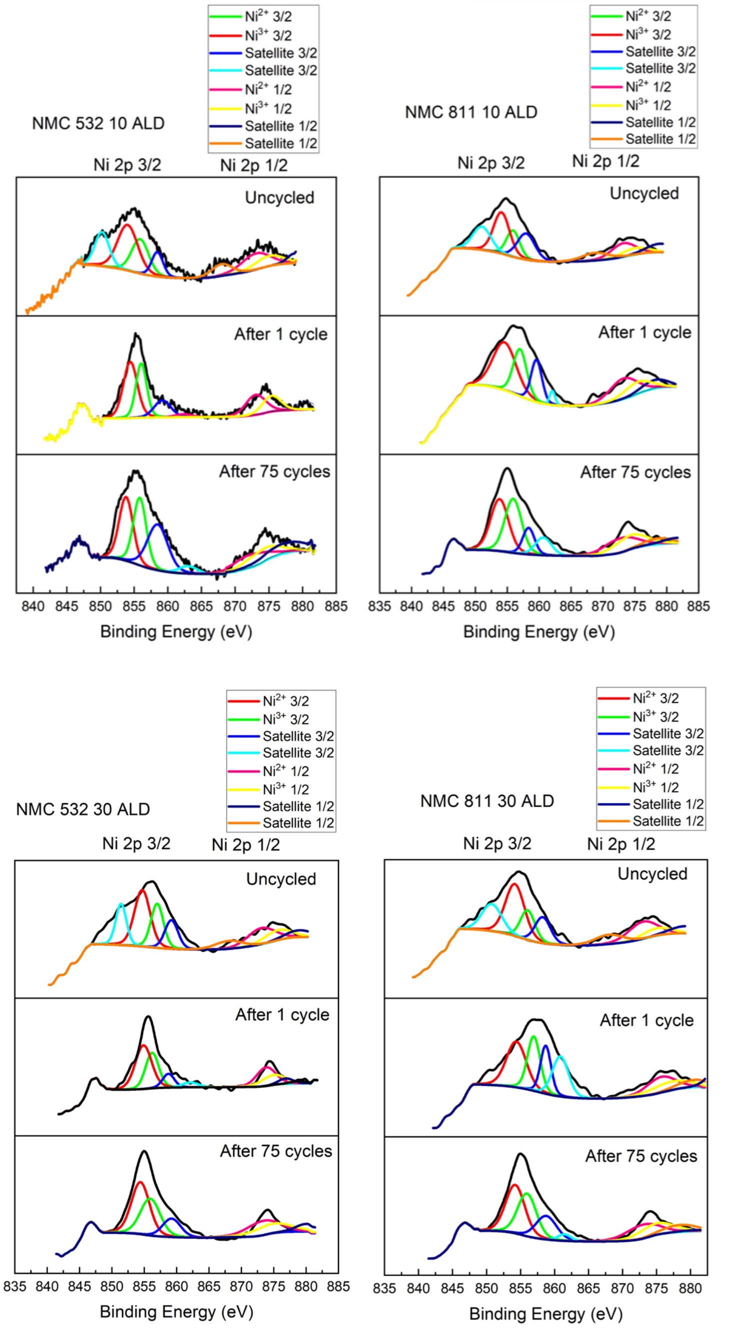

Figure B.12: Ni 2p spectra of (from top to bottom row) 10 ALD and 30 ALD, (from left to right) NMC 532 and NMC 811 FS cathode samples. The cathode samples are tested before cycling, after 1 cycle and after 75 cycles.

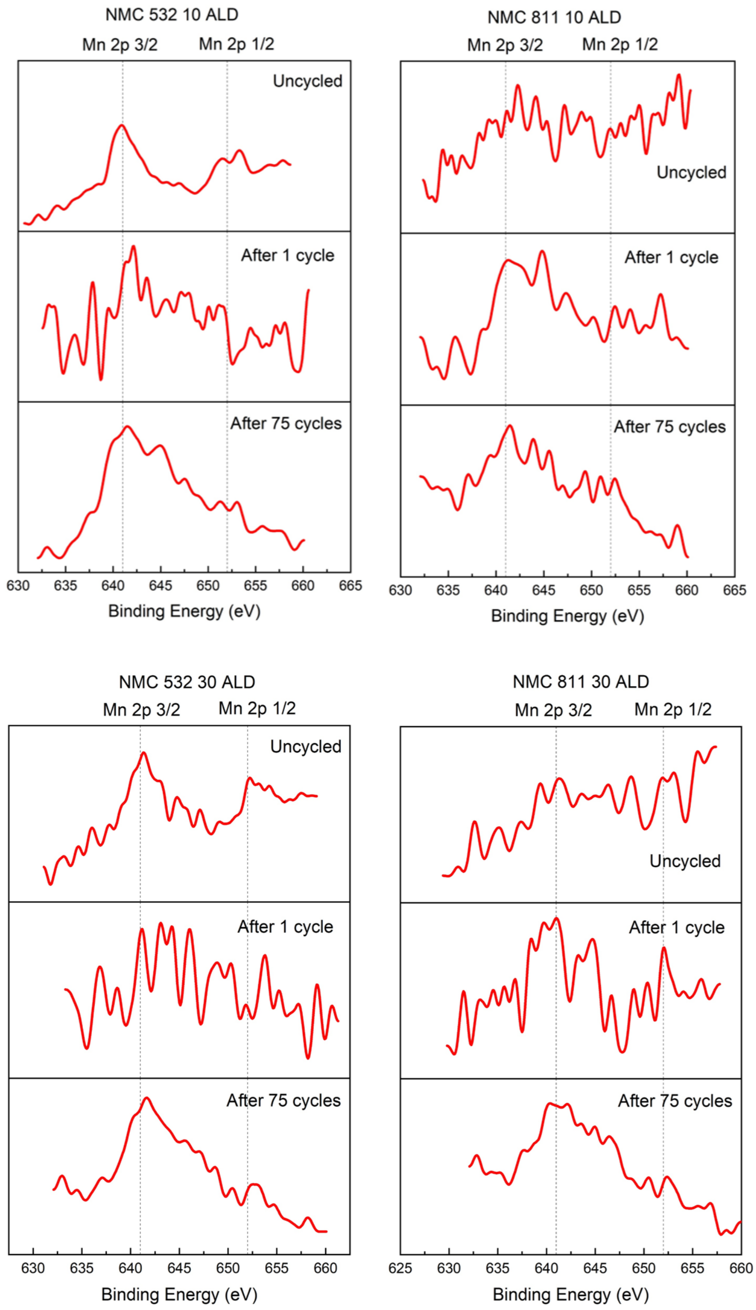

Figure B.13: Mn 2p spectra of (from top to bottom row) 10 ALD and 30 ALD, (from left to right) NMC 532 and NMC 811 FS cathode samples. The cathode samples are tested before cycling, after 1 cycle and after 75 cycles.

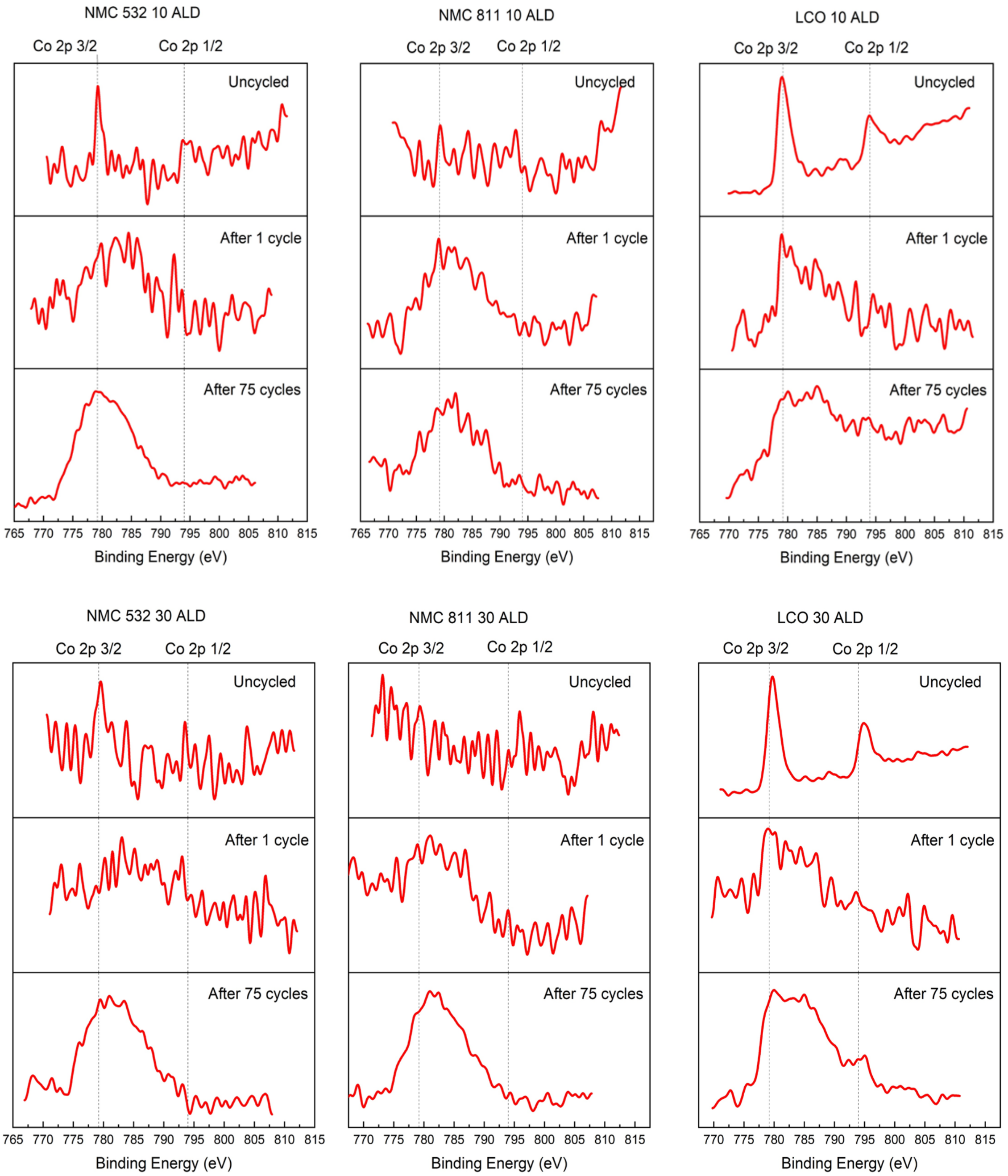

Figure B.14: Co 2p spectra of (from top to bottom row) 10 ALD and 30 ALD, (from left to right) NMC 532, NMC 811 and LCO FS cathode samples. The cathode samples are tested before cycling, after 1 cycle and after 75 cycles.

B.8. Effect of Storage Environment on NMR Spectra

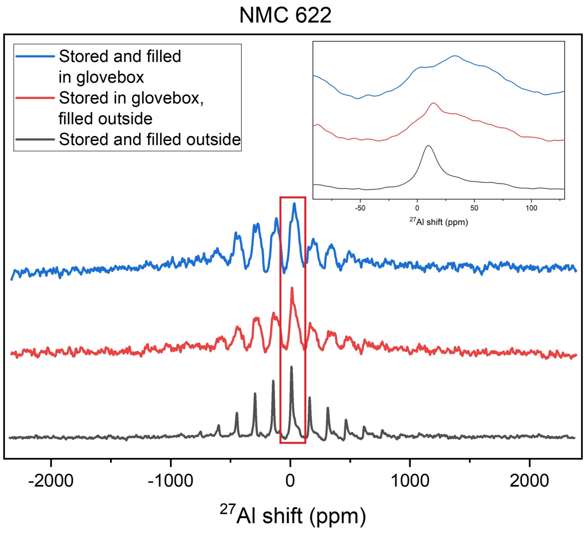

Figure B.15: ^{27}Al NMR spectra of NMC 622 under conditions of filling and storage, inside and outside the glovebox.